Biology's Wires and Motors: Single-Molecule Mechanics of M13 Bacteriophage and Kinesin

by

Ahmad Samir Khalil

B.S., Stanford University (2002)

S.M., Massachusetts Institute of Technology (2004)

Submitted to the Department of Mechanical Engineering
in partial fulfillment of the requirements for the degree of
Doctor of Philosophy in Mechanical Engineering
at the
MASSACHUSETTS INSTITUTE OF TECHNOLOGY
February 2009

Author .....
Department of Mechanical Engineering
October 16, 2008

Certified by .....
Angela M. Belcher
Germehausen Professor of Materials Science & Engineering, and Biological Engineering
Thesis Supervisor

Certified by .....
Matthew J. Lang
Associate Professor of Mechanical Engineering, and Biological Engineering
Thesis Supervisor

Accepted by .....
David E. Hardt
Ralph E. and Eloise F. Cross Professor of Mechanical Engineering
Chairman, Department Committee on Graduate Students

Biology's Wires and Motors:

Single-Molecule Mechanics of M13 Bacteriophage and Kinesin

by

Ahmad Samir Khalil

Submitted to the Department of Mechanical Engineering
on October 16, 2008, in partial fulfillment of the
requirements for the degree of
Doctor of Philosophy in Mechanical Engineering

Abstract

Nature serves as an inspiration for engineering design, and, conversely, engineering principles have helped to usher in a quantitative frontier of biology. This intricate interdependency between engineering and biology is strongly evident in the single-molecule regime, where high-resolution tools are addressing previously intractable biological problems, while nanotechnology is being accelerated by advances in molecular biology. This thesis explores both sides of the dichotomy in an effort to reveal the mechanics of two biological systems – M13 filamentous bacteriophage and kinesin motor protein – and the properties of their underlying parts.

M13 is a filamentous virus that has elicited the interest of the engineering community for its use in phage display of combinatorial peptide libraries and more recently as a 1D template for organizing and growing inorganic materials. Both applications rely on the direct link between genotype and phenotype, whereby each phage particle displays fusion molecules on its proteinaceous capsid and simultaneously carries the encoding DNA. A better understanding of its polymer mechanics is critical to the further development of future M13-based technologies. As a result, combined efforts in genetic engineering, optical trapping, and modeling were employed in the first characterization of the biopolymer's single-molecule elasticity, revealing a persistence length (1265 nm) that places it squarely in the semiflexible polymer regime. Single-molecule stretching also revealed a mechanically robust and genetically versatile tether that could serve as a general "molecular handle" for single-molecule biophysics. As such, M13 was further engineered to incorporate variants of the zinc finger, DNA-binding domain of transcription factor Zif268 as minor coat fusions. Single-molecule assays centered around the "zinc fingered-phages" are being developed to establish M13 as a standalone, single-molecule building block for achieving universal connectivity and for unlocking future studies on the nature of protein-DNA interactions.

Kinesin is an ATPase that "walks" processively along biofilament tracks to perform vital cellular processes. Whereas M13 mechanics were studied in the context of classical rod or polymer bending, our focus within kinesin mechanics is the molecular aspects of motility. While significant progress has been made in elucidating the broad features of the kinesin mechanochemical cycle, details of the force generation mechanism remain a mystery. Com-

bined efforts in molecular biology, optical trapping, and molecular simulation were employed to put forth a novel mechanism for the motor's power stroke, namely that it is produced when the conserved N-terminal *cover strand* forms a β-sheet with the neck linker to yield the *cover-neck bundle*. In agreement with simulation, single-molecule motility data revealed impairment of the force-generating capacity of cover strand mutants, as measured by a reduction in stall force from the wild-type. Motility data also suggest that targeting force-generating elements, such as the cover strand, is a plausible strategy for designing biological motors with tunable motile properties, bringing us one step closer to a complete blueprint of kinesin's parts and their collective functioning.

Thesis Supervisor: Angela M. Belcher
Title: Germehausen Professor of Materials Science & Engineering, and Biological Engineering

Thesis Supervisor: Matthew J. Lang
Title: Associate Professor of Mechanical Engineering, and Biological Engineering

Acknowledgments

My graduate school story is *A Tale of Two Labs*, and, as Charles Dickens opened his 1859 novel, I too can say that "it was the best of times, it was the worst of times." It was the worst of times because getting a PhD is *hard work*! It was the best of times because all that hard work goes into shaping the frontier of scientific discovery and, moreover, doing it alongside some of the most unique and intelligent people.

Two of the most remarkable people I encountered at MIT are my advisors, Angie Belcher and Matt Lang, to whom I am eternally grateful for welcoming me into their respective labs and for 4 years of mentorship and support. Angie is a gifted scientist whose contagious enthusiasm for research infects all those that surround her. Since the day I first approached her with the harebrained idea to optically trap bacteriophage, she has been the epitome of support, lending innovative and creative solutions when I needed them most. From her, I have learned that scientists can indeed attack the world's most challenging problems headfirst with creativity and dedication. Matt has both childlike curiosity when it comes to science and maturity beyond his years when it comes to advising, a combination of characteristics that makes working with him an absolute joy. Before joining his lab, I knew virtually nothing about optical trapping. Now, as I prepare to leave MIT, I am proud to say that I am a young leader in experimental single-molecule biophysics, all because he patiently taught me how to build instruments and how to make measurements. I also want to thank Matt for nurturing my goal of becoming a professor one day. To this end, he has challenged me to achieve excellence in research, to publish in the very best journals, and to give talks at conferences.

I also want to thank my thesis committee for their support and encouragement. My Draper Lab advisor, Jeff Borenstein, has vast knowledge in the field of bioengineering and, as a result, has provided me keen insight and guidance. Beyond my thesis project, it was a privilege to work with him on Draper Lab projects, in particular, in designing and constructing a novel, high-throughput system for studying endothelial cells in physiological conditions. Dean Subra Suresh's expertise in mechanics was critical in helping me to describe the behavior of both biological systems, M13 bacteriophage and kinesin, and it has been a true pleasure to learn from him.

Although it is cliché to say that you, as a scientist, must stand on the shoulders of giants, I am sincerely indebted to those who have come before me and those who will come after me. First, I would like to thank a few mentors, who I have had the privilege of interacting with during my tenure at MIT and who have served as academic examples for me: Roger Kamm, Lallit Anand, and Guillermo García-Cardeña. Next, I would like to thank my many collaborators. They include Chris Noren, who was integral in efforts to genetically engineer M13, and Wonmuk Hwang and Martin Karplus, who provided the theoretical basis for our entire kinesin study. Past members of the Belcher Lab deserving of recognition for setting the stage for my thesis project are Eric Krauland and Steve Kottmann. Similarly, in the Lang Lab, my thesis project would not have been possible without two, very talented individuals: Jorge Ferrer and Ricardo Brau, who built the Lang Lab's first optical trap from scratch. Other critical, contributing members to my thesis were Dave Appleyard and the next generation of graduate students, in particular, Joan Mao, Gaelen Hess, Anna Labno, and Yongdae Shin, who agreed to be my first (hopefully, of many) "students." Getting through

graduate school requires a strong culture of camaraderie and open discussion, similar to what we fostered in the "Belcher Lab Lunch Group." For this, I would like to thank Andrew Magyar, Robbie Barbero, Rana Ghosh, Georg Fantner, Vesal Dini, and the other past and future members of this group. Finally, I would like to acknowledge all the remaining members of the Belcher and Lang Labs who I was fortunate enough to interact with and meet.

I have been incredibly blessed with the most unique, passionate, and caring friends one could ask for, and it is impossible to express my full gratitude to each individual here in this short note. I want to thank all of you from the bottom of my heart for taking such an involved role in my graduate career and, more importantly, in my life. Thank you to the friends, new and old, here in Boston, which include Jeff Augustyn, Emilia Bevilacqua, Kathie Dionisio, Anna Engstrom, Israel Green-Hopkins, Tim Hare, Leonard Lee, Pete & Tina Mack, Robin Prince, Jess Scott, Luke Thompson, Adam Vollmer, and Eli Weinberg. A special thank you to my Stanford drawmates, Amer Ahmed, Steve Compton, Matt Garr, Navid Karimeddiny, Yum Vo, and Justin Volmert, who remain among my most trusted confidants and who dream of reuniting as "drawmates" one day on a cul-de-sac. For the time being, our reunions over the past 6 years, such as the "Autumn Spiced Drink Classic," have kept me balanced, grounded, and energized. Thank you so much, guys! Finally, I would like to thank two of my oldest friends, Ann Hsing and Evan Carlson. Your longstanding friendships have meant so much to me over the years, and I hope we are able to share these memorable events for a long time to come.

Immigrant families are, by nature, tight-knit groups. The Khalil's may actually take 'tight-knit' to a whole new level, but I think this is a good thing. Ayman, my brother, interprets this as having free reign over the contents of my closet. Joking aside, though, I consider myself blessed for having had the opportunity to live with my best friend and brother for the majority of my graduate school career. Thank you, Ayman, you have been a strong source of support and a constant reminder of home away from home. To my youngest brother, Karim, I am so proud of you and know that one day we will similarly be celebrating you. Seeing you during breaks and vacations has been a true source of joy for me. Thank you for being there whenever I have needed you, and thank you for being the calm, level-headed, and rational one in the family!

Another typical characteristic of immigrant families is a selflessness derived from the hope that your hard work will translate to a better life for your children. My parents have lived their entire lives by this creed, and, for that, I dedicate this work to them. Whether it was calling me every week to ask "how the viruses are" or keeping me company while I worked late into the night in high school, I want to thank you, Dad & Mom, for instilling in my a great work ethic, good values, and a love of learning.

When times are tough, the kinesin protein can always rely on the chemical fuel, ATP, to 'charge up' its motor. During my tough times in graduate school, I turned to my ATP: my wonderful girlfriend, Katie. Thank you, Katie, for sharing the graduate student experience with me, both literally and symbolically. Thank you for all the salad lunches, thank you for your Photoshop wizardry, thank you for making me paint the bedroom instead of writing my thesis, and, most of all, thank you for keeping me smiling.

ASK
Cambridge, MA
October, 2008

Contents

List of Figures

List of Tables

Chapter 1

Introduction

1.1 Background and Motivation

Philosophizing on the future of physics in a classic 1931 paper, Paul Dirac wrote,

> There are at present fundamental problems in theoretical physics awaiting solution, e.g. the relativistic formulation of quantum mechanics and the nature of atomic nuclei (*to be followed by more difficult ones such as the problem of life*), the solution of which problems will presumably require a more drastic revision of our fundamental concepts than any that have gone before [26].

In a precocious statement, Dirac not only portends the explosion of problems in the study of life and biology but also predicts that they will be problems shared by biologists, physicists, engineers, etc. The work herein is a modest attempt to take up Dirac's "call to arms" – it is focused, in the broadest sense, on engineering aspects of biology. On one hand, nature has served as endless inspiration for engineering design (Fig. 1-1, left panel), while, on the other hand, engineering and physics tools have pushed the study of biology to new, more quantitative frontiers (Fig. 1-1, right panel). These are of course enduring concepts, in fact, the icons of Fig. 1-1 were adapted from sketches by the artist/engineer/scientist Leonardo da Vinci. As early as 500 years ago, da Vinci drew inspiration for his many engineering ideas in life, often trying to mimic Mother Nature's solutions. Furthermore, he recognized

the power of artificial, mechanical systems for making difficult tasks simpler and for making scientific measurements more tangible.

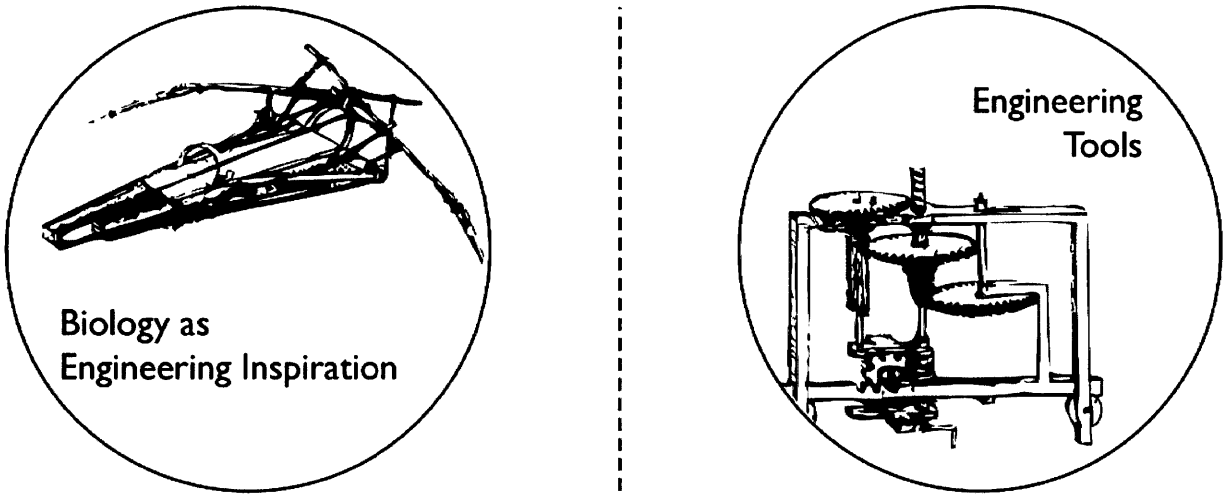

Figure 1-1: Engineering and biology. The circular dependency between engineering and biology was appreciated by Leonardo da Vinci. His designs for a "flying machine" were inspired by birds (left panel). Furthermore, he was fascinated by gears, levers, and other forms of mechanical advantage, featuring them in nearly all of his inventions (right panel).

We continue to propagate these concepts today. In the former case, biologically-inspired design and engineering has taken various forms. One approach is to understand and then artificially imitate biological and natural solutions. A well-known example of this 'biomimimetic' methodology is the design of synthetic structural composites based on rigid, biological materials. Since the discovery of their unusual combination of mechanical properties, including strength, stiffness, and toughness, the shells of mollusks have become guides for new materials technology [24]. Of the various structures present within the mollusk shell, it is the nacreous structure that has received increasing attention for its unique toughness – the amount of energy that can be absorbed and dissipated before failure [70]. The nacre structure is a hybrid composite, consisting of a small fraction of organic matrix ($1 - 5\%$ by volume) surrounding a ceramic, $CaCO_3$ inorganic phase, arranged in a "brick-and-mortar" architecture. As a results of its precise and highly developed structure, it can facilitate a variety of mechanisms that contribute to its ability to dissipate energy, which include the creation of new surface area and 'pull-out' of the ceramic phase from the organic component. Not surprisingly, researchers have developed various assembly and fabrication techniques in efforts to emulate

these structures and, more specifically, their energy dissipation mechanisms [15].

Another approach to biologically-inspired design is to engineer, or reverse engineer, a biological system in order to isolate or harness a desired functionality. The inherent, self-assembling nature of biomolecules, for instance, is one particularly desirable characteristic that has been exploited to construct novel, controllable structures from the "bottom up" [100]. Examples of intricate structures, bio-templated from deoxyribonucleic acid (DNA) [120], self-assembling peptides [127], and viruses [66, 67, 77, 126] have all been demonstrated. Viruses, specifically, make quite sophisticated biological materials, and a discussion below is dedicated to M13 filamentous bacteriophage as an engineered scaffold for inorganic materials. Biological systems possess even more complex functionality on the cellular level. In response to environmental and genetic stimuli, for instance, cells usher a battery of proteins, enzymes, and signaling molecules to sense forces, generate motion, remodel, and communicate. These phenomena are elegantly manifested in the vascular endothelium, where endothelial cells convert mechanical stimuli from hemodynamic forces into biochemical signals that fate their phenotypes through a collective mechanism known as mechanotransduction. Indeed, a mounting body of evidence suggests that endothelial cells function as sensors, with the ability to *discriminate* between shear stress patterns at arterial walls, and that certain shear stress patterns commonly found in bifurcated regions are able to trigger an atherosclerosis-susceptible phenotype [25].

In the latter case, experimental tools and quantitative models are being developed with specific aim at understanding the structure and function of biological systems. One important class of state-of-the-art tools for biological study is the ultra high-resolution instruments for measuring, probing, and manipulating single molecules. These include the single-molecule fluorescence microscope, atomic force microscope, magenetic tweezers, and optical tweezers and are discussed in more detail below. These, along with the plethora of tools for genomics, proteomics, and glycomics, have been integral in delivering vast amounts of biological data that are increasingly quantitative in nature and thus ripe for quantitative modeling. Ultimately, from these efforts, we hope to get closer to a general *and* predictive theory for the assembly and operation of biological systems [89].

Historically, the two sides of the biology/engineering interdependency (Fig. 1-1) have been demarcated and studied independently of one another. However, in this body of work, we do not demarcate the two concepts and show that applying both sides of the interface can be a powerful methodology in the study of single biomolecules.

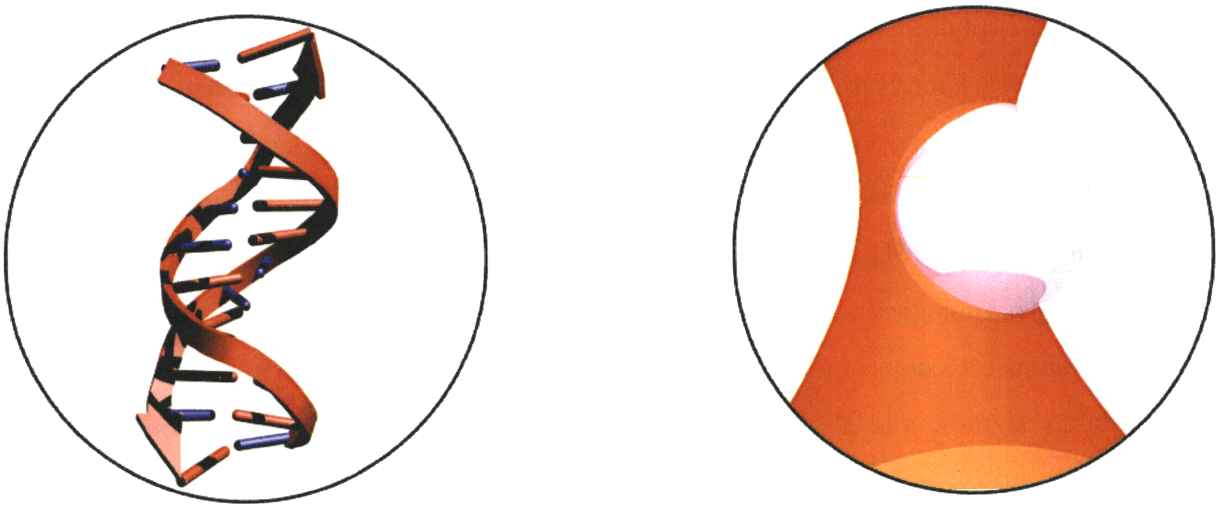

Figure 1-2: Engineering and biology: the single-molecule level. At the level of single molecules, molecular and structural biology techniques afford the opportunity to modify the structure and function of proteins (left panel). These single biomolecules can then be detected and manipulated with high-resolution instruments, such as optical tweezers (right panel).

The dichotomous relationship that exists between engineering and biology spans many length scales, but it is the single-molecule regime that is the focus of this thesis. In this regime, we are indebted to advances in molecular and structural biology for providing toolkits to modify and design biomolecules virtually at will (Fig. 1-2, left panel). On the other hand, physics and engineering have contributed ultra high-resolution instruments, such as the optical trap, for detection and manipulation as well as models that delicately blend statistical and continuum mechanics for describing dynamics (Fig. 1-2, right panel). In addition to possessing the biology knowhow and engineering tools, this regime is special for other reasons. At the length scale of single biological macromolecules, it can be shown that all fundamental energies converge (i.e., those associated with thermal, chemical, mechanical, and electrostatic phenomena) (Fig. 1-3) [89]. This is an interesting result with deep consequence – it helps to explain the diverse and rich dynamics of biological macro-

molecules and the exceptional efficiency of processes carried out by molecular machines. For instance, enzymes, such as ATP synthase, work under constant thermal bombardment and harness these thermal effects to bring about conformational, bonding, electrostatic changes that collectively produce deterministic behavior and power processes.

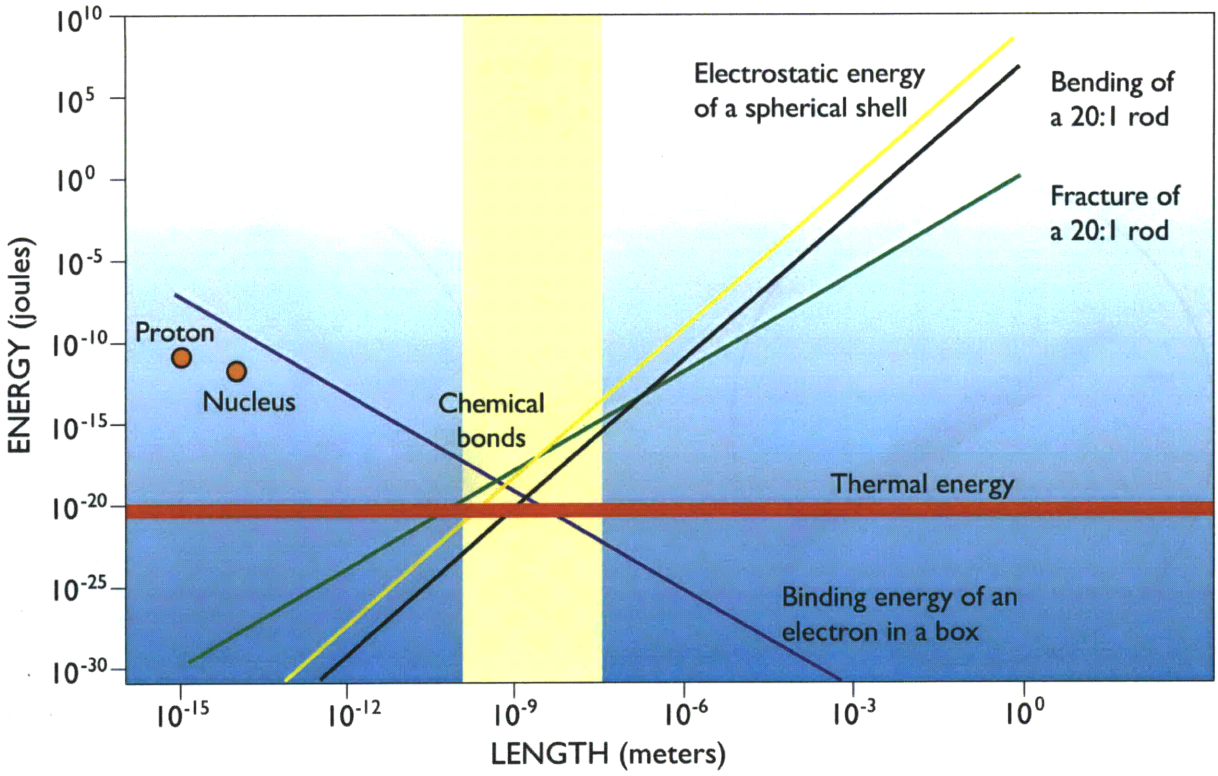

Figure 1-3: The convergence of energy scales. At the length scale of single biological macromolecules (yellow shaded), all fundamental energies converge and delicately interplay to bring about deterministic effects (Figure adapted from [89]).

1.2 The Biological Systems

Like trains and their tracks, biomolecules can be naively divided into two categories. The 'trains' catalyze function and motion, whereas the 'tracks' are substrates for structure and information. The latter class includes DNA, the biopolymer of genetic information, which acts as a template for RNA polymerase, a mechanoenzyme of the former class that steps along DNA and transcribes it into RNA. The work herein is focused on the mechanics of

a biomolecule from each class (M13 filamentous bacteriophage and kinesin, Fig. 1-4) and, specifically, how these mechanics translate to important biological function. Each class has a distinct set of biologically-important, mechanical responsibilities, and thus we apply distinct experimental frameworks for understanding them. The natural mechanical framework for our filamentous molecule is classical rod bending, which is derived from continuum mechanics (Fig. 1-5, left panel), whereas mechanochemistry is the appropriate framework for describing the kinetics of a mechanoenzyme, such as kinesin (Fig. 1-5, right panel).

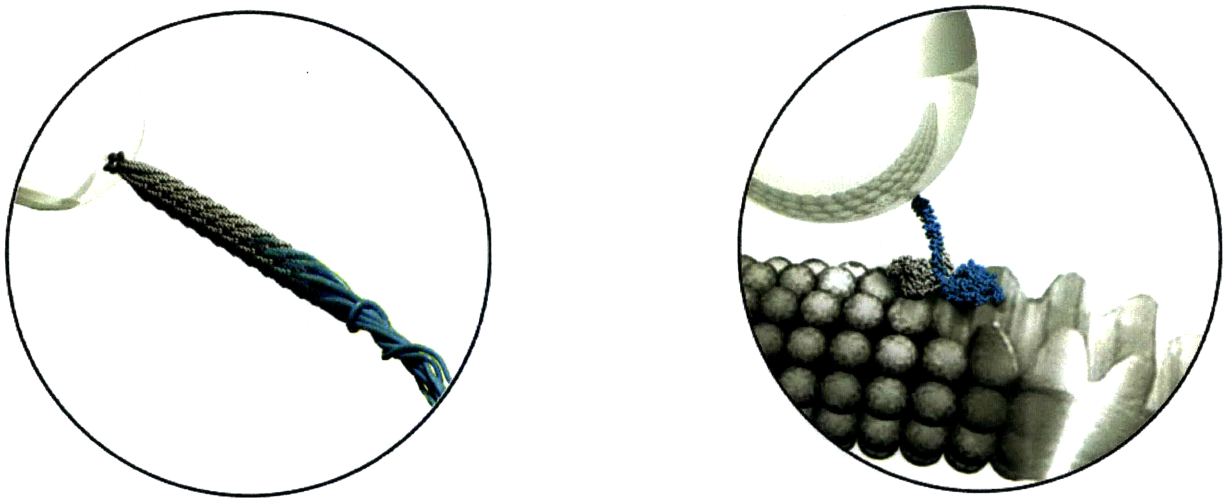

Figure 1-4: The biological systems: M13 bacteriophage (biology's wire) and kinesin (biology's motor).

1.2.1 M13 Bacteriophage: Biology's Wire

First discovered in the sewers of New York City [96], Ff filamentous bacteriophage is a family of viruses that infects *Escherichia coli* (*E. coli*) and non-lytically employs the bacterial host to produce and assemble progeny phage particles. It is structurally hierarchical: a single-stranded viral genome is encapsulated by five, different proteins that arrange into a helical-pitched, cylindrical capsid (Fig. 1-6). M13 capsid proteins can be modified by genetic engineering of the viral genome. Furthermore, since each particle carries its own genetic information, the capsid can be used to display combinatorial peptide libraries for the purpose of screening and identifying binding partners to targets in a technique commonly known as phage display. Recent efforts to expand the repertoire of targets to inorganics have

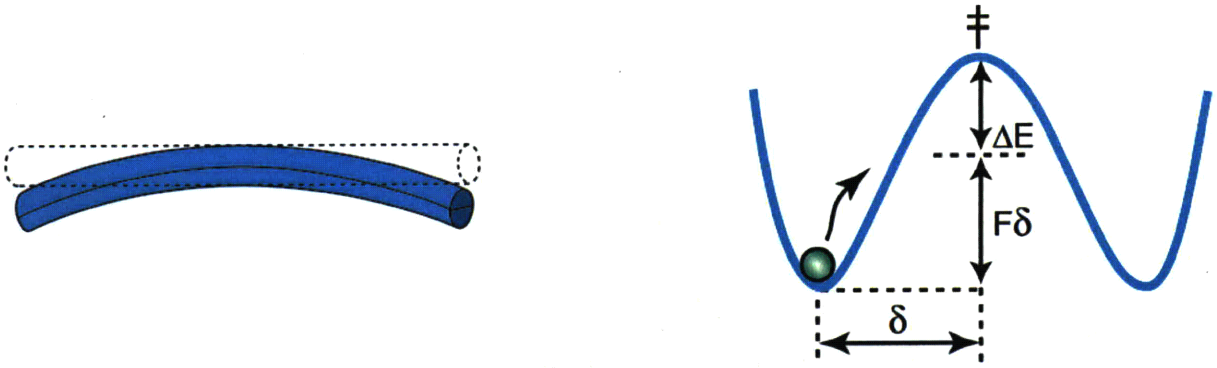

Figure 1-5: Natural mechanical frameworks: rod bending mechanics for M13 bacteriophage (left panel) and mechanochemistry for kinesin (right panel). The application of force can be used to probe the bending and stretching response of biopolymers, such as M13, as well as to selectively modulate the kinetic rates of mechanoenzymes, such as kinesin, by tilting the molecule's reaction coordinate.

revealed biomolecules that are capable of organizing and growing inorganic materials [118]. These biomolecules have been subsequently displayed onto the M13 capsid to engender viral scaffolds of nanowires, structures, and devices (Fig. 1-7) [66, 67, 76].

1.2.2 Kinesin: Biology's Motor

Kinesins are the smallest known processive motors, walking along unidirectional microtubule tracks in an ATP-dependent fashion. They are model systems for understanding molecular motility and are responsible for powering fundamental intracellular processes, such as organelle transport and cell division. Conventional kinesin (Kinesin-1) is a dimer of two, identical heavy chains (Fig. 1-8). At the N-terminal of each monomer is a motor domain that is responsible for microtubule-binding and catalytic activity. The motor head is connected to a C-terminal cargo-binding domain by a long α-helical stalk, which mediates dimerization by forming a coiled-coil. The catalytic core is strikingly conserved among different motor proteins. Indeed, kinesins and myosins share structural similarities in their cores, with analogous nucleotide sensing machinery [56, 111]. Yet, they walk on different cytoskeletal filaments, perform a variety of different cellular tasks, and, even within their respective

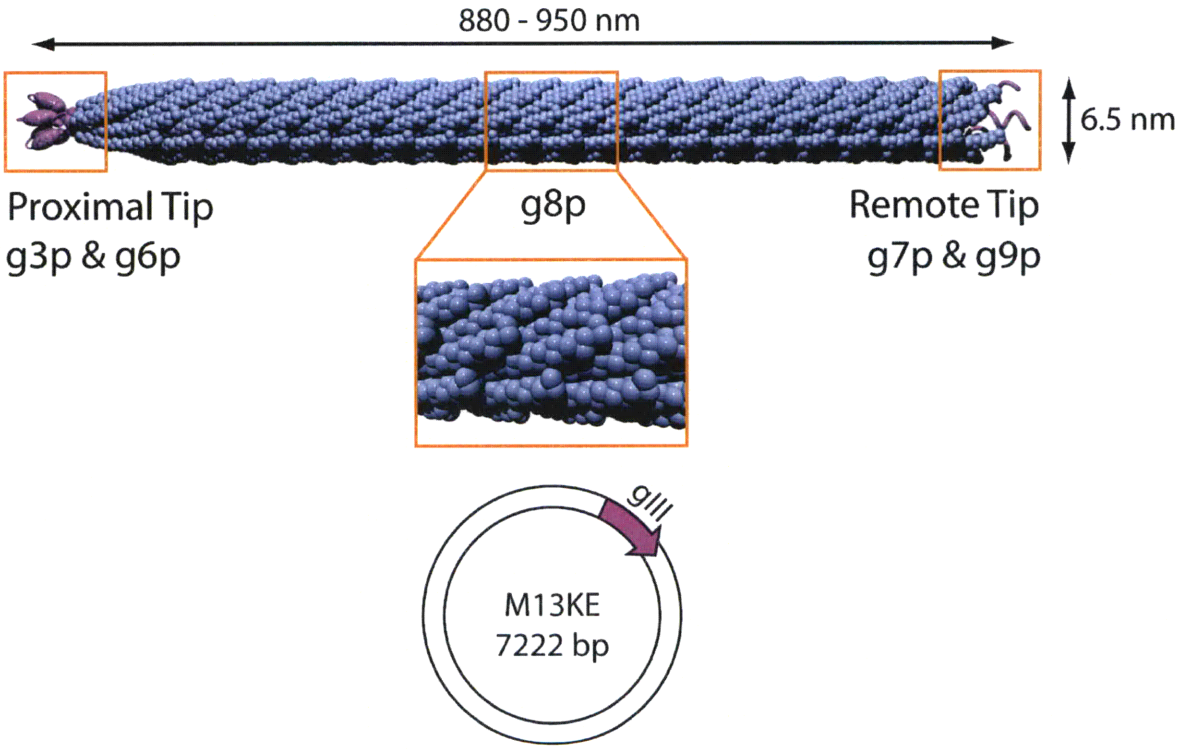

Figure 1-6: Structure of M13 bacteriophage. The proteinaceous capsid is composed of roughly 2700 copies of the *gene VIII* protein (g8p), arrayed in a helical-pitched cylinder, and capped with approximately five copies each of g3p and g6p at one end and five copies each of g7p and g9p at the other end. Packaged within the coat is a single-stranded viral genome, which is necessary for replication and production of progeny, and from which many cloning vectors have been created to yield functional display of peptides and proteins on all five M13 coat proteins.

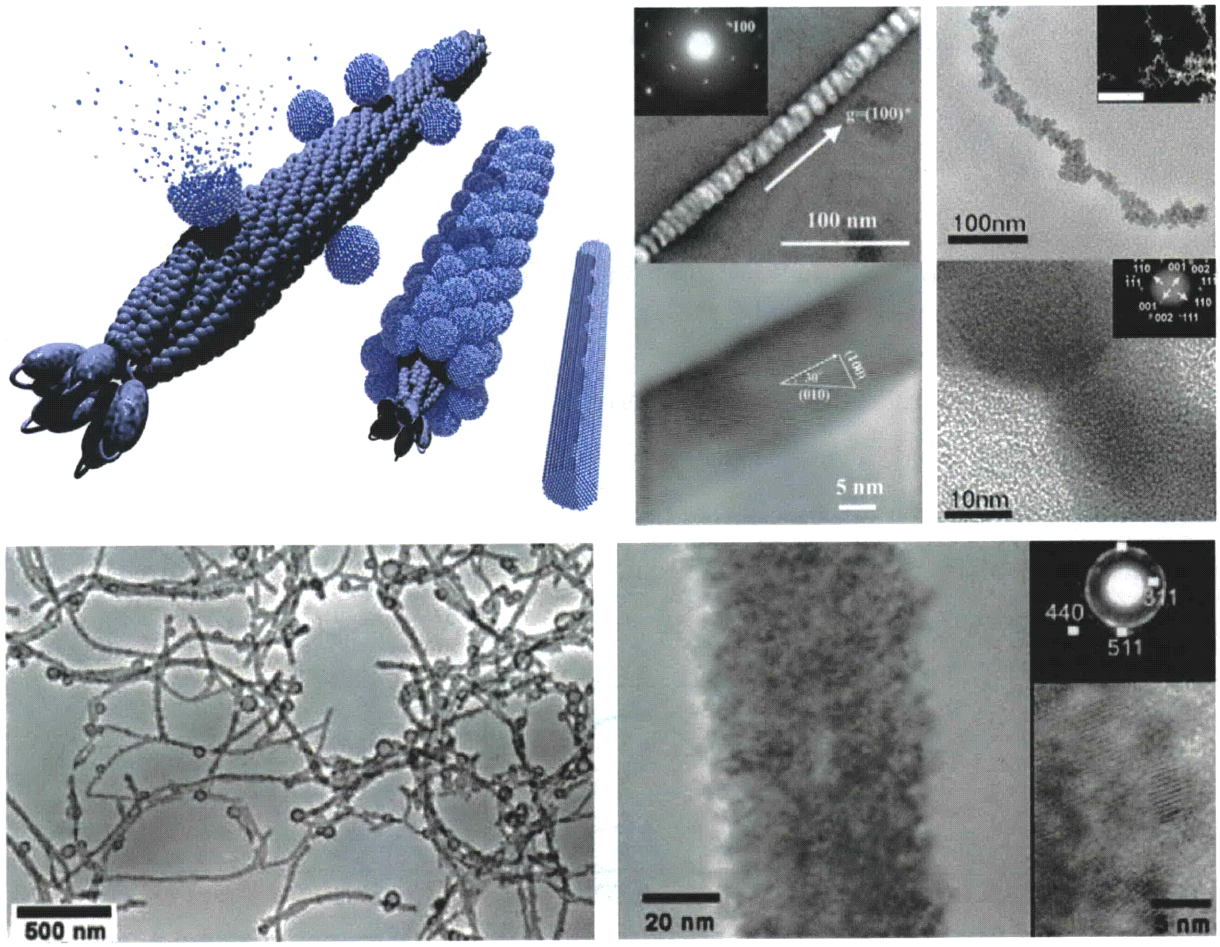

Figure 1-7: M13-based nanowires. M13 provides a system, whereby one can store information about the assembly of materials within the viral genome. The material-specific peptides, which are subsequently displayed on the capsid, facilitate nanowire synthesis. This process, which involves the nucleation, ordering, and annealing of inorganic materials, is visually represented (top left) and has been demonstrated for semiconducting (ZnS) and magnetic (CoPt) nanowires (top right) [67], as well as for Co_3O_4 wires for use in lithium ion battery electrodes (bottom) [76].

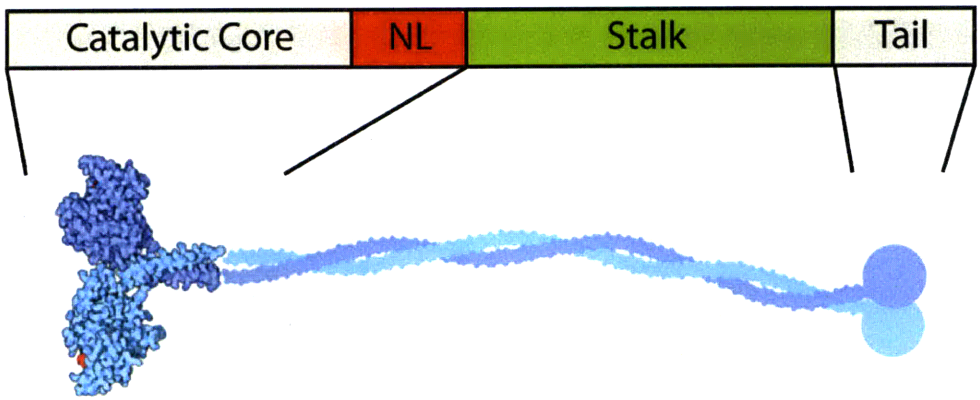

Figure 1-8: Structure of Conventional kinesin. The motor protein is homodimeric, with each monomer comprised of a motor head domain, a short neck linker (NL) that connects the head to a long, α-helical stalk, and a C-terminal domain for cargo binding.

superfamilies, display different motile properties. These motors, therefore, appear to have adopted commonly-used, ancestral nucleotide sensing machinery, yet differentially evolved their energy transduction machinery that converts the chemical energy of ATP-related events into mechanical work. In particular, molecular details of the force generation mechanism of kinesin is not known (Fig. 1-9).

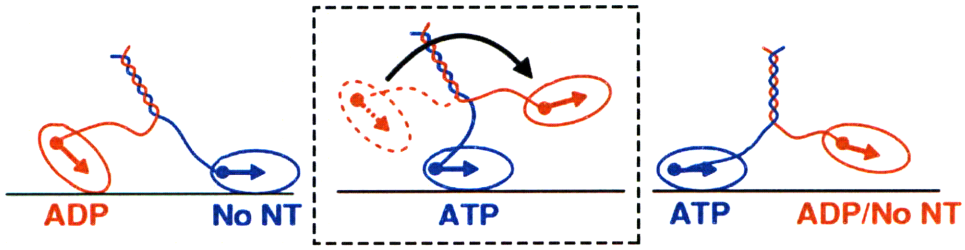

Figure 1-9: Mystery of the kinesin power stroke. The broad features of kinesin's mechanochemical cycle are understood, however, the molecular events that lead to force generation and the forward motion of the trailing head (boxed) have been a mystery (Figure adapted from [45]).

1.3 The Single-Molecule Methods

The breadth of current techniques for manipulating single molecules, spanning six orders of magnitude in length ($10^{-10} - 10^{-4}$ m) and force ($10^{-14} - 10^{-8}$ N), is as vast as the biological systems investigated. Table 1.1 provides an overview of the three most common techniques

Table 1.1: Overview of single-molecule manipulation methods. Adapted from [79].

Methods	Force range (pN)	Spatial resolution (nm)	Stiffness (pN/nm)	Applications
AFM	$10 - 10^4$	$0.5 - 1$	$10 - 10^5$	High-force pulling Bond strength
Magnetic tweezers	$10^{-3} - 10^2$	$5 - 10$	$10^{-3} - 10^{-6}$	Tethered assay DNA dynamics & elasticity
Optical tweezers	$0.1 - 100$	$0.1 - 2$	$0.005 - 1$	Tethered assay Motor proteins

(AFM, magnetic tweezers, and optical tweezers) and their applicability. Optical tweezers are perhaps the most versatile of single-molecule manipulation techniques, with the capacity of exerting forces upward of 100 pN, while measuring sub-nanometer displacements in three dimensions, and are thus the choice for experimental work herein.

On the theoretical side, modeling the mechanics of single molecules requires concepts from various disciplines. For instance and as mentioned earlier, to describe M13-like polymers, we borrow ideas from continuum mechanics and apply them in a statistical mechanics framework. For kinesin, we are interested in mechanics insofar as it reveals information about the molecule's motility. This requires a mechanochemical treatment of molecular transition states and reaction coordinates. The various models derived and applied are described in greater detail within.

1.3.1 Optical Trapping

Shortly after the discovery of the laser, it was shown that the momentum carried by photons of a focused argon laser can be imparted to microscopic dielectric particles with a measurable effect [5]. In particular, a focused laser beam can be used to trap microscopic objects in a three dimensional potential well. This potential well, more colloquially known as an *optical trap* or *optical tweezers*, is the result of gradient restoring forces that are best described by geometric optics in the *ray optics regime* (i.e., when the object's dimension d is much larger than the wavelength of trapping light: $d \gg \lambda$) and by electromagnetic dipoles in the *Rayleigh regime* (i.e., $d \ll \lambda$). Practically, most applications involving micrometer-sized particles and

near infrared laser light involve an approximate combination of the two regimes. Nonetheless, it is useful and informative to provide a short description of optical forces generated from both regimes.

In the ray optics regime, the gradient forces that collectively make up the optical trap arise from momentum differences between refracted light rays of different intensity. This momentum transfer upon refraction produces lateral as well as axial restoring forces that seek to stably trap an object in the focus of a trapping laser, as depicted in Fig. 1-10. Of course, some fraction of incoming light is reflected rather than refracted, producing a scattering force that would tend to push objects out of the focus along the $+z$-direction. Successful trapping is achieved when the gradient force cancels out the scattering force. Mathematical descriptions for the gradient and scattering forces impinging on a sphere have been previously derived [94].

In cases where the diameter of the particle is significantly smaller than the wavelength of light, the particle is treated as a point dipole in an inhomogenous electromagnetic field. The force acting on a single charge in an electromagnetic field is the Lorentz force, which can be written as

$$\mathbf{F}_g = \frac{1}{2}\alpha \nabla E^2 \tag{1.1}$$

where E is the magnitude of the electric field and α is the polarizability of the object. Since the square of the magnitude of the electric field is equal to the intensity of the beam as a function of position, we find that, indeed, dielectric particles are attracted to the region of maximum light intensity along the gradient.

A schematic of our custom-built, optical trap apparatus is shown in Fig. 1-11. For a detailed treatment of optical trap development, including optical design and layout, position detection schemes, and calibration techniques, the reader is referred to [78, 33, 16].

1.4 Scope of Work

This thesis is broadly concerned with the mechanical features of M13 bacteriophage and kinesin. In particular, we believe that a better understanding of filamentous bacteriophage mechanics is crucial to the continued development of M13-based materials and technologies.

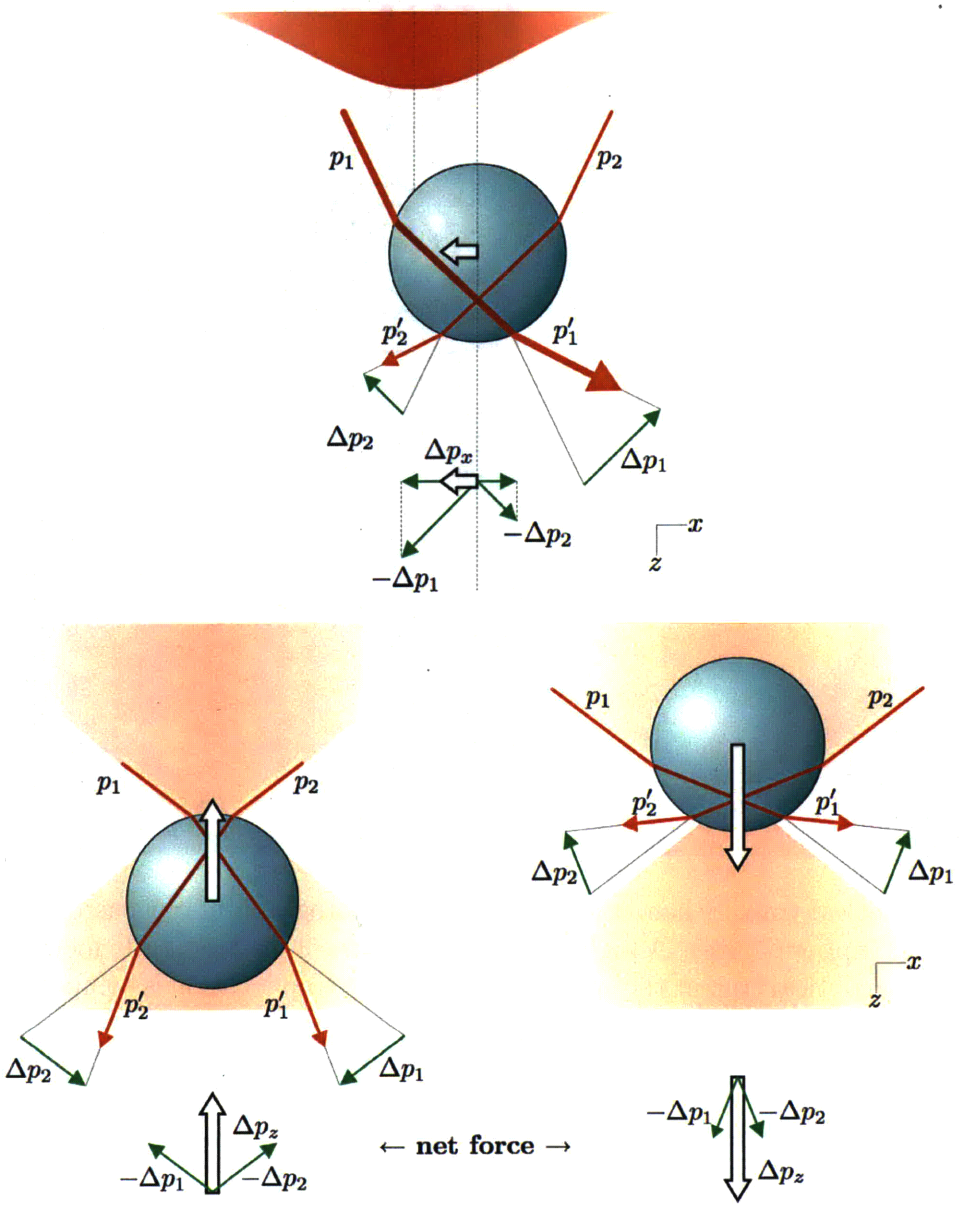

Figure 1-10: Optical gradient forces. The lateral gradient force toward maximum light intensity (top) and the axial gradient force toward the beam focus (Figure reproduced from [112]).

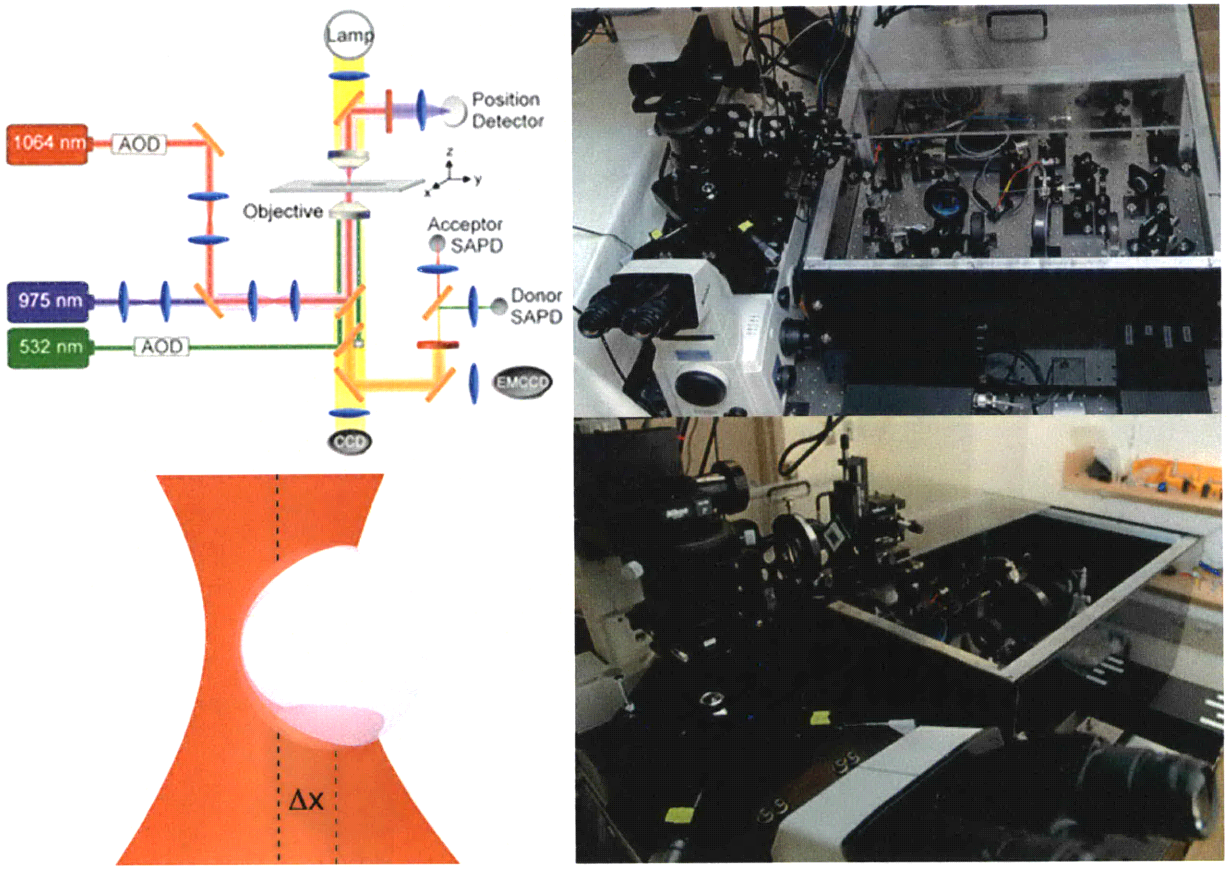

Figure 1-11: Optical trap. Schematic and top-down photograph of our custom-built optical trap apparatus (upper panels). A high numerical aperture objective tightly focuses a 1064 nm laser to form the optical trap at the specimen plane. The trap location is computer-controlled by a pair of orthogonally oriented acousto-optic deflectors (AODs), and the positioning of the specimen is manipulated by a nanometer-resolution piezo-electric stage. The combination of a 975 nm laser and a position sensitive device (PSD) is used for position detection of trapped particles (bottom right panel, photograph of the position detection branch). Specifically, we employ a technique, known as back-focal-plane interferometry, whereby interference patterns in the back focal plane between the outgoing laser light and the scattered light from the trapped particle are imaged onto the PSD and used to calculate lateral displacements of the particle from the trap center. Since the optical trap is modeled as a harmonic potential, these particle displacements correspond directly to the force exerted on the particle (bottom left panel).

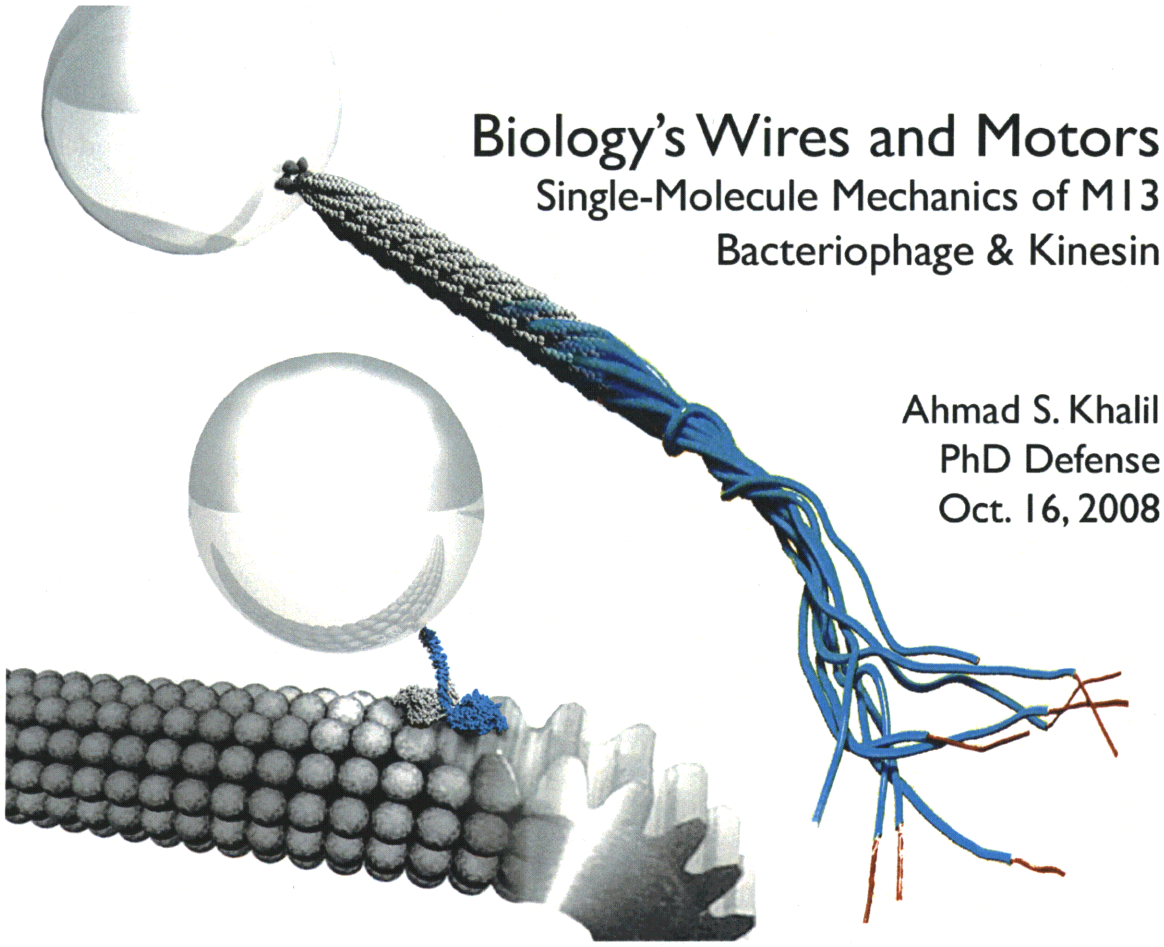

Figure 1-12: Biology's wires and motors.

Furthermore, we believe that a more complete mechanism for kinesin's step is fundamental to elucidating biological motility and dynamics. These topics are addressed with a methodology that combines, on the one hand, molecular biology techniques for modification and control and, on the other hand, high-resolution measurement and modeling.

Chapter Two describes the single-molecule tethering and stretching of M13 bacteriophage, which lead to characterization of the polymer's mechanical properties. Additionally, they reveal M13 to be a potentially simple and robust scaffold for constructing handles to biomolecules for single-molecule study, an effort that is reported in Chapter Three. Finally, Chapter Four summarizes the simulations and experiments that lead to a novel model for the force generation mechanism of kinesin.

Chapter 2

Single M13 Bacteriophage Tethering and Stretching

2.1 Summary

The ability to present biomolecules on the highly organized structure of M13 filamentous bacteriophage is a unique advantage. Where previously this viral template was shown to direct the orientation and nucleation of nanocrystals and materials, here we apply it in the context of single-molecule biophysics. Genetically engineered constructs were used to display different reactive species at each of the filament ends as well as along the major capsid, and the resulting hetero-functional particles were shown to consistently tether microscopic beads in solution. With this system, we report the development of a novel single-molecule assay based on M13 bacteriophage. We also report the quantitative characterization of the biopolymer's elasticity using an optical trap with nanometer-scale position resolution. Expanding the fluctuating rod limit of the wormlike chain to incorporate enthalpic polymer stretching yielded a new model that accurately captured the full range of extensions. Fits of the force-extension measurements yielded a mean persistence length of approximately 1265 nm, providing single-molecule evidence in support of a filamentous bacteriophage persistence length shorter than previously thought. Furthermore, a predicted stretching modulus roughly two times that of double-stranded DNA, coupled with the system's linkage versatility and load-bearing capability, makes the M13 template an attractive candidate for use in tethered

bead architectures. This chapter was reproduced from [49].

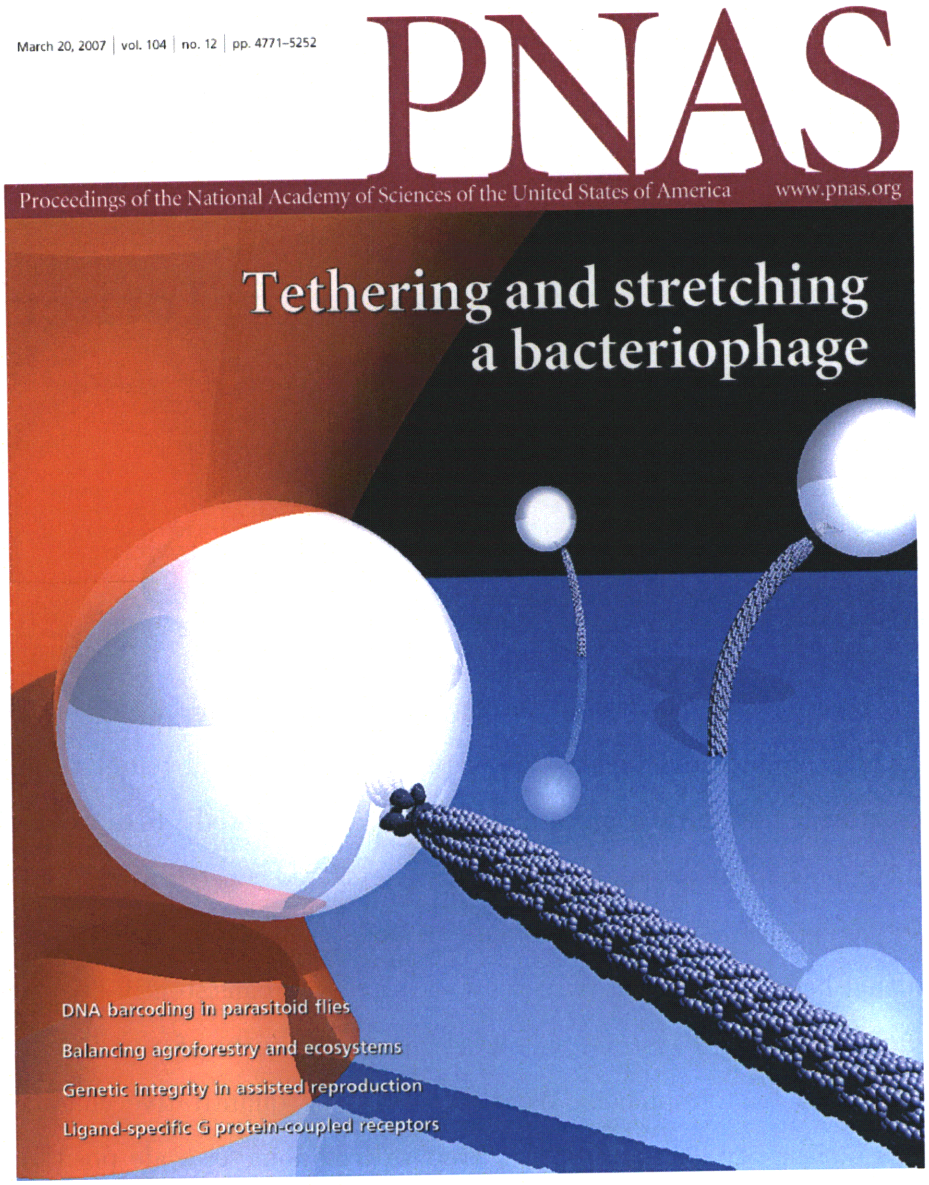

Figure 2-1: Tethering and stretching a bacteriophage (journal cover illustration).

2.2 Introduction

The Ff class of filamentous bacteriophage, comprising the structurally akin species f1, fd, and M13, has elicited the interest of many wide-ranging scientific disciplines on account of

its self-assembling nature. Protected and transported within the highly organized, protein-based capsid is the structural and assembly information necessary for its own production. This provides a direct and accessible link between phenotype and genotype, a feature, which particularly in the case of M13 bacteriophage, has proven advantageous for numerous studies and applications. For instance, combinatorial libraries of polypeptides can be fused to M13 coat proteins, in a technique known as phage display, as a means of screening binding candidates against targets [117]. Recently, targets have been extended beyond biologicals to a wide variety of inorganics, in efforts to discover biological systems capable of organizing and growing materials [118]. In addition to serving as the vehicle for displaying these ligands, the unique structure of M13 itself has been exploited as a biological template for nanotechnology, such as in the directed synthesis of semiconducting/magnetic nanowires and lithium ion battery electrodes [66, 67, 76]. Considering its utility as *both* a genetic blueprint and structural backbone for materials and device architecture, a better understanding of its mechanical behavior and a novel means of actively assembling M13 can greatly advance the design of future M13-based materials.

M13 bacteriophage is a high-production rate virus composed of five different, modifiable proteins, the vast majority of which is major capsid *gene VIII* protein (g8p). Approximately 2700 copies of this 50 amino acid monomer encase the virion's single-stranded DNA during assembly in *E. coli*, forming a helical-pitched cylinder that is 7 nm in diameter [84]. Joined at one end of the cylindrical particle are typically 5 copies of small, minor coat g7p and g9p (the *remote tip*), and at the opposite infective end, 5 copies of g3p and g6p proteins (the *proximal tip*). Both end complexes are tightly packaged and contribute little to the wild-type length of 880-950 nm [80].

Control over the composition and assembly of M13 bacteriophage is not limited to the single particle level. At critical concentrations and ionic solution strengths, filamentous bacteriophages undergo transitions into various liquid crystalline phases [2], which have subsequently been exploited as macroscale templates for organizing quantum dot nanocrystals [61]. These phase transitions result from purely entropic effects, typically from competition between rotational and translational entropy [83]. Thus, an accurate depiction of M13 elastic properties and degrees of freedom is crucial for phase transition modeling and prediction.

In the pioneer application of optical trapping to biological systems, Ashkin and Dziedzic lured and manipulated tobacco mosaic virus with laser light [6], unlocking a flood of subsequent light-based studies of cells, proteins, and single molecules [106, 71]. To our knowledge, the efforts to optically trap and study single viruses have not continued with the same rigor of, for instance, DNA. Nevertheless, these efforts could provide interesting, new platforms for single-molecule (SM) biophysics, which remains heavily reliant on a few, accessible assays, such as the gliding filament, the tethered bacterium, and the tethered bead [11]. In this report, we merge advances in genetic engineering of M13 capsids with SM instrumentation to unlock a new SM tool. Additionally, we demonstrate that M13 can be a *strong* and *versatile* biopolymer alternative to dsDNA in constructing the instrumental tethered bead assay.

The developed M13-based assay additionally provides a new means of investigating unknown or contentious filamentous bacteriophage mechanical properties. Doubt over previously reported persistence lengths, for instance, was cast from recent investigations into the interaction of colloidal microspheres in suspensions of bacteriophage "rods" [62]. Deviations between depletion attraction measurements and "rigid-rod" theories were resolved when rod flexibility was introduced in the model, and persistence lengths 2-3 times smaller than the commonly cited value of 2.2 μm were ultimately suggested [60]. Indeed, longer persistence length values, obtained from dynamic light scattering (DLS) of bacteriophage solutions, have drawn question. For instance, spontaneous nano-ring formation was readily observed when M13 remote and proximal tips were functionalized with hexahistidines (H_6) and divalent cations, respectively [77]. Even without modification, intricate, close-packed, circular structures were assembled from M13 films on thin polymer multi-layers [126].

In this report, we first demonstrate a robust and tunable method for generating M13 tethers in solution. Next, we investigate the SM elasticity via optical tweezers stretching and modify the appropriate limit of the wormlike chain (WLC) model to accurately capture force-extension (F-x) measurements. Finally, we discuss significant features and extensions of this new system.

2.3 Results

2.3.1 Tethering

Once the genetic constructs encoding for modified forms of specific capsid proteins were engineered, phages expressing the desired polypeptide sequences were readily amplified in bacterial hosts. For the majority of our stretching measurements, we designed hetero-bifunctional phages (termed *B*-H_6), displaying H_6 epitopes at remote tips and biotin molecules linked through selenocysteines (Sec) at proximal tips. Guided by the established protocols for SM dsDNA studies [59], a procedure for suspending *B*-H_6 phage in solution between antibody-functionalized coverslips and streptavidin-coated polystyrene microspheres was developed (Fig. 2-2). This procedure was robust and repeatable, generating roughly 20-40 tethered beads and minimal nonspecifically immobilized beads per visual field of view (110 μm $\times$ 110 μm).

The M13 genome provides a convenient platform for displaying and interchanging functional groups at M13 tips and the major capsid. Three variant constructs were genetically designed and substituted into the developed assay. In each, biotin molecules at proximal tips were replaced with short *S*1 peptides (WDPYSHUQHPQ) carrying the HPQ motif, which is known to bind streptavidin with micromolar affinity [98]. The first construct (*S*1-H_6) yielded analogous arrays of tethered beads, possessing surprisingly high stability and strength (as demonstrated below). To the *S*1-H_6 genome, peptide markers were additionally cloned upstream of the g8p N-terminus to give two, different hetero-trifunctional phages. The first, *S*1-#9-H_6, was endowed with a known gold-binding octamer (VSGSSPDS) on each copy of g8p, such that nanoparticle-mineralized capsids were observed after incubation with 5 nm gold colloidal solution (Fig. 2-2C) [42]. As illustrated in the transmission electron microscopy (TEM) image of Fig. 2-2C, there is a single mode of assembly, where only the proximal tip is adapted to bind beads. The second trifunctional construct, *S*1-*E*4-H_6, was designed to present negatively charged tetraglutamate species (AEEEEPDA) at each g8p N-terminus. The localized negative charge coordinates divalent cation and certain inorganic material precursors, and, in particular, has been shown to nucleate single crystal Co_3O_4 nanowires [76]. Following identical procedures, this construct analogously tethered beads in

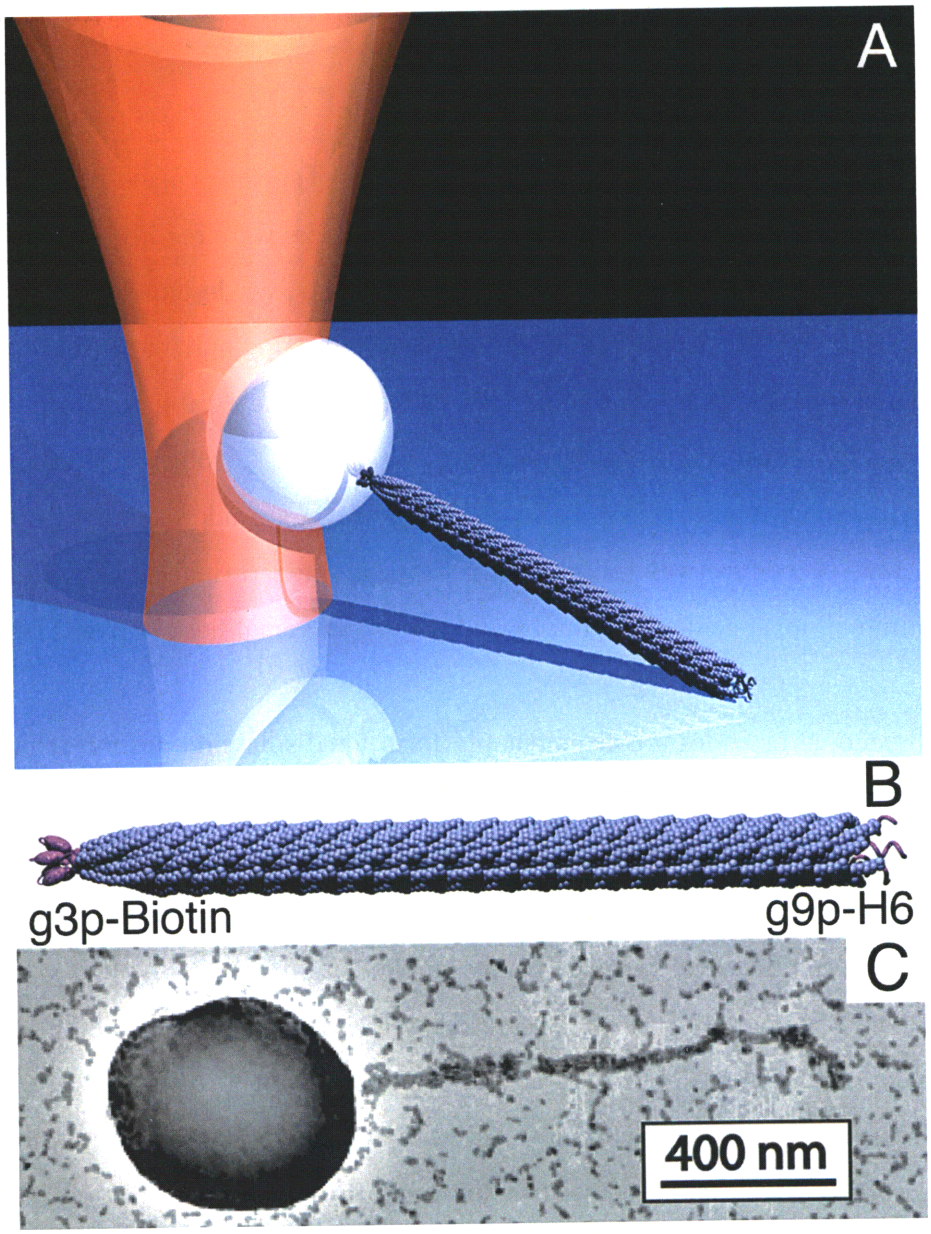

Figure 2-2: Single M13 bacteriophage stretching and engineering. (A) Rendering of M13 bacteriophage stretching by an optical trap (not to scale). (B) Major capsid g8p monomers form an ordered helical shell that encases its ssDNA. The g8p coat was reconstructed from x-ray fiber crystallographic data (PDB number 1ifj). The end complexes (identified in purple) consist of several copies of genetically modifiable g9p and g3p monomers. In *B-*H_6 phages, H_6 tags were fused to g9p via plasmids inserted into bacterial hosts. Each copy of g3p was biotinylated after encoding for a selenopeptide fusion directly into M13's *gene III* (not to scale). (C) A TEM image of the assembly architecture, where a gold-binding peptide was fused to g8p monomers for gold nanoparticle incorporation along the length of the capsid (note that bead is larger than beads used for stretching).

solution. In essence, the location and moiety to which the M13 construct binds is tunable, extending even to inorganic materials.

2.3.2 Stretching

The elastic properties of M13 are critical to its use as a SM tool, nanotechnology assembly vehicle, or liquid crystal building block. In an effort to characterize them, single M13 molecules were stretched with a high-resolution optical trap using procedures similar to those of [116] for short dsDNA tethers (see Materials and Methods). Briefly, 440 nm diameter polystyrene beads, affixed to proximal ends of M13, were trapped by the optical gradient forces of a tightly focused laser beam and positioned a set height above the coverslip surface. The piezo-electric stage was then translated laterally while bead displacements from the trap center were recorded, and, with the necessary calibrations [106], these results were converted to F-x measurements.

Stage-based stretching of M13 molecules with optical trap stiffness in the range of 0.25-0.35 pN/nm gave F-x measurements from fractions of a pN up to 30-40 pN. Despite its hierarchical structure, M13 F-x behavior was reminiscent of typical WLC biopolymer stretching curves (Figs. 2-3,2-4). In fact, plotted alongside a typical F-x curve for a 3500-bp dsDNA molecule, stretched using identical procedures, the M13 response appears very similar to that of dsDNA, albeit much stiffer (Fig. 2-3). After a small entropic elasticity regime, the thermal random-walk fluctuations governing the filament's shape are stifled and its end-to-end distance approaches its contour length, or the B-form length in the case of dsDNA. Just before the molecule reaches its contour length, it begins to display compliance and enthalpic stretching, or simply linear elasticity, governs this higher-force regime that accounts for actual polymer extension.

While more work is needed to properly characterize and identify where M13's enthalpic stretching regime breaks down, a preliminary investigation at higher forces showed that M13 experiences no abrupt transitions, as does dsDNA at 60-65 pN to an "overstretched" form (Fig. 2-4A) [103]. In all instances, the F-x response was reversible and showed no plasticity, permanent deformation, or even force plateau through loads of 70 pN, the maximum achievable force given our experimental conditions, namely where the trap's linearity remained

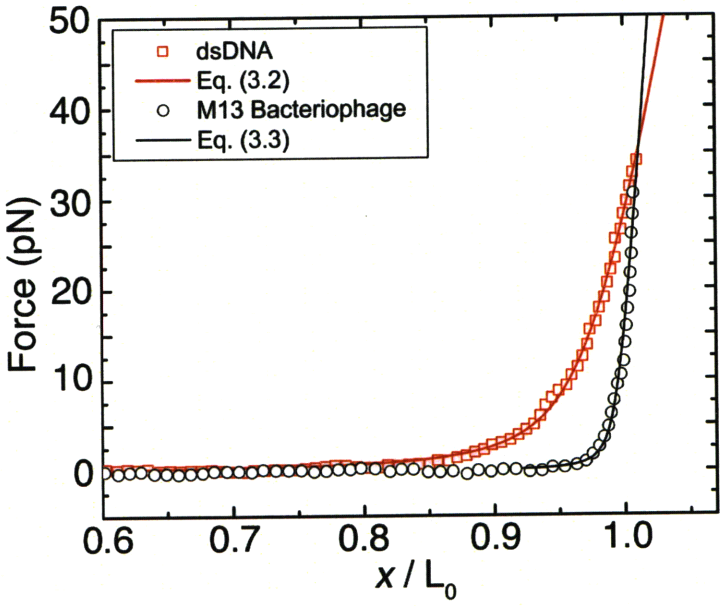

Figure 2-3: F-x comparison of M13 bacteriophage and dsDNA. A typical F-x measurement for M13 bacteriophage (open circles) with corresponding fit, using Eq. (2.3), overlayed on the data. A modified form the WLC's fluctuating rod limit was developed to describe the full range of extensions. The M13 behavior is suggestive of a stiffer analog to dsDNA, for which a typical F-x measurement (open squares) is plotted along with its corresponding fit using the modified Marko-Siggia form of Eq. (2.2). Average DNA parameters, l_p = 42.1 $\pm$ 2.9 nm, K = 1016.0 $\pm$ 180.2 pN, and L_0 = 1185.7 $\pm$ 19.4 nm, extracted from a set of 5 independent molecules agree well with previous literature values and theoretical 3500-bp contour length, validating our experimental stretching procedures.

trustworthy. Higher forces were attained by increasing the laser power delivered to the specimen and, in some cases, substituting larger beads (984 nm diameter) in place of 440 nm beads to increase the instrument's potential force generation.

2.3.3 Modeling

The mechanical properties and fluctuations of semiflexible polymers are widely modeled and well described by the WLC [54]. Here, the configuration of a polymer is represented by a space curve of fixed, zero tension contour length, L_0, with a bending energy that is quadratic in the chain curvature. External forces stretching WLC polymers, therefore, do work against the conformational entropy of the chain [69]. With space curve, $\mathbf{r}(s)$, parameterized by the polymer's arc length s, the chain's curvature is simply $\kappa = |\partial^2\mathbf{r}(s)/\partial s^2| = |\partial\hat{\mathbf{t}}(s)/\partial s|$, where $\hat{\mathbf{t}}(s)$ is the unit vector tangent to the chain. The resulting elastic energy, E, of a WLC polymer being mechanically stretched by a uniaxial force is

$$\frac{E}{k_BT} = \int_0^L \frac{l_p}{2}\kappa^2\, ds - \frac{F}{k_BT}x\,, \tag{2.1}$$

where x is the total extension of the chain, l_p the persistence length, k_B the Boltzmann constant, T the absolute temperature, and F the force. The persistence length is the characteristic length scale over which thermal fluctuations begin to dominate the orientation of the chain's tangent vectors.

Using a statistical mechanical treatment of the WLC, the equilibrium extension and other relevant thermodynamic variables are evaluated from the Boltzmann distribution e^{-E/k_BT}. In the long polymer limit, Marko and Siggia derived an interpolation formula [69] that has been widely employed to model stretching data, such as that of dsDNA [104]. The modified Marko-Siggia form,

$$F = \frac{k_BT}{l_p}\left[\frac{1}{4(1-x/L_0+F/K)^2} - \frac{1}{4} + \frac{x}{L_0} - \frac{F}{K}\right], \tag{2.2}$$

accounts for enthalpic elongation and was used to capture a broader range of extensions, ultimately predicting dsDNA persistence lengths of 40-50 nm and elastic stretching modulus,

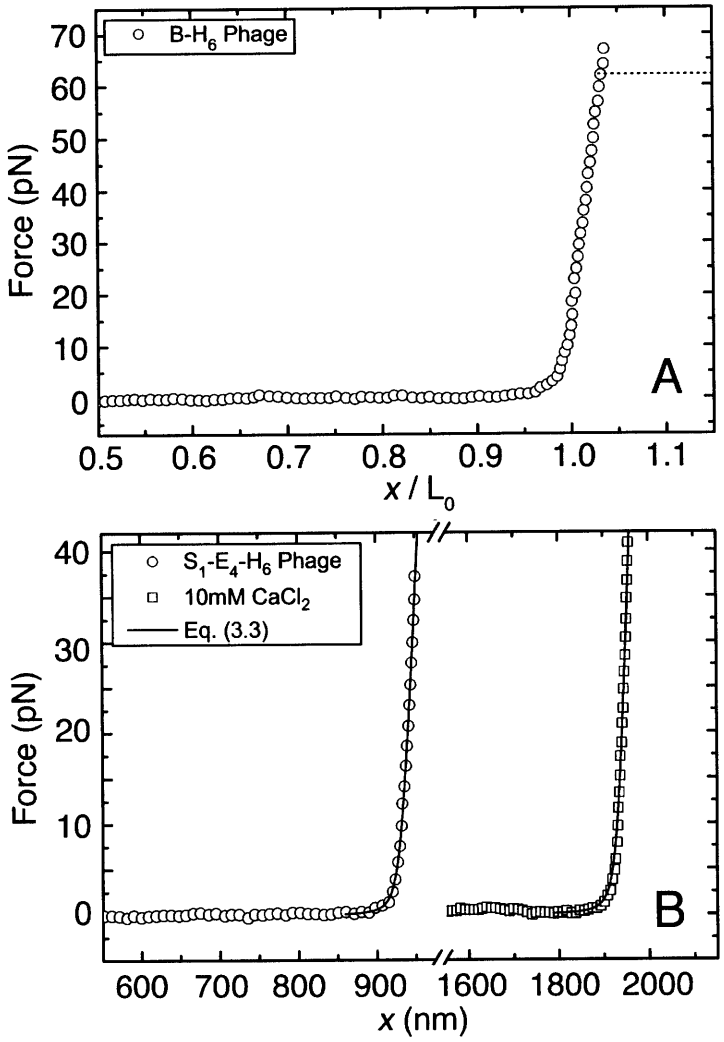

Figure 2-4: Mechanical features and extensions of the M13 system. (A) The F-x behavior of M13 loaded up to 70 pN is fully elastic, exhibiting no transitions or permanent deformation, unlike that of dsDNA, which exhibits an abrupt force plateau at 60-65 pN (dashed line) to an "overstretched" form. (B) When modified to display streptavidin-binding $S1$ peptides on g3p and tetraglutamate peptides on g8p, the mechanics of the $S1$-$E4$-H_6 variant remained robust and comparable to that of B-H_6 phage. Interestingly, the tethered system remained intact for relatively large loads due to its ability to express multiple copies of the linking peptides at each filament end. In the presence of 10 mM $CaCl_2$, negatively-charged $S1$-$E4$-H_6 phage was induced to form lateral bundles, which were manifested as much longer tethers in their F-x measurements.

K, of 1000-1100 pN [116]. As indicated above, to validate our experimental methods, 3500-bp dsDNA was prepared and stretched using identical procedures to those of M13 phage. A small dataset ($N = 5$) of F-x measurements were generated and fit to Eq. (2.2). The resulting parameters, $l_p = 42.1 \pm 2.9$ nm, $K = 1016.0 \pm 180.2$ pN, and $L_0 = 1185.7 \pm 19.4$ nm, agreed well with previous predictions as well as with the theoretical contour length of 1183 nm (using 0.338 nm/bp), thus confirming our procedures.

The thermodynamic limit of $L_0 \gg l_p$ is not valid for filamentous bacteriophage, thus Eq. (2.2) is inapplicable for describing its mechanics. Instead, the WLC must be solved with the appropriate boundary conditions to account for finite-length effects. In general, this is a difficult task, however, an analytical solution exists for the equilibrium extension of polymers with contour length of the order of, or shorter than, persistence length ($L_0 < 2l_p$). In this fluctuating rod limit, thermal undulations in the chain appear increasingly smoothed out as compared with random-walk polymers [119]. With tangent vectors making only small deviations away from the direction of the force, a harmonic approximation can be taken and the generating functional method used to obtain the average extension [41].

Inspired by the approach of Odijk [81], we have modified this solution to include a stretching term that allows us to model the full range of bacteriophage extensions. An effective stretching energy that is quadratic in the polymer's elongation, $E_e = \int_0^L \frac{1}{2} K \left(s/s_0 - 1\right)^2 ds$, was added to Eq. (2.1). In the case of small elongations, the resulting average extension is

$$x = L_0 - \frac{k_B T}{2F}\left[L_0\sqrt{\frac{F}{A}}\coth\left(L_0\sqrt{\frac{F}{A}}\right) - 1\right] + \frac{FL_0}{K}, \tag{2.3}$$

where $A = l_p\, k_B T$ and K is an elastic stretching modulus [41, 47]. Here, the end tangent vectors are assumed to be collinear with the force, consistent with our experimental setup, where linkages were engineered from the proximal and remote tips (i.e., from small, pivoting proteins as opposed to the crystalline g8p shell).

A typical fit of a single M13 F-x measurement to Eq. (2.3) is shown in Fig. 2-3, where it is evident that the full range of extensions is generally well described by modified model. In all, stretching curves for 31 different specimens were obtained and fit, and the resulting parameters then averaged to ultimately obtain $l_p = 1265.7 \pm 220.4$ nm, two contour

lengths $L_0 = 939.7 \pm 46.1$ nm and 532.0 ± 20.5 nm, and $K = 2176.2 \pm 656.3$ pN. The full results for l_p and L_0 are pictorially collected in the histograms of Fig. 2-5, where the dual contour length population can undoubtedly be observed. These two lengths corresponded to bacteriophage packaging full M13 genomes and shorter g9p-H_6 plasmids (see Materials and Methods) [117]. The relative frequency of full genome- to plasmid-packaging phages depends on various preparation factors, and the histogram results are not reflective of the true relative populations, particularly because we focused our stretching studies on full-length particles. The corresponding lengths, on the contrary, accurately depict how phage length scales with the number of nucleotide bases in the packaged DNA: 7222 in full M13KE vectors and 3957 in H_6 plasmids.

Average M13 contour lengths are commonly reported between 880-950 nm [117, 8]. To more precisely assess our model-predicted contour lengths, atomic force microscopy (AFM) images were taken of the same B-H_6 sample used for stretching. The contour lengths of 83 different bacteriophages were measured using manual image processing techniques from a total of 10 phase images (5 μm $\times$ 5 μm or 3 μm $\times$ 3 μm). The distribution (shown in the Fig. 2-5B inset) confirms the existence of dual length populations, and the average values of 945.4 $\pm$ 51.8 nm and 542.3 $\pm$ 39.1 nm corresponded well with the values obtained from stretching data.

2.3.4 Features and Extensions of the System

Variant M13 constructs, $S1$-H_6, $S1$-#9-H_6, and $S1$-$E4$-H_6, readily tethered beads in solution when integrated into our SM assay. Force-based studies with these variants elucidated some further, interesting features of the overall system and provided a means of exploring genetically-coupled mechanics.

Stretching of $S1$-$E4$-H_6 revealed, first, that tethers were capable of withstanding respectable forces, of at least 40 pN, despite the use of relatively low affinity interactions with streptavidin beads (Fig. 2-4B). This unique strength can be attributed to the multiple copies of g3p being displayed on the proximal tip of the capsid. As a result, the roughly 5 attachment points between $S1$ and streptavidin are, most likely, sharing the total load and providing an aggregate strength greater than that of the weaker individual bonds. The

linkages in B-H_6 tethers, therefore, are likely to withstand much higher forces than needed to break single biotin-streptavidin or H_6-antibody bonds.

The second result answers the question of what affect an engineered modification in the major coat g8p may have on the filament's mechanics. Preliminary results suggest that $S1$-$E4$-H_6 phage exhibit comparable mechanical properties to those of B-H_6, despite having highly charged tetraglutamate species along its filamentous capsid. Indeed, a set of 4 full-length $S1$-$E4$-H_6 phages yielded an average l_p of 1250.6 ± 164.2 nm, L_0 of 931.6 ± 26.7 nm, and K of 1796.9 ± 367.9 pN.

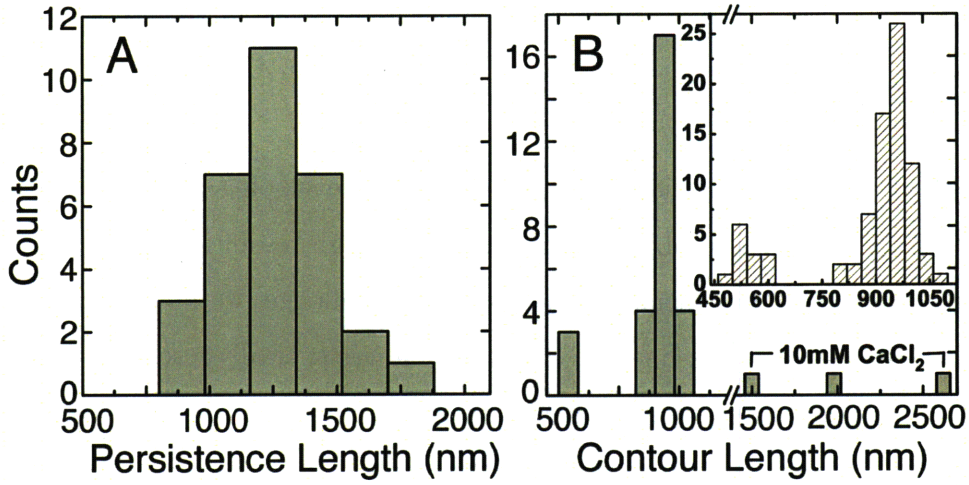

Figure 2-5: Histogram results for l_p and L_0 for the complete set of 31 independent M13 bacteriophage specimens. (A) Persistence lengths centered about an average value of 1265.7 ± 220.4 nm. (B) Contour length values, under standard experimental conditions, revealed dual length populations, with averages 939.7 ± 46.1 nm and 532.0 ± 20.5 nm, corresponding to full and shorter, plasmid-packaging lengths. Occurrences of longer M13 bundles were observed in the presence of 10 mM $CaCl_2$. (Inset) Contour length distributions estimated from high-resolution AFM images of 83 different bacteriophage specimens confirmed the stretching-predicted lengths (L_0 = 945.4 ± 51.8 nm and 542.3 ± 39.1 nm).

Due to their polyelectrolyte nature, M13 and other filamentous bacteriophage can be induced to laterally aggregate into bundles by metal divalent cations [108]. The extra negative charge inherent to $S1$-$E4$-H_6 is advantageous in spurring this phenomenon at lower divalent cation concentrations than typically required (40-80 mM Ca^{2+}). So, we tested whether $S1$-$E4$-H_6 bundles, generated in the presence of a small amount of Ca^{2+}, could also be incorporated into our tethering assay. $S1$-$E4$-H_6 phage was incubated in 10 mM $CaCl_2$ for 30

minutes and then introduced into flow cells with streptavidin-coated beads. While certainly not as prevalent as single M13 tethers, there was indeed evidence of tethered bacteriophage bundles. For instance, Fig. 2-4B illustrates the stretching of one of three long bundles. The corresponding contour lengths of the three specimens, displayed in the histogram of Fig. 2-5B, significantly exceeded those of single bacteriophage and therefore, most likely, could not have corresponded to single particles. It should be noted that additional work is still needed to fully characterize these bundles, such as to test the effect of varying cation concentration on bundle sizes and mechanics.

2.4 Discussion

A significant challenge in SM biophysics research is in developing creative and trustworthy assays to link the biological problem of interest to the high-resolution instruments responsible for detection and manipulation. To address this challenge, we have harnessed a robust protein-based template, possessing the genetic advantages typically reserved for DNA. In particular, M13 bacteriophage provides direct genotypic control over the molecules displayed on it, and, due to its hierarchical structure, these molecules can be targeted to specific locations on the polymer. This feature of excellent physical handle connectivity is advantageous for two reasons. First, versatility is embedded into the system by virtue of the widely studied and modifiable M13 genome. M13KE, a derivative of the M13 genome with cloning sites introduced for fusion to *gene III* (New England Biolabs), and various phagemid vectors are commercially available. With these, reactive peptide epitopes, including the H_6 tag, the hemagglutinin (HA) tag, and cysteine residues, as well as proteins can be fused to g3p, g9p, or g8p [77, 42, 97]. Modes of attachment can, as a result, be diversified, potentially allowing for SM handling of biological species previously unsuited for DNA tethering, such as transcription factors. Furthermore, the displayed molecules need not be solely vehicles for attachment but can also be the species of study. For instance, mechanically interesting proteins, such as dimeric streptavidin, have been successfully expressed on M13 g3p [7]. Conceivably, the M13 template can be made to carry the protein of interest and simultaneously serve as the mechanical tether. Second, in tethered bead assays, binding is restricted to M13

ends, ensuring that tethers of finite length are always generated and that force corrections, due to ill-defined geometries, are small. In experiments with protein biopolymers, such as F-actin, often the strategy is to unselectively biotinylate monomers and hope the desired attachment architecture is obtained in solution. As a consequence, beads tend to bind numerous locations along the filaments, resulting in filament wrapping and unwanted bending contributions during stretching [28].

The M13 system appears well-suited for higher force studies, such as for protein extension and distortion, particularly now that the force capability of optical tweezers is increasing [73]. In contrast to dsDNA, phage showed no deviation from standard entropic/enthalpic stretching when subjected to loads through 70 pN. Nonetheless, in optical tweezers-based studies, dsDNA is commonly used to translate forces to a protein of interest [20]. The M13 template may be better able to communicate these forces because it is stiffer (longer l_p and higher K) than DNA. Furthermore, the M13 template can provide multiple, localized attachments to the species of interest to prevent or delay detachment.

Characterizing filamentous bacteriophage mechanics and flexibility has been a scientific challenge. Thus far, literature values for l_p have been wide-ranging, though this has not been rigorously investigated since the DLS studies of fd and M13 suspensions from over 15 years ago. The often cited value, $l_p = 2.2$ μm, was derived from fitting fluctuations in scattering intensity to theoretical models for Brownian dynamics that are built upon various other models, assumptions, and correction factors [105]. These fits are highly dependent on certain hydrodynamic and structural parameters and are therefore associated with large variances [8]. Furthermore, l_p estimates from electron microscopy images (880 nm - 6 um) are subject to sample preparation artifacts yet have been widely used as standards by which to confirm DLS results [8]. In fact, DLS has been known to give a broad range of predictions for other semiflexible polymers, including F-actin [14]; thus, continuing efforts to reconcile and validate the different techniques are critical.

In this report, the first characterization of the SM elasticity of filamentous bacteriophage was presented. The fluctuating rod limit of the WLC was equipped with an elastic chain stretching term and then used to model optical tweezers stretching data. The extracted mean l_p (1265 nm) supports recent predictions that filamentous bacteriophage lp may be

shorter than previously thought [60]. Additionally, the two expected contour lengths (at full length and g9p-H_6 plasmid length) and a mean K near 2200 pN, approximately double that of dsDNA, were obtained. It should be noted that while the model described F-x measurements well, it may not have captured all of the polymer's complex mechanical behavior. For instance, M13 is a chiral molecule and may also undergo stretching-coupled twisting [68]. It should also be noted that for finite-length molecules, experimental conditions should reflect the desired statistical ensemble, as different ensembles cannot be assumed equivalent [47]. Stage-based stretching, as implemented here, applies a nearly constant force at each increment, consistent with the model's assumed ensemble. In fact, under our experimental conditions, it can be shown that the M13 polymer is in equilibrium. For instance, at trap stiffness lower than that used for stretching, M13 relaxation time was estimated at 0.32-0.37 ms by the autocorrelation of bead position at x/L_0 = .72-.92, negligibly longer than the corresponding time for un-tethered beads, 0.30 ms.

Biopolymer mechanics are intrinsically related to biological function. Microtubules, with mm-long l_p, provide cellular rigidity and structure, actin is responsible for cell motility, while DNA, with short l_p, is easily folded and packaged into chromosomes. Filamentous bacteriophage capsids have the dual responsibility of safeguarding viral DNA as well as locating and binding host receptors during infection. As a result, they are *robust*, yet *adaptable*, structures. We anticipate that the techniques developed for M13 bacteriophage will provide a broadly applicable tool for facilitating future SM studies and for furthering biopolymer modeling and mechanics.

2.5 Materials and Methods

Genetic engineering of capsid proteins

Modification of all M13 capsid proteins is possible. To the N-terminus of each g3p, a short Sec-containing peptide (SARVXHGP where X is Sec) was fused by cloning directly into the M13 genome (M13KE) and amplifying in the presence of 2 μM sodium selenite (*Sec1*) [97]. Compared to cysteine (pK_a = 8.1), Sec has a pK_a of 5.2 and thus can be targeted for

nucleophilic substitution at acidic pH.

Cloning directly into the M13 genome is not as straightforward for g9p modification because of overlapping genes. Therefore, we PCR-amplified a primer encoding for H_6 upstream of the M13 virus *gene IX*. This extended *gene IX* was cloned into a pAK derived phagemid, separate from the full M13 genome, such that the fusion protein was under *lac* promoter control [66, 77]. As a result, bacterial hosts harboring this plasmid were induced to express the fusion protein with 1mM isopropyl β-D-thiogalactopyranoside (IPTG). Upon infection with helper phage (*Sec1*), hetero-bifunctional particles (*Sec1-*H_6), packaging *either* full M13KE genomes or recombinant plasmids, were produced.

Once the desired genetic constructs were designed, phages were amplified in bacterial hosts and then purified by polyethylene glycol-NaCl (PEG-NaCl) precipitation. Sec residues fused to g3p were subsequently biotinylated with 1mM iodoacetyl-PEO_2-biotin (Pierce) in 30mM acetate buffer (pH 5), yielding the final phage species, *B-*H_6.

2.5.1 Instrument design

Phage stretching was performed in an optical trap setup constructed around an inverted microscope (Nikon) as described previously [17]. Briefly, a high numerical aperture objective (100X, 1.40 NA, Nikon) tightly focuses a 1064 nm laser (Coherent) to form the optical trap. The trap location at the specimen plane was computer-controlled by a pair of orthogonally oriented acousto-optic deflectors (AODs, Intra-Action), and the positioning of the specimen was manipulated using a nanometer-resolution piezo-electric stage (Polytec PI). The combination of a 975 nm laser (Corning) and a position sensitive device (PSD, Pacific Silicon) was employed for back-focal plane position detection as collected from bead scattering [37]. Data was acquired with an A-D board (National Instruments) and custom software (LabView, National Instruments) was developed to automate experimental runs and data acquisition. Data analysis was performed using software written in MATLAB (Mathworks).

2.5.2 Single M13 stretching

A procedure for suspending M13 phages between surface and polystyrene microspheres was developed. 20 μg/mL Penta-His antibody (Qiagen) in TBS buffer (100 mM Tris-HCl, 150 mM NaCl, pH 7.5) was incubated in 10 μL flow cells, constructed from glass slides and etched coverslips. After washing flow cells with 200 μL of 3 mg/mL Casein (Sigma) in TBS, 40 μL of 10^8-10^9 *B*-H_6 phages/μL was flowed in and allowed to bind the antibody-coated coverslip surface for 25 min at room temperature. Following another washing step with 100 μL of 0.15 mg/mL Casein solution, 40 μL of 60 pM 440 nm streptavidin polystyrene microspheres (Spherotech) was exposed to immobilized phages for 20 min. Flow cells were finally washed with 200 μL of TBS.

Stretching candidates were located by visual inspection. Tethered bead were then optically trapped and put through a lateral centering routine. Next, the vertical height of the trap center was determined and fixed such that beads were offset 150-200 nm from the surface. Stretching was performed by repeatedly stepping the stage every 50 ms in increments of 10 nm while PSD voltage samples, acquired at 5 kHz, were averaged to obtain the bead position at each "fixed force" step. Beads from each stretching experiment were position calibrated using procedures described previously to map PSD voltage readings to spatial bead displacements [58]. Trap stiffness was determined from the positional variance of beads and from the Stokes drag method [106].

Output voltage, stage position, position calibration, and trap stiffness data were compiled to generate corresponding *F*-*x* measurements. Furthermore, the correct force and extension components were computed using the appropriate geometric corrections, as described previously [116].

2.5.3 DNA stretching

Preparation of DNA flow cells followed from the wealth of published protocols. Briefly, flow cell bottom surfaces were coated with 20 μM anti-digoxigenin polyclonal antibody (Roche Applied Science) for 45 min and subsequently washed with 200 μL of 3 mg/mL Casein in PBT (100 mM Phosphate buffer, 0.1 % Tween-20, pH 7.5). 20 pM 3500-bp dsDNA (Oligo

1: [Biotin]-5'-AAT CCG CTT TGC TTC TGA CT-3', Oligo 2: [Digoxigenin]-5'-TTG AAA TAC CGA CCG TGT GA-3'), which was PCR-amplified in TE buffer (10 mM Tris, 1 mM EDTA, pH 7.5), was incubated with 60 pM 440 nm streptavidin microspheres for 4 hours at 4°C and then exposed to the antibody-functionalized flow cells. Finally, the flow cells were washed with 400 μL of 0.15 mg/mL Casein. DNA stretching procedures were analogous to those of M13.

2.5.4 Imaging

Transmission electron microscopy (TEM) images were collected using a JEOL 2010, operating at 200 kV. Atomic force microscopy (AFM) images were carried out using a Nanoscope IV (Digital Instruments) operating in tapping mode under ambient conditions using etched silicon cantilever tips.

Chapter 3

Engineered Bacteriophages as Standalone Single-Molecule Handles: Phage Arms to Zinc Fingers

3.1 Summary

A general methodology for constructing force-based, single-molecule (SM) assays would make more biological systems accessible to study on the SM level. C_2H_2 zinc fingers, the most abundant DNA-binding domains of eukaryotic transcription factors, are models for understanding DNA recognition by proteins but have yet to be the focus of SM investigation. We simultaneously address both needs by engineering "zinc fingered-phages" – M13 filamentous bacteriophages with Zif268 zinc finger domains as capsid protein fusions – and featuring them in a prototypical SM assay. In particular, we employ zinc fingered-phage handles to grip and unfold a short DNA hairpin, obtaining the characteristic forces and extensions expected for the mechanical process. The phage-based system is advantageous genetically, as it relies on the wealth of established methods for directed phage display of proteins, and structurally, as it is built on a hierarchical, filamentous structure with desirable mechanical properties. Handles to zinc finger proteins unlock potential investigations into the underlying physics of protein-DNA interactions and a tool for building complex SM architectures. This method-

ology is also easily generalized for designing standalone linkers to other biomolecules. This chapter was reproduced from [50].

3.2 Introduction

Many fundamental biological processes are either driven by or are subject to molecular-scale forces. Indeed, force is a key parameter in the dynamic structure and function of single molecules. As a result, the study of biomolecules has been revolutionized by force-based, single-molecule (SM) techniques, such as optical tweezers, magnetic tweezers, and atomic force microscopy (AFM). For instance, in SM enzymology, force has been used to selectively perturb a mechanoenzyme's reaction coordinate in order to elucidate the fundamental mechanisms behind the enzyme's motion [107, 99, 113, 3, 65, 1]. Force has also been instrumental in the study of biomolecule structure and folding, by enabling measurement of an individual polymer's or protein's force-extension (F-x) behavior [104, 63, 121]. Finally, force has allowed the characterization of molecular bonds through force spectroscopy-related techniques [32, 43].

While these techniques become ever-comprehensive in the range of forces and displacements for which manipulation and measurement are possible, a common challenge to these SM studies is assay development. In particular, a general scheme for simply and reliably connecting the biomolecule of interest to the SM probe is lacking. In the simplest arrangement, the free end of the molecule is attached to the SM probe, while the other end is affixed to either a surface or a second probe. In AFM, for instance, a biomolecule is attached to a sample surface sitting atop a piezoelectric scanning stage. The surface is axially translated to contact a cantilever tip and then axially retracted to produce force-induced extension of the biomolecules being gripped by the tip. Challenges in specificity, however, such as nonspecific binding to the surface, can obscure AFM-based measurements of single molecules [79]. To mitigate such artifacts, tips and surfaces are sometimes functionalized with reactive molecules, ligands, or antibodies. This allows more control over geometry and directionality. However, the repertoire of mechanically strong interactions, such as streptavidin-biotin, can be small and limiting.

Another challenge in specificity is the unknown number of molecules attached to the relatively large probe. A remedy is to use long handles that connect the biomolecule to the probe and are able to transmit forces in specified directions. Tethering biomolecules is particularly helpful in the case of small, difficult to manipulate proteins. For instance, in order to mechanically unfold single proteins using optical tweezers, Cecconi *et al.* used double-stranded DNA (dsDNA) "handles" to tether *E. coli* protein ribonuclease H between two microspheres [20]. Here, and in many instances, researchers have resorted to engineering unique cysteine residues or even removing cysteine residues to make cysteine-light proteins for covalent attachment. This can potentially introduce unwanted perturbations to the protein's structure and function and often involves difficult chemistry procedures. Ultimately, we seek an alternative and simpler strategy for engineering "molecular handles" to biomolecules for SM manipulation.

M13 is a filamentous bacteriophage that is potentially well-suited for this task. M13 is widely known for its use in phage display techniques, whereby each phage particle displays biomolecules on coat proteins *and* carries the encoding DNA in its encapsulated viral genome. The proteinaceous capsid is composed of roughly 2700 copies of the *gene VIII* protein (g8p), arrayed in a helical-pitched cylinder, and capped with approximately five copies each of g3p and g6p at one end and five copies each of g7p and g9p at the other end. Packaged within the coat is single-stranded DNA (ssDNA), which is necessary for replication and production of progeny, and from which many cloning vectors have been created to yield functional display of peptides and proteins on all five M13 coat proteins [117]. Therefore, genetically, M13 is a promising platform for engineering standalone molecular handles because of the precedent for M13-based molecular biology and because of the relatively indiscriminate ability to modify each capsid protein.

Recently, we demonstrated that M13 can be engineered to tether individual microspheres and can elastically withstand substantial stretching forces imparted by optical tweezers [49]. Here, we report the further engineering of M13 into a standalone SM system: the capsid serving as both the filamentous handle *and* the scaffold carrying the protein of interest. The fusion protein we chose is a zinc finger protein: the DNA-binding domain of Zif268 [23], a mouse transcription factor (TF) that is homologous to human Egr1. There are many reasons

for this choice. First, Zif268 serves as a skeleton platform for achieving universal, sequence-specific DNA recognition. One of the founding members of the C_2H_2 family of zinc fingers, Zif268 has been crystallized [86] and has been the subject of many investigations seeking to map residue–nucleotide complementarity [91, 21, 22, 123, 30, 18]. From a scientific standpoint, these efforts are key to understanding gene regulation, while from an application standpoint, they are enabling powerful biotechnology platforms for drug discovery and gene therapy [90]. Second, transcriptional events within a cell are relatively infrequent as compared with, for instance, protein-protein interactions [39] and typically involve low copies of TFs [29]. Therefore, the SM assay is a close to 'natural,' *in vitro* way of probing the subtle, transient dynamics that would otherwise be obscured by population averaging inherent in ensemble measurements [64]. Finally, as we demonstrate herein, "zinc fingered-phages" could be harnessed as molecular building blocks for assembling higher-order, SM architectures. Specifically, we constructed zinc fingered-phages to grip and mechanically unfold short nucleic acid hairpins.

3.3 Results

3.3.1 Engineering Zinc Fingered-Phages

The M13 genome and abundant M13-based cloning vectors provide convenient platforms for displaying biomolecules on bacteriophage capsids. Phage display of combinatorial peptide libraries is one particularly useful manifestation of these platforms. In this work, we have taken advantage of these platforms to empower M13 into a standalone SM tool for facilitating linkages and force transduction to biological molecules of interest. In particular, we engineered M13 phages to display the zinc finger domains of Zif268 as fusions onto g3p capsid proteins: Zif268–M13 (Fig. 3-1). Display of zinc finger proteins on bacteriophage capsids has been achieved historically and primarily through phagemid engineering, in other words, using plasmids that are altogether separate from the M13 genome [91, 21, 22, 123]. Here, Zif268 zinc fingers were encoded into the full M13 genome, resulting in complete incorporation of fusion proteins on every phage particle. The M13 genome, which is commercially

available as the M13KE vector, is designed with restriction sites (Acc65I and EagI) at the N-terminal end of *gene III*. Therefore, to engineer a fusion to g3p, one need only obtain a recombinant gene of the protein of interest (i.e., Zif268) and apply basic molecular biology techniques (see *Materials and Methods*).

In addition to the Zif268–M13 clone, we also designed a mutant, Zif268–M13 (2F), that carries just the first two of three Zif268 zinc fingers (Fig. 3-1B). Transcription factors rely on tandem arrays of zinc fingers for specificity and affinity (cooperative behavior between sequential fingers is thought to be limited to a certain number of fingers [87]). In the 2F variant, we designed a mutant that would undoubtedly display reduced DNA-binding and serve as a "control" to validate the wild-type (WT) form, Zif268–M13. Additionally, engineering the variant reinforces the flexibility of the M13 system to mutagenesis and modified protein display.

In order to complete the standalone handle, we fused hexahistidine (H_6) tags to g9p capsid proteins at the filament's other end [49]. Both clones were readily propagated in the appropriate bacterial hosts (i.e., *Escherichia coli* cells containing the F-plasmid) and purified using standard phage preparation techniques (see *Materials and Methods*).

3.3.2 Zinc Fingered-Phages Display Cognate DNA Binding

The ability of our Zif268–M13 clones to bind DNA was qualitatively assessed with a standard Enzyme-Linked ImmunoSorbent Assay (ELISA). Briefly, short dsDNA, containing the consensus sequence (5'–GCG TGG GCG–3') and a biotin, were immobilized on neutravidin-coated 96-well plates. Serial dilutions of our Zif268–M13 clones, in parallel with WT M13 (herein we refer to the M13KE clone as WT), were allowed to bind the DNA and then linked to an enzyme that acts on a chromogenic substrate, giving optical absorbance readouts.

The equilibrium dissociation constant for Zif268 binding to its consensus sequence is $0.5 - 6.5$ nM, as reported by electrophoretic mobility shift assays [86, 91]. Therefore, we were confident we could resolve the strong binding interaction, even with a relatively low sensitivity technique, such as an ELISA. Indeed, the equilibrium binding results show clear and effective binding of the Zif268–M13 clone over WT M13 (Fig. 3-1D). Furthermore, as predicted, the 2F variant exhibited a decreased binding capacity (roughly 100-fold) with

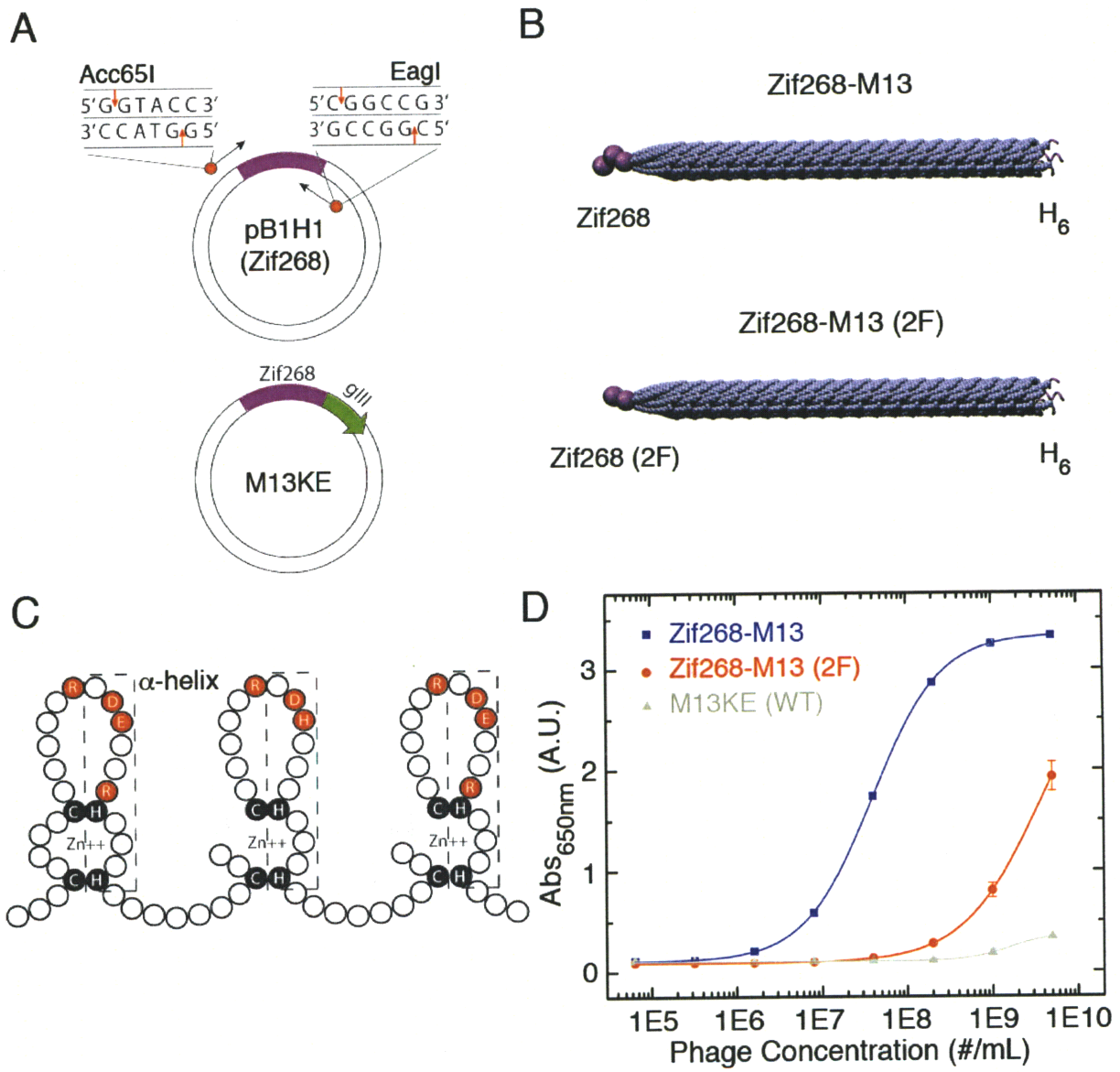

Figure 3-1: Engineering zinc fingered-phages. (A) Displaying Zif268 on M13 bacteriophage coat proteins is made simple by the commercially available and widely used M13KE cloning vector. (B) The three zinc finger domains of Zif268 were fused to g3p proteins, yielding "zinc fingered-phages" (Zif268–M13, above). In a mutant clone, only the first two finger domains were included (Zif268–M13 (2F), below). On the particle's remote tip, we displayed H_6 tags. (C) Cartoon representation of the simple and modular structure of C_2H_2 zinc finger domains. Each finger, which recognizes 3 consecutive bps, consists of a short, antiparallel β-sheet and an α-helix that are held compactly together by a cysteine- and histidine-coordinated zinc ion and a small hydrophobic core. Binding is achieved by docking of the α-helix into the major groove of dsDNA, which positions key residues in the helix (red circles) to contact 3 bases along one strand. (Cartoon adapted from [114]). (D) Equilibrium binding curves obtained from an ELISA study with the engineered zinc fingered-phages, showing variation in the DNA binding capacity of Zif268–M13 and the 2F mutant.

respect to Zif268–M13.

Avidity effects of multiple interactions, which are inherent to phage-displayed proteins, precludes us from extracting an equilibrium dissociation constant that can be reliably compared with previous reports. However, the resulting equilibrium binding curve is comparable to those obtained for phage-displayed streptavidin-binding peptides with nM affinity (C. Noren, personal communication).

3.3.3 Single DNA Hairpin Unfolding with Zinc Fingered-Phages

To demonstrate the phage handle in a SM context, we next designed an experimental procedure for unfolding short DNA hairpins with our zinc fingered-phages. The M13 filament is particularly well-suited for force-based measurements. In a previous study, stretching of single M13 particles revealed relatively stiff filaments, whose F-x behavior is well described by the wormlike chain (WLC) model [49]. A representative F-x curve and corresponding fit to the fluctuating rod limit of the WLC is shown in Fig. 3-2, where an elastic response is observed for loads through 80 pN.

Nucleic acid hairpins are model systems for understanding the fundamental problem of folding in biological structures. Furthermore, hairpins play essential roles *in vivo*. As a result, significant efforts have been made to map their folding landscapes [63, 82, 122, 121]. The application of force has been integral in these efforts, enabling the force-induced unfolding of hairpins and allowing researchers to tilt and constrain the molecule's reaction coordinate in highly controllable ways.

Woodside *et al.* recently underwent a systematic study of the sequence-dependent folding landscapes of 20 different DNA hairpins, for which they measured various kinetic and thermodynamic quantities, including the unfolding force and the opening distance [122]. This was achieved by tethering short hairpins ($6 - 30$-base pair (bp) stems) between two long, dsDNA handles that could then be attached to polystyrene beads, resulting in a "dumbell" geometry that is manipulated with two optical traps. We chose one of the studied hairpins, 20R25/T4 (20-bp stem length, quasi-random sequence, 25% GC content, thymidine tetraloop), and attempted to mechanically unfold it with zinc fingered-phage handles.

In our assay (Fig. 3-3), we essentially substituted the dsDNA handles with a Zif268–M13

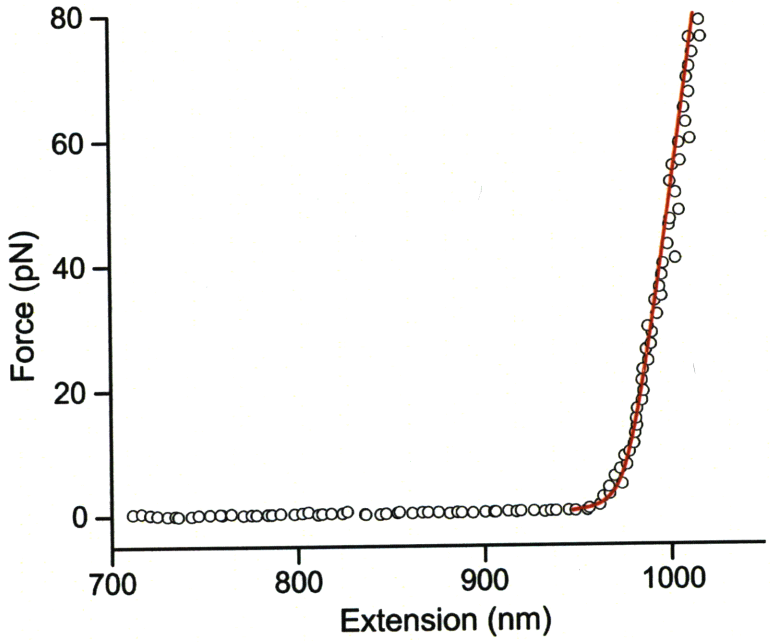

Figure 3-2: Single WT M13 bacteriophage stretching. Using previously developed methods [49], optical tweezers were used to stretch single WT filaments. The F-x response is captured well by the fluctuating rod limit of the WLC model (red line). M13 is an attractive candidate for use in SM, tethered bead assays because it exhibits a stiff, elastic response, even at high applied loads (80 pN).

handle. An advantageous feature of this system is that only 2 oligonucleotides are necessary to build the SM assay: one oligomer to make up the hairpin and a short, complementary oligomer to generate the double-stranded Zif268 cognate site. As a result, this experimental assay avoids the need to PCR-amplify many oligomers into a molecular handle of sufficient length and to subsequently ligate it to the hairpin ends. Rather, we simply attached one end of the DNA hairpin to polystyrene beads using the streptavidin-biotin interaction and relied on the native Zif268–DNA interaction to couple to the other end of the hairpin.

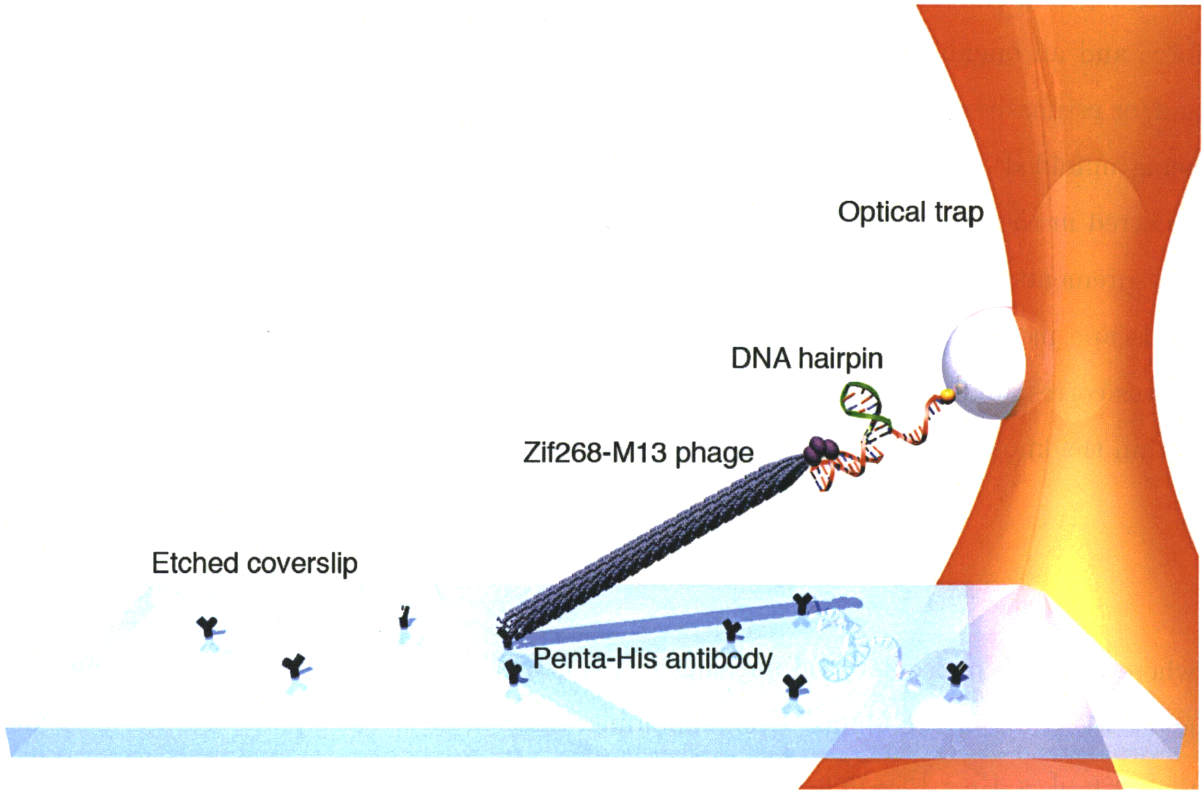

Figure 3-3: Illustration of DNA hairpin unfolding by zinc fingered-phages. The experimental geometry: a DNA hairpin is tethered between a bead, held in an optical trap, and a Zif268–M13 handle, which binds specifically to the 9-bp consensus sequence 5'–GCGTGGGCG–3' (not to scale).

We found that zinc fingered-phages do indeed facilitate the generation of SM tethers and subsequently used this result to measure the force-induced unfolding of hairpin 20R25/T4. After identification of tethered beads, hairpins were stretched using similar procedures to those of previous optical trap-based stretching measurements (see *Materials and Methods*). Briefly, tethered beads were trapped, centered and positioned in 3D, and then the specimen

plane was translated laterally at a velocity of 50 nm/s, while bead displacements from the trap center were recorded. As shown in Fig. 3-4A, at a critical force, the hairpin unfolds suddenly, leaving a sawtooth pattern in the time-dependent bead displacement or force trace [63]. In conjunction with the stage position, this data can be used to assemble molecular F-x curves (Fig. 3-4B).

The F-x curves provide the appropriate outputs by which to confirm proper hairpin unfolding and validate our system. Each unfolding event is characterized by an unfolding force and an opening distance, which can be readily compared to previous measurements and/or estimates of $F_{1/2}$ (defined as the force at which the hairpin has a 50% probability of being unfolded) and Δx for hairpin 20R25/T4. As shown in Fig. 3-4, unfolding typically occurred in the range of $\approx 9 - 13$ pN, which agrees well with the $F_{1/2}$ obtained from direct measurements of the open/close probability at constant F (10.6 pN) and from an energy landscape model (11.1 pN) [122]. To estimate the opening distance, we first fit the F-x curves corresponding to the folded structure with the appropriate form of the WLC model, within the known range of parameters for M13 [49]:

$$x = L_0 - \frac{k_B T}{2F}\left[L_0\sqrt{\frac{F}{A}}\coth\left(L_0\sqrt{\frac{F}{A}}\right) - 1\right] + \frac{FL_0}{K}, \tag{3.1}$$

where L_0 is the molecular contour length, $A = l_p\ k_B T$, l_p is the persistence length, and K is an elastic stretching modulus. Upon unfolding, the contour length is extended by an opening distance of $\approx 15 - 18.5$ nm, as estimated by subsequent fits of the unfolded curve. These estimates are also in good agreement with direct measurements of the hairpin extension at a constant F (17.6 nm) [122]. Finally, the overall contour lengths, observed in the F-x curves of Fig. 3-4B, both confirm the predicted values for M13 and reveal an added feature of this system – contour length can be tuned by the size of the virus-packaged plasmid. Specifically, the WT M13 capsid is assembled at the bacterial inner membrane around a $\approx$ 7222-nucleotide genome, yielding a contour length on the order of $900 - 1000$ nm. To express H_6 tags on capsid proteins of the remote tip, a 3950-nucleotide plasmid was inserted into bacterial hosts that were subsequently infected with helper phage (see *Materials and Methods*). As a result, zinc fingered-phages packaging the shorter plasmid are proportionally

shorter in length, $500 - 600$ nm (Fig 3-4B).

3.4 Discussion

SM methods have been widely adopted due to their ability to address a range of important biological questions, centered on the structure and function of biomolecules. For instance, SM stretching has revealed a more complete picture of the structure of DNA [104, 103], while studies of motion have detailed fundamental mechanisms of enzyme action [107, 99, 113, 3, 65, 1]. These results were largely unattainable by studies in the bulk because they required subtle temporal and distribution information. A limitation of these methods, however, is developing creative and trustworthy assays that link the biomolecule of interest with the ever-improving manipulation/detection instruments. Indeed, SM biophysics has flourished as a result of a small set of celebrated assays, such as the tethered bead, the kinesin bead assay, etc.

To this end, we have proposed a method based on M13 bacteriophage for constructing standalone, SM handles. This method is genetic in nature, in that it draws its power from the established techniques for genetically displaying biomolecules as fusions to capsid proteins. Additionally, the structure and mechanical properties of M13 are advantageous for force-based studies. M13 is filamentous, and, with a WT length near 1 μm, it provides ample spacing and geometric buffer against undesired force components. It is a semiflexible polymer, with a stiffer response to bending and stretching than dsDNA, and can accommodate forces beyond dsDNA's overstretching force (65 pN) [49].

As a demonstration of this method in its proposed SM context, the zinc finger domains of transcription factor Zif268 were, first, displayed on one end of the filament and shown to facilitate binding of the 9-bp consensus sequence (5'–GCGTGGGCG–3'). Next, a model hairpin, 20R25/T4, which has been previously characterized [122], was gripped with Zif268–M13 handles and unfolded in a optical tweezers-based assay. We observed typical binary-like hairpin unfolding, characteristic of a 2-state system. Unfolding forces and hairpin opening distances agreed well with previous measurements, and the F-x curves revealed contour lengths expected of WT and phagemid-packing M13.

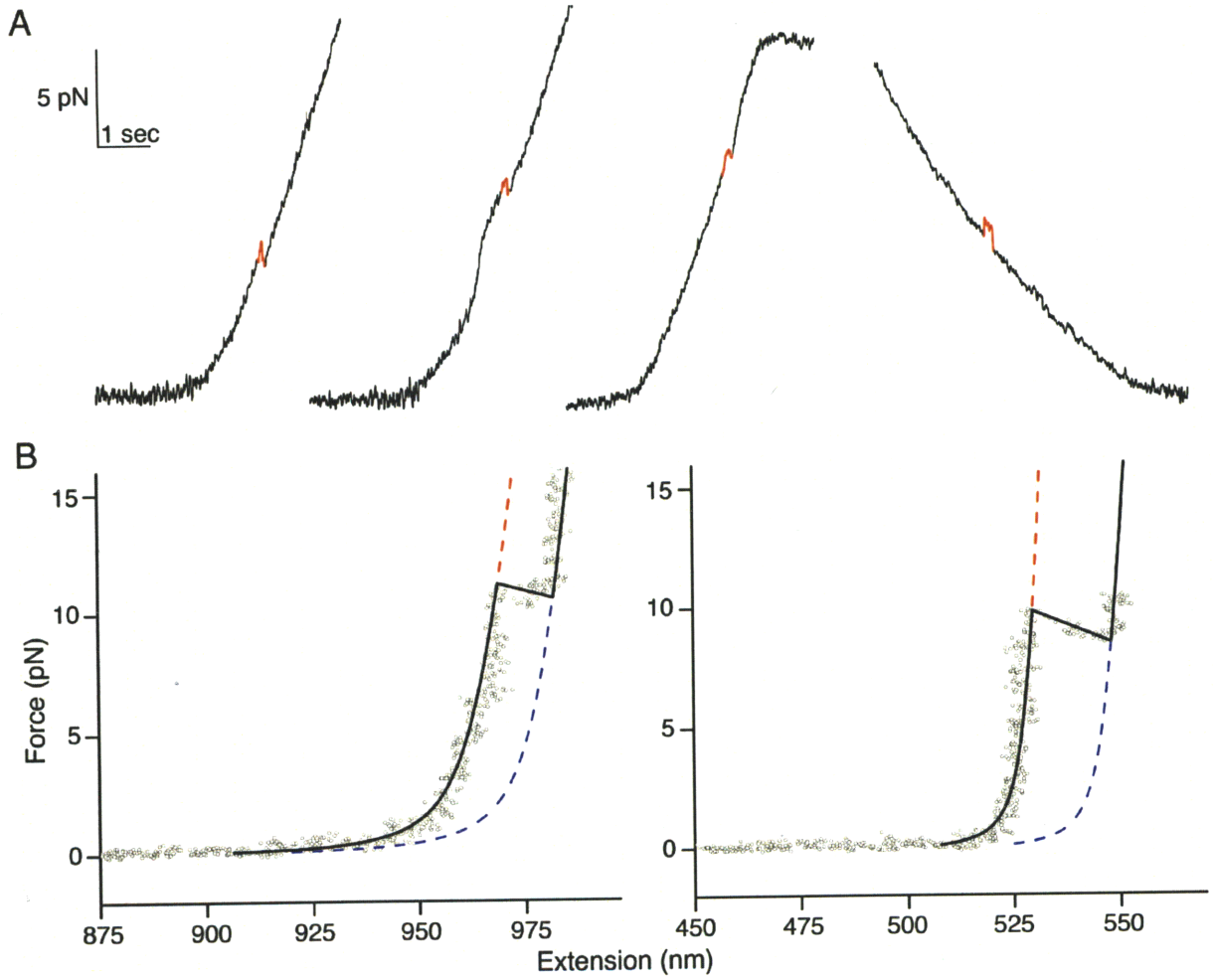

Figure 3-4: Measurement of DNA hairpin unfolding by zinc fingered-phages. (A) Representative stretching traces showing the discrete jumps that are characteristic of hairpin unfolding (first three traces) and refolding (final trace). (B) F-x curves for two unfolding measurements, overlayed with corresponding WLC fits (red and blue). In both cases, unfolding occurred near the hairpin's directly measured $F_{1/2}$ (11 pN) with opening distances near the directly measured Δx (17.6 nm). The Zif268–M13 handle length can be tuned by adjusting the size of the packaged plasmid: a WT M13 filament (left) and a phagemid-packaging filament (right).

The methodology described herein and the M13-based platform are meant as a general system for facilitating SM linkages and force transduction, with which other biomolecules can be substituted in. That said, Zif268 zinc fingers were specifically chosen for a variety of reasons that will continue to be topics of research. First, C_2H_2 zinc fingers, in addition to being the most abundant DNA-binding domains in eukaryotic transcription factors [46], are prototypes for understanding DNA recognition, and, as such, are platforms for *de novo* design of DNA-binding proteins. The crystal structure of Zif268 bound to its cognate subsite [86] was integral in assigning coordination between key residues in the zinc finger with complementary bases. Each zinc finger recognizes a DNA triplet (tandem zinc fingers recognize overlapping 4-bp subsites), with residues at positions -1, 3, and 6 of the helix making direct contact with 3 subsequent bases in one strand (primary strand) and the residue at position 2 making contact with a base in the complementary strand (Fig. 3-1C). Subsequent structural, biochemical, and combinatorial efforts have revealed recurring patterns and recognition 'rules' for the residues at these 4 positions [21, 22, 123, 30, 18]. However, the predictive power of these rules is limited and a simple, all-encompassing 'recognition code' is unavailable [46]. This is due, in part, to structural and binding complexities, including secondary interactions between residues and the phosphate backbone, the spatial relationship between the polypeptide backbone and DNA [85], complex residue-residue interactions [72], and strain imposed by the linkers connecting tandem zinc fingers [87]. Combining structural efforts with SM studies focused on the physics of protein-DNA interactions could contribute to the ongoing search for a universal 'recognition code.' In particular, our platform is well-suited for rapid modification of zinc fingers because the protein is encoded in the single-stranded M13KE template, which is ideal for classic Kunkel mutagenesis. Additionally, the zinc finger handle could be combined with established methods of SM DNA manipulation to provide insight into how DNA structure affects TF binding.

Second, as previously mentioned, transcriptional events *in vivo* are relatively infrequent [39] as a result of low-copy number. Therefore, SM studies are an appropriate *in vitro* testbed to probe TF dynamics [29]. Additionally, many families of eukaryotic TFs are characterized by transient binding events, with off-rates of $\approx 10^{-3} - 10^{-2}$ s^{-1} for their consensus sequences and even higher for nonconsensus sequences. This makes quantifying affinities

difficult with conventional and biochemical methods [64]. SM techniques, on the other hand, are specifically designed to capture transient behavior, such as that underlying the specific and nonspecific interactions that collectively lead to the dynamics of gene regulation.

Finally, standalone handles to sequence-specific, DNA binding partners provide immense potential for diversifying SM linkages. In this work, we employed the Zif268 consensus sequence to construct a handle to a DNA hairpin. This is, of course, just one of the many well-characterized binding sites of C_2H_2 zinc fingers. Potentially multiple different species of zinc fingered-phages could be utilized in concert to build more complex and previously unattainable SM architectures.

3.5 Materials and Methods

3.5.1 Engineering zinc fingered-phages

The zinc finger domains of Zif268 were fused to the N-terminus of each g3p capsid protein by direct M13KE genome cloning. The gene encoding for a recombinant form of Zif268 was PCR-amplified from the pB1H1 vector (Addgene) with primers possessing *Acc65I* and *EagI* restriction sites: (3F sense) 5'–CAT GCC CGG GTA CCT TTC TAT TCT CAC TCT GAA CGC CCA TAT GCT TGC CCT G–3'; (3F antisense) 5'–GGC GGC GCA TGT TTC GGC CGA GTC CTT CTG TCT TAA ATG GAT–3'; (2F sense) 5'–CAT GCC CGG GTA CCT TTC TAT TCT CAC TCT GAA CGC CCA TAT GCT TGC CCT G–3'; (2F antisense) 5'–CA TGT TTC GGC CGA TGT GTG GGT GCG GAT GTG GGT–3'. The PCR product and M13KE vector (New England Biolabs) were digested with *Acc65I* and *EagI* and subsequently ligated together, and the resulting plasmid was transformed into XL-1-Blue Electroporation-Competent Cells (Stratagene). After shaking the infected cells at 37°C for 1 hr., aliquots of the phage/cell mixture were diluted in melted top agarose and spread onto LB agar plates (containing 20 μg/mL tetracycline, 0.1 mM IPTG, and 40 μg/mL Xgal) for blue-white color screening. The plates were then incubated at 37°C for $12 - 16$ hrs. Resulting blue plaques were picked and used to inoculate ER2738 cells (New England Biolabs) in LB broth (containing 20 μg/mL tetracycline and 50 μM zinc

acetate), and the phage/cell mixture was subsequently grown at 37°C with shaking for $4-5$ hrs. Phages were purified by two-step polyethylene glycol-NaCl (PEG-NaCl) precipitation, sequenced to ensure proper incorporation of Zif268 genes, and finally resuspended in Zinc Buffer A (ZBA: 10 mM Tris, pH 7.5, 90 mM KCl, 1 mM $MgCl_2$, 50 μM zinc acetate, 0.5 mM EDTA). Hexahistidines were fused to g9p capsid proteins using previously described procedures, based on a pAK derived phagemid vector [49].

3.5.2 ELISA

Zif268–DNA binding was confirmed with a standard ELISA assay. Neutravidin (1 μg/well, Pierce) was adsorbed onto wells of a 96-well plate (NUNC MaxiSorp) at 4°C for $12-16$ hrs. After blocking with 5% bovine serum albumin (BSA) in TBS (100 mM Tris-HCl, pH 7.5, 150 mM NaCl), the wells were coated with short dsDNA fragments (Oligo 1: 5'–CCC TAT ATA **GCG TGG GCG** TAT ATA–3'; Oligo 2: [Biotin]–5'–CGG TAT ATA CGC CCA CGC TAT ATA GGG–3'). Next, serial dilutions (5-fold) of Zif268–M13 and WT M13 phage in Zinc Buffer B (ZBB: ZBA, 1% BSA) were incubated in the wells. The bound phages were coupled to HRP/Anti-M13 Monoclonal Conjugate (1:5000 in ZBB, GE Healthcare), which acts on the chromogenic substrate TMB (Sigma) to produce a color change that was quantified by reading absorbance values at 650 nm on a plate reader. All incubation steps following the adsorption of neutravidin were performed at room temperature for ≈ 2 hrs. on an orbital shaker. Wells were washed $3-5$ times with 0.1% Tween-supplemented buffer between every step.

3.5.3 DNA hairpin assay

A procedure for tethering short, DNA hairpins between Zif268–M13 handles and beads was developed. Hairpins were constructed by annealing two HPLC-purified DNA oligomers (Primary: [Biotin]–5'–CCC TAT ATA TTT AAG TTA ACA TCT AGA TTC TAT TTT TAG AAT CTA GAT GTT AAC TTT TTT ATA GCG TGG GCG TAT AGC GTG GGC GTA–3'; Secondary: 5'–TAC GGC CAC GCT ATA CGC CCA CGC TAT A–3', Integrated DNA technologies). Hairpin constructs were incubated with 800-nm diameter, streptavidin-

coated polystyrene beads ($\approx$ 12 pM, Spherotech) for 2 hrs. at 4°C in ZBC (Zinc Buffer C: 0.3 mg/mL casein in ZBA). $10 - 20$ μL flow channels, constructed from glass slides and KOH-etched coverslips, were coated with 20 μg/mL Penta-His antibody (Qiagen) for 1 hr. at room temperature. After blocking flow channels with 3 mg/mL casein (Sigma) for 30 min., Zif268–H_6 phage ($\approx 10^8/\mu$L in ZBA) was allowed to bind for 30 min. Unbound phages were washed away with 100 μL ZBC, and the DNA-loaded beads were introduced into the flow channel. Following a final 30 min. incubation, the flow channels were washed with 100 μL ZBC.

3.5.4 DNA hairpin unfolding

DNA hairpin unfolding (as well as phage stretching) was performed with a custom-built optical trap apparatus with nm-level spatial resolution [17, 49]. Beads tethered to the coverslip surface were located by visual inspection, optically trapped with a tightly-focused infrared laser (1064 nm Nd:YAG, Coherent), and subjected to an automated lateral centering routine. Next, the vertical height of the trap center was fixed so that beads were offset 200 nm from the coverslip surface. Stretching was performed by translating the specimen plane, via a piezo-electric stage (Polytec PI), at a constant velocity of 50 nm/s, while recording bead displacements from the trap center at 200 Hz (anti-alias filtered at a Nyquist frequency of 100 Hz). The combination of a 975 nm laser (Corning) and a position sensitive device (PSD, Pacific Silicon) was employed for back-focal plane position detection as collected from bead scattering [37]. Beads from each stretching experiment were position-calibrated [58] and stiffness-calibrated by the positional variance method [106], yielding trap stiffnesses of $0.2 - 0.3$ pN/nm. Data analysis was performed with custom software written in MATLAB (Mathworks).

Chapter 4

Kinesin Folds Forward

4.1 Summary

Each step of the kinesin motor involves a force-generating molecular rearrangement. While significant progress has been made in elucidating the broad features of the kinesin mechanochemical cycle, molecular details of the force generation mechanism remain a mystery. Recent molecular dynamics simulations have suggested a novel mechanism in which the forward drive is produced when the N-terminal *cover strand* forms a β-sheet with the neck linker to yield the *cover-neck bundle*. We tested this proposal by comparing optical trapping motility measurements of cover strand mutants with the wild-type. Motility data, as well as kinetic analyses, revealed impairment of the force-generating capacity accompanied by a greater load dependence in the mechanochemical cycle. In particular, a mutant with the cover strand deleted functioned only marginally, despite the fact that the cover strand, the N-terminal 'dangling end,' unlike the neck linker and nucleotide binding pocket, is not involved with any previously considered energy transduction pathway. Furthermore, a constant assisting load, likely in lieu of a power stroke, was shown to rescue forward motility in the cover strand deletion mutant. Our results support a stepping mechanism driven by dynamic cover-neck bundle formation. They also suggest a strategy to generate motors with altered mechanical characteristics by targeting the force-generating element. This chapter was reproduced from [48].

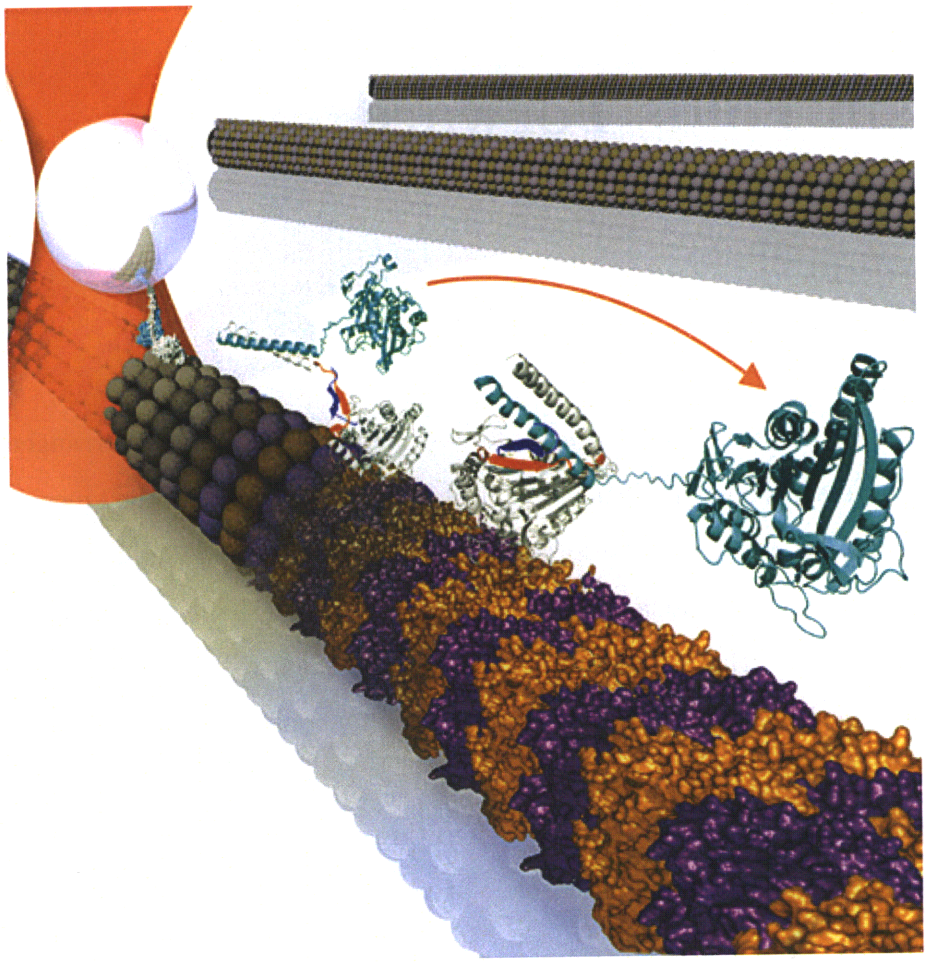

Figure 4-1: Kinesin folds forward (journal cover illustration).

4.2 Introduction

Translocating motors, such as kinesins and certain myosins, form a distinct class of proteins that "walk" along biofilament tracks to perform a wide range of vital cellular processes [110]. A fundamental, yet poorly understood aspect of these motors is the energy transduction mechanism that converts the chemical energy of ATP binding, hydrolysis, and product release into mechanical work. Kinesins and myosins appear to have a common nucleotide sensor [56, 111] yet have evolved different energy conversion mechanisms to achieve a variety of motile properties. In myosin, a series of structural changes leading to the rotation of its lever arm have been identified [36], but the details of the force generation have yet to be established.

Likewise, the force generation mechanism of kinesin (herein we mainly consider Kinesin-1) is not known. Until recently, the only mechanical element considered was the neck linker (NL), which connects the N-terminal motor head to the α-helical stalk. This $\sim$12-residue segment is disordered and flexible in the absence of ATP and "docks" when ATP binds to the motor head [93]. Mutations in the NL impair the motility whilst preserving ATPase activity and microtubule (MT) binding [19, 92]. However, a mechanism for its contribution to force generation is not available, and, in lieu of this, affinity-driven zippering of the NL to the motor head has been assumed. Unlike the structurally well-defined lever arm of myosin, the NL is short and flexible when detached. Furthermore, it interacts only weakly with the motor head [45], drawing further question to whether the NL alone is capable of generating the necessary forces to bias the forward motion of the trailing head.

To address the question of force generation in kinesin, we have recently carried out a series of molecular dynamics simulations and structural analyses, which suggest that an additional element is involved in the stepping mechanism. It is the motor head's N-terminal cover strand (CS) [45]. In a MT-bound, nucleotide-free leading head, the CS is separated from the rearward-pointing, "undocked" NL. In this state, the α4 helix (corresponding to myosin's relay helix) prevents α6 from forming an extra helical turn at the N-terminal base of the NL, which renders the NL out-of-register with the CS (Fig. 4-2A). When ATP binds to the motor head, conformational changes in the switch II cluster lead to retraction of α4

[52, 101], the subsequent formation of the $\alpha 6$ extra helical turn, followed by shortening of the NL. This places the CS and NL in-register to form a two-stranded β-sheet, which we refer to as the "cover-neck bundle" (CNB) (Fig. 4-2B). The CNB was shown by simulations to possess a forward conformational bias and generate forces consistent with previous 2-D force clamp motility measurements [13]. Specifically, a force map capturing the conformational bias of the CNB, generated through a new "tug-of-war" sampling method [44], was shown to be directed toward the motor head binding pocket and to be transversely anisotropic, helping to explain the asymmetric response of kinesin in 2-D force clamp experiments [13]. In contrast, the NL alone was shown to exhibit little forward bias and generate much smaller forces, in accord with the fact that its role as a force-generating element continues to be under debate [12]. The simulations thus suggested a force generation mechanism triggered by this dynamic disorder-to-order transition (*i.e.*, formation of the CNB from the NL and CS).

If CNB formation initiaties the kinesin power stroke, specific disruption of this local interaction should interfere with the ability of the molecule to exert force and move forward. To test this hypothesis, we designed two CS mutants, one that renders the CS more flexible by mutation of two residues to glycines, and the other one lacking the CS. Single-molecule motility measurements using an optical trap revealed that the CS mutants indeed generate less force compared to the wild-type (WT), and, as a result, display a variety of altered motile properties, such as processivity and load-dependent kinetic substeps. Taken together, our data suggest that the CS, which is separate from the conserved motor head core, is a key element in the force generation machinery of kinesin [93, 12]. Force generation by a disorder-to-order transition also suggests that static crystal structures may have to be supplemented with simulations to elucidate the dynamical features of motor proteins.

4.3 Results

4.3.1 Design of Cover Strand Mutants

For mutagenesis, we used *Drosophila* kinesin, for which there is a well-studied recombinant form [10] and which is highly homologous to the kinesins studied previously [45] (Fig. 4-3A–

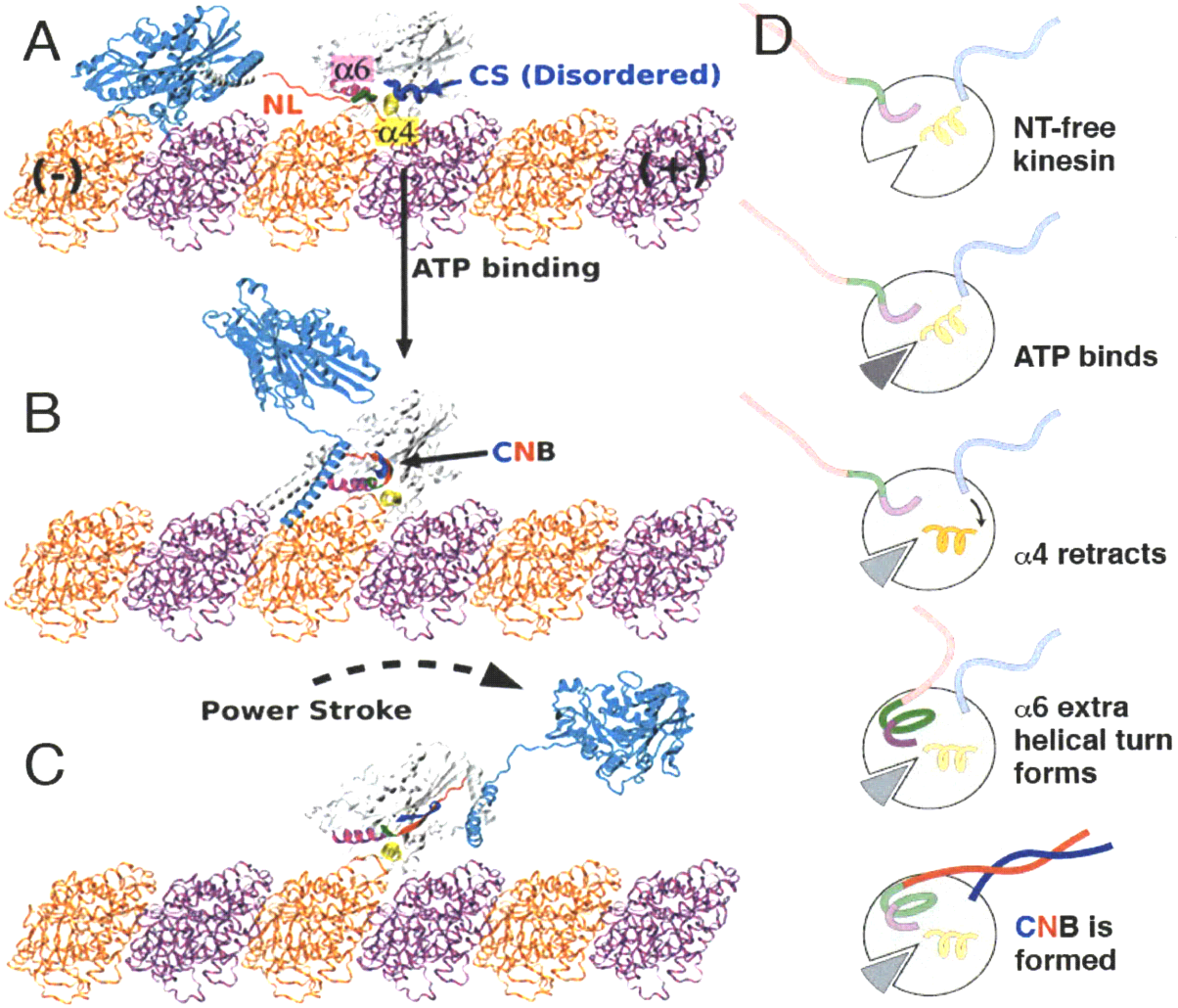

Figure 4-2: Model for kinesin's power stroke. (A) Prior to ATP binding, the NL (red) and N-terminal CS (blue, thick S-shaped tube) of the leading motor head are rendered out-of-register by the unwound portion (green, thick tube) of $\alpha 6$ (magenta). (B) ATP binding results in retraction of $\alpha 4$ (yellow), allowing the extra helical turn of $\alpha 6$ to form and bringing the NL and CS in favorable position to form a β-sheet, known as the CNB. (C) The CNB possesses the forward bias to deliver a power stroke and propel the trailing head forward. Following this action, the new leading head searches for its next MT binding site in a post-stroke confined space, while the C-terminal half of the NL latches onto the motor head, achieving its final, "docked" position. Kinesin dimers were constructed using PDB 1MKJ (with CNB) and PDB 1BG2 (without CNB). The neck coiled-coil stalk was extended based on PDB 3KIN. (D) Cartoon model highlighting the major molecular events that lead to CNB formation and a power stroke.

D). The CS of *Drosophila* kinesin is 13 residues long and a sequence comparison [45] indicated that CNB formation is achieved primarily through residues 9-13 (AEDSI), though a zipper-like interaction might also engage residues 1-8 into β-sheet formation [45]. Therefore, we generated a relatively conservative mutant 2G (A9G and S12G) and a second, more severe mutant DEL that lacks the entire CS (*i.e.*, residues 1-13 were deleted) (Figs. 4-3B,C).

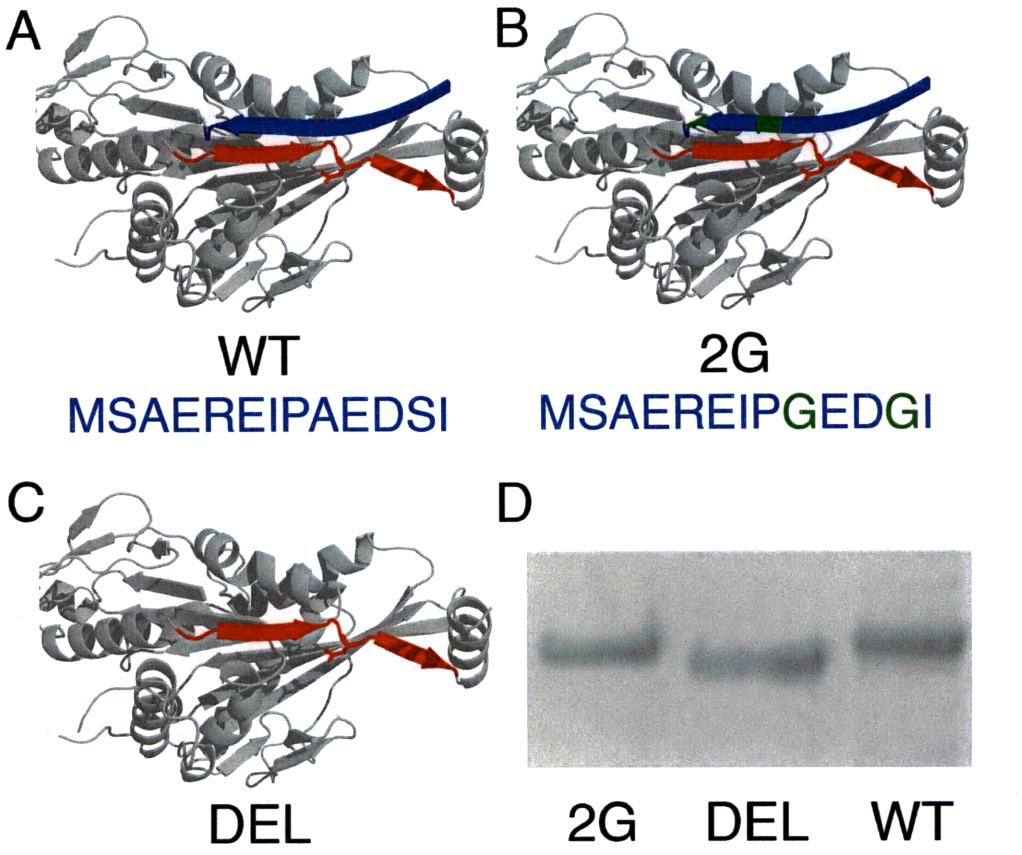

Figure 4-3: Kinesin mutant design. (A) WT: full CS (blue ribbon). (B) 2G: CS with mutated residues in green. (C) DEL: CS is absent. The NL is in red and the structure is based on PDB 2KIN, modified to incorporate the *Drosophila* CS (SwissProt ID P17210). (D) SDS-PAGE gel, confirming DEL's smaller molecular weight compared to WT and 2G.

4.3.2 Kinesin Motility With Load

We mechanically probed the force-generating capacities of both mutants, along with the WT, with classical single-molecule motility experiments using a custom-built optical trap apparatus with nm-level spatial resolution [49]. Motility was retained in all constructs. WT

walking records were normal, in that motors running at maximum velocity were slowed by the increasing optical force until near stall where the characteristic 8-nm steps are easily resolved (Fig. 4-4A). While Mutant 2G behaved qualitatively similar to WT, DEL motors were drastically crippled: relatively small backward loads ($0.5-2$ pN) caused motor stalling and stunted processivity, resulting from backward motions and/or slippage from MTs (Fig. 4-4B). Nonetheless, all three kinesins walked in stepwise fashion, as confirmed by the processive walking records measured at limiting ATP levels (4.2 μM ATP) (Fig. 4-5).

For a more quantitative comparison, we determined stall forces (F_s) and force-velocity (F–V) behaviors for the three motors. The mean stall force of Mutant 2G was 61% of WT, while that of the more drastic Mutant DEL was at most 27% of WT (Fig. 4-6A, Table 4.1). DEL motors repeatedly bound and released, sometimes taking no or only a few steps, before reaching the 0.7 pN force threshold, one of several stalling criteria [53] for detection of stalling events. This made it difficult to build the full stall force distribution for Mutant DEL. A running variance of bead displacement for 4 different DEL traces (Fig. 4-4B) showed that, of events in which the variance dropped 2 or 3 times below standard deviation (a characteristic drop in bead fluctuations accompanying MT binding), only $30\% - 60\%$ of DEL events surpassed the force threshold as compared with 100% of WT and 2G.

The effect on force production by CS mutation was also manifested in the F–V curves (Fig. 4-6B). A minimal kinetic model capturing the F–V relationship for many mechano-enzymes is the Boltzmann relation for the velocity, $v(F)$, as a function of the force, F, with a single load-dependent step [3, 115, 13]:

$$v(F) = \frac{v_{max}\,(1+A)}{1 + A\exp\left[\frac{F\delta}{k_B T}\right]} \tag{4.1}$$

where v_{max} is the unloaded velocity given by $v_{max} = \Delta/\left(\tau_1 + \tau_2\right)$, $\Delta = 8.2$ nm, τ_1 and τ_2 are the times associated with load-independent (biochemical) and load-dependent (mechanical) transitions at zero load, respectively, A is the ratio τ_2/τ_1, δ is the effective distance over which the force acts, k_B is Boltzmann's constant, and T is temperature. In fits using this model (Fig. 4-6B, solid lines), v_{max} was relatively unaltered, whereas both A and δ increased for the mutants (Table 4.1). Thus, an increase in A with load suggests that τ_2 increases,

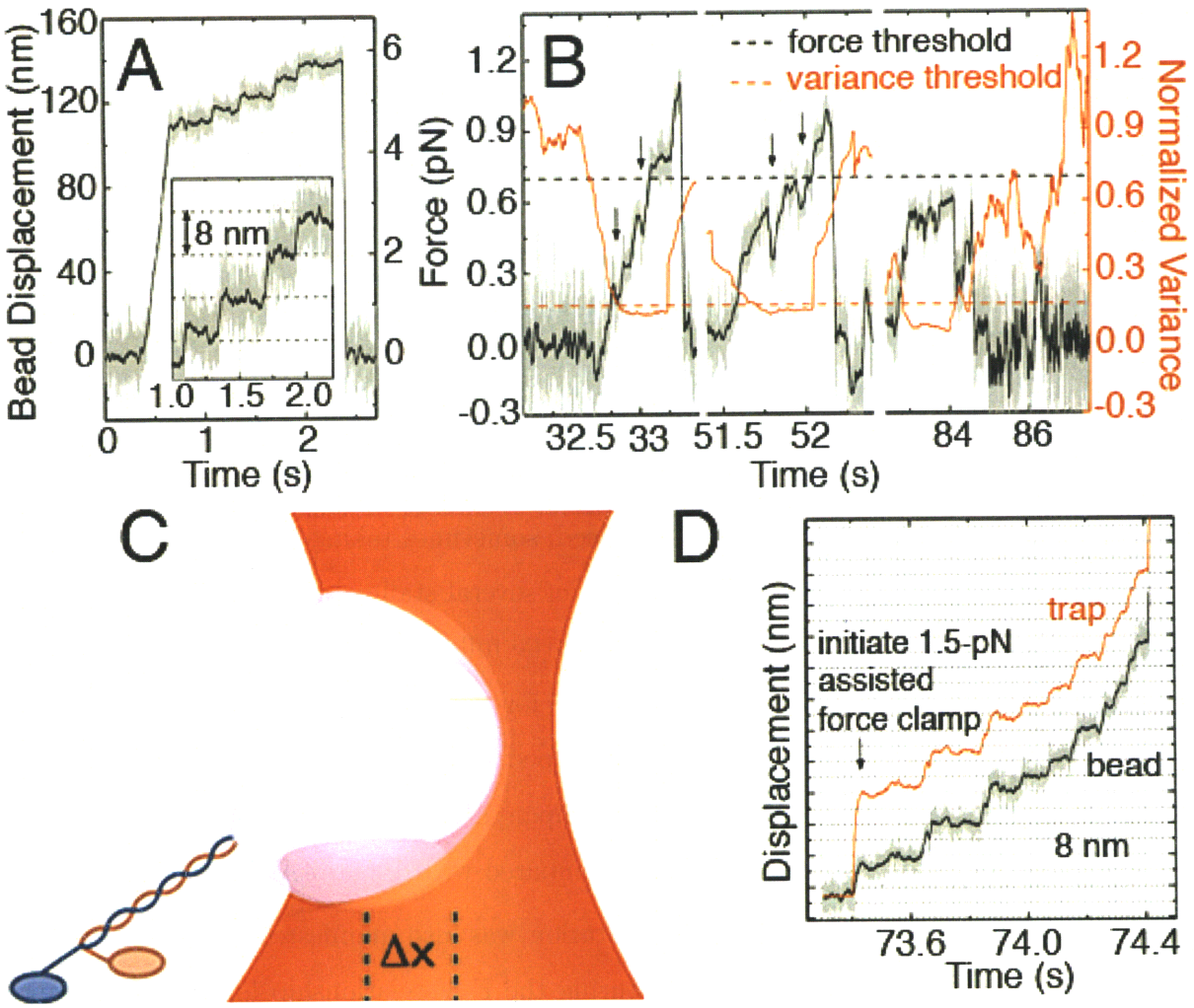

Figure 4-4: WT and DEL kinesin motility with load. (A) Representative stalling event for WT, which walks with 8-nm steps away from the trap center until stall ($F_s \sim 6$ pN). (B) Representative walking events for DEL, taken from a single trace, displaying the significantly impaired processivity and load-bearing capacity against low opposing forces. Events include many instances of backwards motion (arrows) and trajectories below the 0.7 pN force threshold (black dashed line) that is used for counting stalling events. For instance, in the rightmost event, the maximum force was only $\sim$ 0.6 pN, despite observing a drop in the running variance of the bead position (red trace) that is characteristic of MT binding and kinesin motility. The variance threshold (red dashed line) was 3 times below the standard deviation of the normalized variance. (C) Cartoon representation of kinesin subjected to a forward force clamp. (D) Representative walking event for DEL with a constant 1.5-pN, assisted load, which resulted in forward stepwise motion, typical of WT kinesins that possess the ability to produce a power stroke. The trap position (red trace) is maintained at a constant offset from the bead position (black trace) by an automated feedback control system.

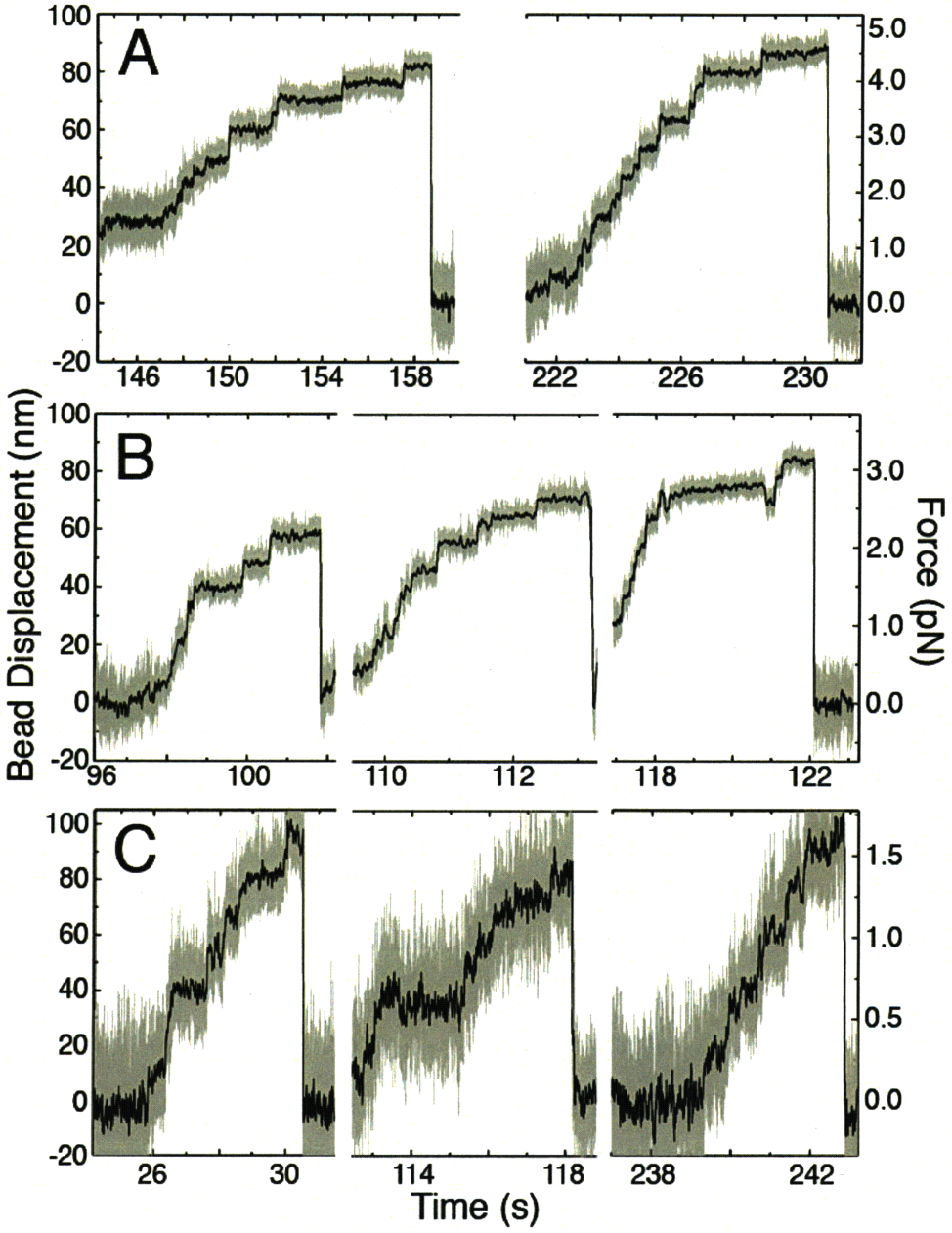

Figure 4-5: Processive walking events at limiting ATP levels (4.2 μM ATP). (A) WT. (B) 2G. (C) DEL.

i.e., the kinetics of the load-dependent mechanical transition is being affected by disrupting proper CNB formation. The increase of the "characteristic distance" δ from WT to 2G to DEL suggests that a larger fraction of the step distance is load-dependent. For WT, δ is smaller than the physical step size of 8.2 nm, as found previously [13], while for DEL, a larger value of δ indicates that the applied external load has a more significant influence over the molecule's mechanical step. In the absence of the CNB that generates a power stroke and holds the unbound head in the post-stroke leading position (Fig. 4-2C), thermal fluctuations may be the main driving force for the motor head motion.

It has been suggested that more than one load-dependent steps occur in the kinesin cycle [13]. Consequently, we also applied a model proposed by Fisher and Kolomeisky [35] that partitions the reaction coordinate into 2 states with spacings d_0 and d_1, such that $d_0+d_1 = 8.2$ nm (Fig. 4-6B). While the reaction coordinate was divided nearly equally for WT, it was skewed in 2G and more severely in DEL toward the second state (Table 4.1). Consistent with a division of the reaction coordinate into (a) a power stroke leading to (b) a diffusive search by the unbound, new leading head [12], the fit implies a larger contribution from (b). Although larger data sets, preferably involving force clamped measurements [13], would yield more adequate and detailed kinetic modeling, the simple models reveal the impaired motility characteristics of the mutants specifically designed to generate less force.

Stall force results were found to be consistent over a wide range of conditions, in that stall force histograms at 4.2 μM ATP overlayed predictably onto the respective histograms at saturating ATP and showed the same progression with CS mutations (Fig. 4-6A). Furthermore, the force dependence of the F–V curves on the CS mutations at limiting ATP levels shows a trend similar to the case of saturating ATP, suggesting that the load-dependence occurs mainly on or after ATP binding (Fig. 4-7).

With deletion of the CS nullifying the folding transition necessary for a power stroke, we hypothesized that external assisting loads would help to recover some of the forward bias of Mutant DEL and bring about normal, processive motion. We tested this in a preliminary experiment, in which we implemented an optical force clamp by feedback control of the trapping laser and subjected DEL motors to constant assisting forces at saturating ATP conditions. With the aid of a 1.5-pN forward load, walking records restored much of the

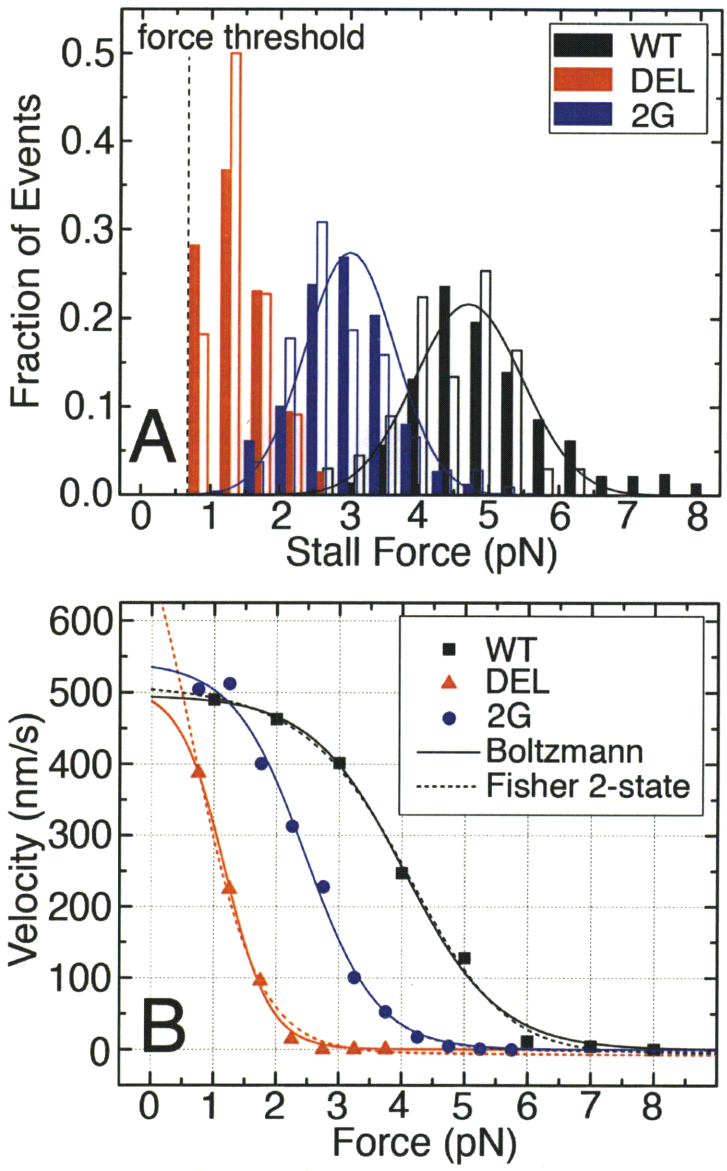

Figure 4-6: Measured mechanical characteristics of kinesin mutants. (A) Stall force histograms at 1 mM ATP (solid bars, saturating [ATP]) and 4.2 μM ATP (open bars, limiting [ATP]). Solid lines: Gaussian fits for WT and 2G at 1 mM ATP. DEL histogram was not fit because of the unknown number of stalls below the minimum detection force threshold (mean stall forces given in Table 4.1). (B) Global F–V curves generated from stalling event records at saturating [ATP]. Solid lines: Fits using the Boltzmann model (Eq. 4.1). Dotted: Fits using the Fisher-Kolomeisky 2-state kinetic model [35], which further support the biasing of the reaction coordinate toward a single state, likely by nullifying the power stroke (Table 4.1). For a complete list of parameter results, see Table 4.2.

character of WT kinesin, *i.e.*, forward processive motion in 8-nm steps (Fig. 4-4C). Although further force clamp experiments are necessary, the present results indicate that DEL lacks the forward bias generated by a power stroke, which can be compensated for by an external assisting force.

4.3.3 Kinesin Motility Without Load

The unloaded velocity, $v(0)$, and processive run length, L, of Mutant 2G were at least those of WT (Table 4.1), suggesting that its ATPase machinery was unaffected by mutation of the CS, which is structurally separate from the highly conserved catalytic core. Interestingly, we observed slightly enhanced unloaded velocity and run length for 2G. Even though the faster unloaded velocity was not statistically significant, this enhancement was similarly observed and even more pronounced in initial velocities at 4.2 μM ATP (Fig. 4-7). Presumably, this is due to the increased flexibility of its CS, which may reduce the time for CNB formation. In 2G, the decreased time associated with load-independent transitions (τ_1) may offset the increase in time for load-dependent transitions (τ_2; due to the diminished force generation), ultimately resulting in a slightly higher v_{max}. Furthermore, a more flexible CS may allow the molecule to enter its power stroke more quickly, thus reducing the time in a single-headed bound state and increasing processivity. In a sense, 2G can be regarded as being in a 'high-gear' state, in which it can generate less force but is kinetically more efficient.

By contrast, DEL had severely lower processivity (4-fold reduction), as foreshadowed by the abundant releasing and backwards events observed under load, and, as a result, it was difficult to estimate unloaded velocity (Table 4.1). Compared to the extrapolated value from F–V curves (487.4 nm/s, Fig. 4-6B), the unloaded velocity by direct bead tracking (254.8 nm/s) was significantly lower, in contrast to WT or 2G, whose velocities from the two measurements were comparable. Also note that with a 1.5-pN constant assisting force, where we have increased position resolution, DEL appears to step similarly to WT. The nonzero unloaded velocity of DEL, although ill-defined due to short run lengths, may correspond to a pure thermal diffusion with trapping by binding to the MT. During its mechanochemical cycle, when both heads are bound to the MT, ATP binding to the leading head would still be limited by strain on its rearward-pointing NL [95]. Alternatively, ADP release from

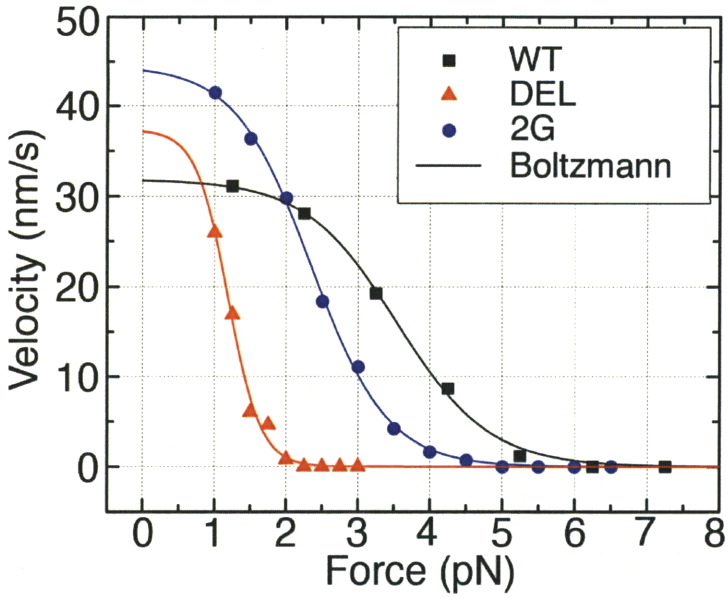

Figure 4-7: F–V curves generated from stalling event records at limiting ATP levels (4.2 μM ATP). Solid lines: Fits using the Boltzmann model.

the trailing head may be suppressed by the forward-pointing conformation of the NL [75]. One or both of these effects could contribute to maintaining the motor head coordination and forward directionality of DEL, although the reduced pulling force from the leading head weakens the strain-induced regulation and makes detachment of the trailing head more difficult. Furthermore, when the trailing head detaches, there is no active machinery to bring it forward (Fig. 4-2B→C), and its search for the next MT binding site will be largely driven by thermal fluctuations. As this is expected to be much slower than the forward motion of the unbound head via a power stroke, the MT-bound head may undergo ATP hydrolysis and detach before the unbound head finishes its diffusive search, resulting in a short run length. Thus, mutations in 2G and DEL have opposite effects on processivity.

Table 4.1: Summary of motility and load-dependent kinetic parameters measured at saturating [ATP].

	Load						No Load	
		Boltzmann			Fisher 2-state			
Kinesin	Stall Force* F_s (pN)	$v_{max}^{\dagger}$ (nm/s)	$A^{\dagger}$	$\delta^{\dagger}$ (nm)	d_0 (nm)	d_1 (nm)	$v(0)^*$ (nm/s)	L^* (μm)
WT	4.96 ± 0.05	493.7 ± 26.4	0.0043 ± 0.0050	5.53 ± 1.04	4.4	3.8	581.1 ± 38.8	1.104 ± 0.215
2G	3.02 ± 0.03	535.2 ± 27.8	0.0137 ± 0.0101	7.15 ± 1.10	1.1	7.1	608.2 ± 22.5	1.740 ± 0.209
DEL	$1.37 \pm 0.04^{\ddagger}$	482.1 ± 33.5	0.0357 ± 0.0202	11.28 ± 1.24	0.4	7.8	254.8 ± 27.2	0.342 ± 0.088

ber of measurements: $n_{\text{loaded}} = 373, 487, 117$; $n_{\text{unloaded}} = 34, 75, 32$ (WT, 2G, DEL).

n $\pm$ s.e.m.; †mean $\pm$ 95% confidence interval.

ntially biased toward a higher mean value on account of the unknown number of stalling events below the minim

tion threshold of 0.7 pN.

4.4 Discussion

The cover-neck bundle (CNB) action proposed for kinesin involves force generation by the *folding* of a domain (*i.e.*, a disorder-to-order transition), rather than by conformational changes of well-defined domains. This new, dynamic energy transduction pathway was identified by simulations based on the available structures [45]. To test the model, mutants of the CS, which forms the CNB with the NL, were generated and shown to be deficient in their force generation capacities. The altered kinetics of CNB formation in the 2G mutant led to increased processivity, while deletion of the CS resulted in motility that was stunted and likely driven in large part by thermal fluctuations without a power stroke. In the latter, processive forward motility was rescued by applying a small assisting load.

The force generation mechanism by CNB formation explains why changes in the NL, despite being clearly associated with kinesin's stepping motion [93, 109], alone do not appear sufficient to generate force [92, 12]. A previous study suggests that NL docking is weakly favorable, with only a 3 kJ/mol free energy loss associated with the event [92]. However, this measurement was made on unloaded kinesin monomers, for which the undocked NL would assume a relaxed, likely forward-pointing conformation. On the other hand, when a kinesin dimer walks on a MT, the power stroke in the leading head begins from a rearward-pointing NL state and proceeds against load. Since the conformational ensemble of the undocked NL is different, the 3 kJ/mol free energy of NL docking may not be applicable to the case of a dimer under load. Furthermore, the electron paramagnetic resonance (EPR) measurement compares ADP to AMP-PNP states, as a proxy for the transition between nucleotide-free and AMP-PNP states. Since the NL may exist in an ADP state that is partially bound (see Fig. 4d in [93]), the EPR measurements may include transitions between weak and strong NL bound states. Furthermore, without load, CNB formation is simply a short β-sheet folding process. In analogy with β-hairpin formation, the associated free energy change is expected to be low [45], consistent with the result of [92]. Yet the CNB picture permits the possibility of a larger free energy change when loads are applied. For a clearer picture of how force is generated, a more detailed study on thermodynamics of CNB formation under load is necessary.

When the NL docks to the motor head from the rearward-pointing state, its end translates by approximately 7.5 nm along the MT axis. Of the motion over this distance, about 5.1 nm is caused by the power stroke carried out by the $\beta 9$ half of the NL, while a latch mechanism in its C-terminal half is thought to carry out the rest of the docking event [45]. Since the NL of the stepping motor head makes a reverse transition from a forward- to rearward-pointing state, the distance covered by the NL motion in both heads (7.5 nm $\times$ 2) is close to the total 16 nm distance of travel by the stepping head. The small gain in axial distance caused by the $< 20^\circ$ motor head rotation upon ATP binding [51] may cover the remaining distance during a stepping event. However, rotation of the motor head upon ATP binding is not likely to affect the proposed force generation mechanism. A recent cryo-EM study showed that the conformation of the nucleotide-free motor head bound to the MT virtually mirrors the x-ray structure of an isolated head, except for the nucleotide switch region [102]. Upon ATP binding, the head rotates so that the NL binding pocket moves further away from the MT, hence there is no obvious rearrangement induced by interaction with the MT that might enable a zipper-like binding of $\beta 9$ without assistance of the CS. While the two-part mechanism of power stroke followed by latching [45] explains the NL docking action in the MT-bound head, it is yet unclear how the forward- to backward-pointing transition of the NL in the moving head occurs.

A sequence comparison shows that the CNB-forming part of the CS is conserved among Kinesin-1, 3, and 5 [45]. The minus-end-directed, C-terminal ncd motor also possesses a 36-residue N-terminal cover domain, which is invisible (hence flexible) in available crystal structures [31]. As in Kinesin-1, the cover domain is in close proximity to the N-terminal neck of ncd, which suggests that a dynamic interaction between the cover and the neck domains could be a common feature across many kinesin families. More generally, about half of single-domain proteins in the Protein Data Bank have contacting N- and C-terminal elements [55]. Furthermore, it has been recently suggested that proteins with N- and C-termini forming a β-sheet domain may possess a 'chameleon' behavior in which the terminal segments switch between different secondary structures to assist with proper folding [74]. The disorder-to-order transition of the CS and the NL would be an adaptation of this type of behavior to force generation in kinesin motor domains. Identifying and characterizing the

force-generation elements of motors other than kinesin would aid in understanding how they function.

4.5 Materials and Methods

4.5.1 Plasmid preparation

Kinesin mutants were designed from an existing expression plasmid for a recombinant truncated derivative of kinesin, which includes the N-terminal 401 amino acids of *Drosophila melanogaster* kinesin heavy chain (DmK401), followed by a biotin carboxyl carrier protein (BCCP) and a His_6 tag (gift of J. Gelles, Brandeis University) [10]. To create the 2G mutant, we mutated the gene sequences for residues 9 and 12 using the QuickChange Multi Site-Directed Mutagenesis Kit (Stratagene) with a single oligonucleotide primer containing the desired mutations (5' - CGAGAGATTCCCGGCGAGGACGGCATCAAAGTGG - 3'). We created the DEL mutant by cassette mutagenesis of the original expression plasmid, specifically by taking advantage of the unique restriction sites flanking residues 1-13 (*XbaI* and *NgoM IV*). First, we constructed a 133-bp mutant gene insert, possessing the 2 restriction sites, from 6 overlapping oligonucleotide primers: (a) 5' - CCACAACGGTTTCCCTCTAGAAATAATTTTG - 3'; (b) 5' - CTCCTTCTTAAAGTTAAACAAAATTATTTCTAGAGG - 3'; (c) 5' - CTTTAAGAAGGAGATATACATATGATCAAAGTGGTCTGCCG - 3'; (d) 5' - CTGTCGTTCAGCGGTCGGAATCGGCAGACCACTTTG - 3'; (e) 5' - CGCTGAACGACAGCGAAGAGAAGGCCGGCTCC - 3'; (f) 5' - ACTTGACCACGAACTTGGAGCCGGCCTTC - 3'. The original plasmid and the mutant gene insert were digested with *XbaI* and *NgoM IV* and subsequently ligated together, and the resulting plasmid was transformed into One Shot TOP10 Chemically Competent Cells (Invitrogen). The final expression plasmids carrying the WT, 2G, and DEL genes were confirmed by sequencing of the entire protein reading frames.

4.5.2 Protein preparation

BL21(DE3)pLysS *E. coli* cells (Invitrogen) were transformed with the 3 plasmids to create expression strains. Protein expression and purification followed from previously described methods [9, 4]. Briefly, mid-log cultures in TB medium, supplemented with 24 mg/L biotin, were induced with 1 mM isopropyl-β-D-thiogalactopyranoside (IPTG) and subsequently brought from 37°C to room temperature. After 3 h, 0.2 mM rifampicin was added, and the cultures were grown overnight. Harvested cell pellets were resuspended in lysis buffer (20 mM imidazole, pH 7, 4 mM $MgCl_2$, 2 mM PMSF, 2 μg/mL pepstatin A, 20 μg/mL TPCK, 20 μg/mL TAME, 2 μg/mL leupeptin, 20 μg/mL soybean trypsin inhibitor, 10 mM β-mercaptoethanol) and lysed via 3 freeze-thaw cycles. The lysates were incubated with 1 mg/mL RNAse A (Sigma, Type II-A) and 0.5 mg/mL DNAse I (Sigma, Grade II) for 30 min at 4°C and then clarified by centrifugation (21,800 g, 20 min, 4°C) followed by ultracentrifugation (180,000 g, 30 min, 4°C). The clarified lysate was purified using liquid chromatography by binding to Ni-NTA resin (Qiagen, Ni-NTA Superflow) and eluting with 70 – 100 mM imidazole. The collected fractions were pooled, concentrated in a Vivaspin 15 spin column (Vivascience, 30,000 MWCO), and stored at -80°C in storage buffer (50 mM imidazole, pH 7, 100 mM $NaCl_2$, 1 mM $MgCl_2$, 20 μM ATP, 0.1 mM EDTA, 5% sucrose).

Extensive characterization of the protein products was carried out. Kinesin proteins were well-expressed (final concentrations typically exceeded 1 mg/mL), pure (according to SDS-PAGE gels), and healthy (large dilutions of $>$ 300,000 fold were required to drive motility assays to the single-molecule limit). Finally, to ensure that proper protein translation had taken place, the protein sequences of the 3 kinesins were confirmed by standard Edman degradation N-terminal sequencing with 2 separate automated systems: Procise and ABI 494 Protein Sequencers (Applied Biosystems).

4.5.3 Single-molecule motility assay

Dilutions of kinesin corresponding to the single-molecule limit were incubated with 0.44-μm diameter streptavidin-coated polystyrene microspheres (Spherotech Inc.) for 1 hr at 4°C in assay buffer (80 mM Pipes, pH 6.9, 4 mM $MgCl_2$, 50 mM potassium acetate, 1 mM

EGTA, 0.1 mM DTT, 20 μM Taxol. 1 mg/mL casein, 1 mM ATP) to allow binding. MTs, polymerized from tubulin (Cytoskeleton), were diluted and stabilized in PemTax buffer (80 mM Pipes, pH 6.9, 4 mM $MgCl_2$, 1 mM EGTA, 20 μM Taxol) and then immobilized on poly-L-lysine-coated etched coverslips. After a series of washes with PemTax and assay buffers, kinesin-loaded beads were introduced to the 10 μL flow cells.

4.5.4 Motility measurements with load

Freely diffusing beads carrying kinesin motors were optically trapped with an infrared laser and positioned atop fixed MT filaments. Displacements from the trap center of motile beads were recorded at 2 kHz, anti-alias filtered at a Nyquist frequency of 1 kHz, as kinesin motors processively walked against the increasing optical force until stall. Beads from each motility record were position-calibrated [58] and stiffness-calibrated by the positional variance method [106]. Trap stiffness ranges were 0.040 – 0.060 pN/nm, 0.025 – 0.045 pN/nm, and 0.010 – 0.025 pN/nm for WT, 2G, and DEL, respectively.

Data analysis was performed with custom software written in MATLAB (Mathworks). Raw motility records were transformed to displacement and force transients, filtered with a boxcar window of 25 ms, and parsed into stalling events that met stalling criteria [53]: stall force $>$ 0.7 pN, stall plateau time $>$ 0.1 sec, stall velocity $<$ 50 nm/sec, snapback velocity $>$ 500 nm/sec, and a snapback to baseline. Stall forces were extracted from each stalling event and compiled into histograms. Force-velocity (F–V) curves for each stalling event were constructed by dividing motility data into 15-ms (1 mM ATP records) and 175-ms (4.2 μM ATP records) windows, in which the force trace was averaged and the velocity was obtained from linear fits to the corresponding bead displacement trajectory. Curves from each motility record (*i.e.*, per kinesin molecule) were pooled into global F–V curves by averaging into 1-pN force bins for WT and 0.5-pN force bins for mutants.

Motility measurements were found to be reproducible. A second preparation of Mutant 2G, for instance, yielded $<$ 6% deviation in mean stall force: 3.09 ± 0.04 pN (mean $\pm$ s.e.m., $n = 286$) vs. 2.92 ± 0.05 pN ($n = 201$).

4.5.5 2-state kinetic model

A full description of this kinetic model has been provided previously [35]. According to multistate chemical kinetics, molecular motors pass through a sequence of N intermediate biochemical states for each physical step taken. The F–V curves of kinesin can be described with a 2-state model [34, 35]. Briefly, for a step distance of $d = 8.2$ nm between consecutive binding sites $x = ld$ ($l = 0, \pm 1, \pm 2, \ldots$) on a linear MT track, the 2 intermediate biochemical states are connected by forward rates, u_j, and backward rates, w_j:

$$(0)_l \underset{w_1}{\overset{u_0}{\rightleftharpoons}} (1)_l \underset{w_0}{\overset{u_1}{\rightleftharpoons}} (0)_{l+1} \tag{4.2}$$

where the corresponding substep lengths, d_j, sum to the total step length, $d = d_0 + d_1$. An external load biases the rates by Boltzmann factors, such that $u_j \rightarrow u_j(F) = u_j^0 \exp\left[-\theta_j^+ Fd/k_BT\right]$ and $w_j \rightarrow w_j(F) = w_j^0 \exp\left[+\theta_j^- Fd/k_BT\right]$, where $\theta_j^{+/-}$ are the load distribution factors that divide the reaction coordinate into the substeps, $d_j = (\theta_j^+ + \theta_{j+1}^-)d$. The resulting expression for the mean velocity, V, is

$$V = d(u_0u_1 - w_0w_1)/(u_0 + u_1 + w_0 + w_1) \tag{4.3}$$

which can be used to model F–V data from single-molecule motility measurements. Using previously extracted model parameters [35] as initial guesses, our F–V curves were well described by the model (Table 4.2), where $u_0^0 = k_0^0[\mathrm{ATP}]$ for ATP binding in the first forward transition and $w_0^0 = k_0'[\mathrm{ATP}]/(1 + [\mathrm{ATP}]/c_0)^{1/2}$ in the final reverse reaction, as defined previously [35].

4.5.6 Optical force clamp

An optical force clamp was implemented following previously described methods [58]. A constant force was applied to kinesin-loaded, motile beads by maintaining the center of the trapping beam at a constant, specified displacement. Custom software written in Labview 6.1 (National Instruments) was used to control the trap position via acousto-optic deflectors (IntraAction). First, freely diffusing beads were trapped and position- and stiffness-calibrated.

Table 4.2: Summary of 2-state kinetic model parameters.

	WT	2G	DEL
k_0' (μM^{-1}sec^{-1})	6.327	0.363	0.104
k_0^0 (μM^{-1}sec^{-1})	3.625×10^{-3}	3.714×10^{-2}	2.244×10^{-2}
c_0 (μM)	9.71	28.82	148.6
w_1^0 (sec^{-1})	0.650	0.03869	7.97
u_1^0 (sec^{-1})	62.07	81.01	460.2
θ_0^+	0.547	$\sim$0	0.035
θ_0^-	0.451	0.869	$\sim$0
θ_1^+	0.002	$\sim$0	0.960
θ_1^-	$\sim$0	0.131	0.015

Beads were then steered atop MTs, and the trap center was placed at the edge of the detection zone. Bead position data was sampled at 5 kHz, anti-alias filtered at 2 kHz, and the trap position was updated at 500 Hz to maintain a constant displacement from the bead center. The force clamp feedback was triggered manually, based on visual inspection of the drop in bead positional variance accompanying motility, and stopped when beads reached the outer edge of the detection zone.

4.5.7 Motility measurements without load

Single kinesin molecules were attached to 0.8-μm streptavidin-coated beads (Spherotech Inc.). The optical trap was operated at < 0.05 pN/nm. The KG filter (CVI Laser, CG-KG-5-1.00-3) before the CCD camera (Dage-MTI, CCD-100) was partially removed so that the laser was visible on the camera. An unloaded velocity event was captured by trapping a bead, starting video recording at 30 frames per sec, positioning the bead above a MT, releasing the trap at first sign of motility, and continuing recording until the bead detached from the MT and diffused away. Movies were clipped to start at the first frame after shutting the trap off and to end with the last frame where the bead was attached to the MT. Bead position was calculated using a centroid method to map out the traveled paths. A second order polynomial was fit to the paths to quantify run lengths. Due to the speed of video capture and operator speed, short run events were difficult to capture, as was typically the case for DEL.

Appendix A

Semiflexible Polymers

The mechanics of semiflexible biopolymers are critical to the structure and function of cells, accounting for such phenomena as the compact packaging of DNA into chromosomes and the scaffolding of cells by actin networks. Whereas we have a fairly complete understanding of highly flexible chain molecules, the field of semiflexible polymers continues to challenge and flourish, particularly since the development of experimental tools for visualizing and manipulating single filaments. As a result, there has been an explosion of data with which to test and improve theoretical models. This appendix is intended to provide an introduction to the theoretical framework for semiflexible polymer modeling.

A.1 The Bent Rod

An understanding of semiflexible polymers begins with a classical mechanics treatment of beam bending. Consider a slender rod with length much greater than diameter, as depicted in Fig. A-1. In the bent geometry, the upper portion of the rod undergoes stretching while the lower portion undergoes compression. These regions meet at a a *neutral surface* whose length remains fixed. From simple geometry, the stretched (or compressed) amount, as a function of the distance to the neutral surface y, is

$$\frac{dl}{l} = \sin\theta = \frac{y}{R} \tag{A.1}$$

We can then invoke *Hooke's law* to determine the force per unit area in an infinitesimal strip, dy, to obtain

$$\frac{dF}{dA} = E\frac{y}{R}\,, \tag{A.2}$$

where E is a 'spring constant,' more commonly known as the material's *Young's modulus*.

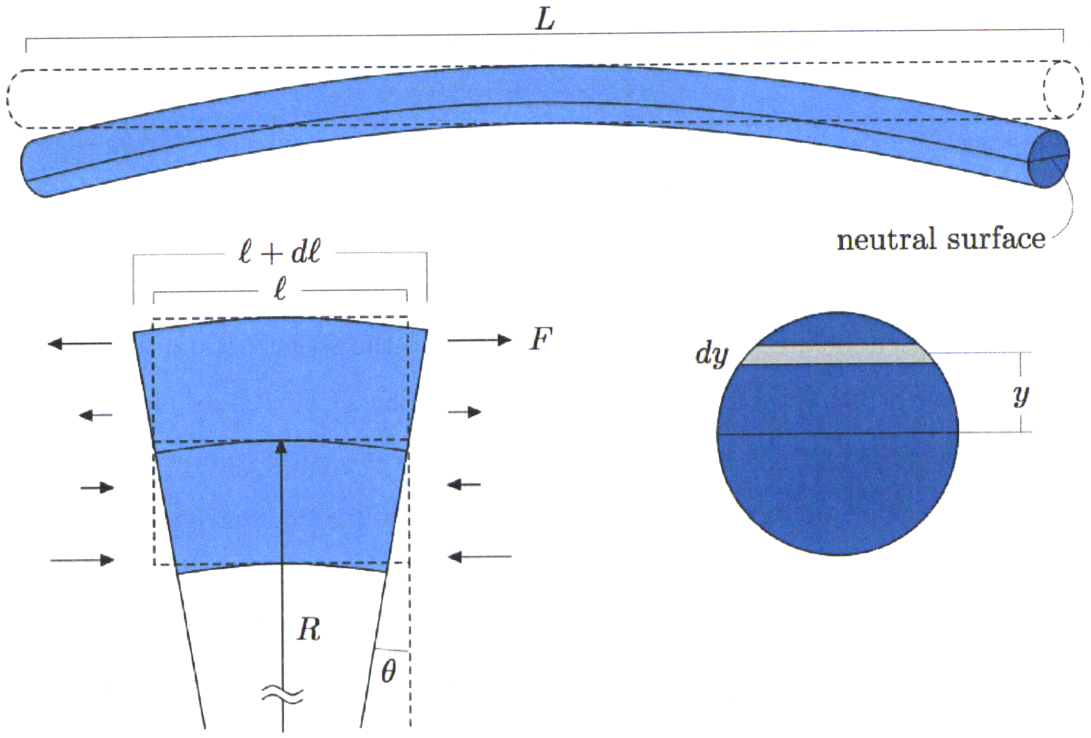

Figure A-1: Geometry of a bent rod (Figure reproduced from [112]).

The stretching forces above the neutral surface and compressive forces below produce a bending moment M about the neutral surface:

$$\begin{aligned} M &= \int_{\text{area}} y\, dF \\ &= \frac{E}{R}\int_{\text{area}} y^2\, dA \\ &= \frac{EI}{R}\,, \end{aligned} \tag{A.3}$$

where the product of I (the *bending moment of inertia* reflecting the geometry of the rod) and E (the Young's modulus reflecting the material composition of the rod) gives the *flexural rigidity* EI, which is a measure of the rod's resistance to bending. The resulting *beam*

equation (Eq. (A.3)) shows that the moment, and thus the energy, of a straight rod having $R = \infty$ is 0, while that of a strongly curved rod is $\gg 0$.

A.2 Wormlike Chain Model

The wormlike chain model for biopolymers is inspired by the continuum approach described above. We begin, once again, with a continuous space curve, parametrized by the arc length s that follows along the contour of the curve (Fig. A-2, left panel). Each point $\mathbf{r}(s)$ along

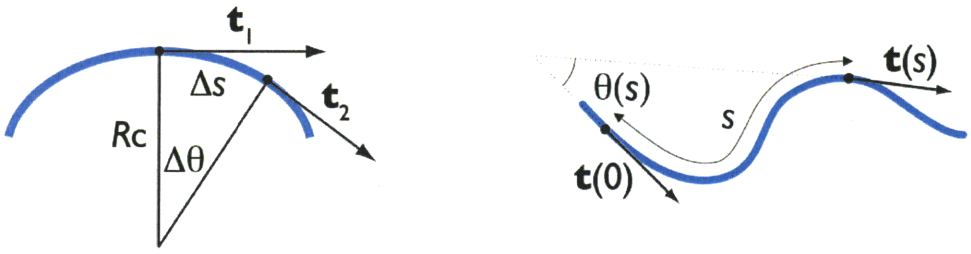

Figure A-2: Wormlike chain space curves bent with constant curvature R_c (left panel) and varying curvature (right panel). $\theta(s)$ is the angle subtended by the arc length s, or equivalently, the change in direction of the unit tangent vector, $\mathbf{t}$, between two points along the arc.

the curve has a unit tangent vector $\mathbf{t}$ that, in the limit of an infinitesimally small arc length segment, can be written as

$$\mathbf{t}(s) = \frac{\partial \mathbf{r}(s)}{\partial s} \tag{A.4}$$

We are interested in how $\mathbf{t}$ changes along the curve, for instance, between positions 1 and 2 (Fig. A-2, left panel). When these positions are infinitesimally close, this rate of change is commonly referred to as the *curvature*,

$$C\hat{\mathbf{n}} = \frac{\partial \mathbf{t}(s)}{\partial s}\ , \tag{A.5}$$

with $\hat{\mathbf{n}}$ the unit normal to the curve. It can subsequently be shown that the magnitude of the curvature is just the reciprocal of the local radius of curvature of the arc, R_c:

$$C = 1/R_c \tag{A.6}$$

The energy associated with the bending deformation shown in Fig. A-2 (left panel) is taken as harmonic with the curvature. Applying *Hooke's law* with the curvature yields

$$E_{\text{arc}} = \frac{1}{2} k C^2 \ , \tag{A.7}$$

a result that can be related to the continuum mechanics of the "the bent rod" [57]:

$$\begin{aligned} \frac{E_{\text{arc}}}{L_0} &= \frac{\kappa_F}{2R_c^2} = \frac{EI}{2R_c^2} \\ &= \frac{1}{2} EI \left(\partial \mathbf{t}(s)/\partial s\right)^2 \ , \end{aligned} \tag{A.8}$$

where L_0 is the contour length of the polymer, i.e., the space curve's full arc length.

Unlike in the case of Fig. A-2 (left panel), biopolymers do not, in general, exhibit constant curvature along the length of the filament. Instead, their curvature varies as a function of s, as depicted in Fig. A-2 (right panel); therefore, we can generalize Eq. (A.8) to obtain the well-known Kratky-Porod model,

$$\boxed{E_b = \frac{1}{2} \kappa_F \int_0^{L_0} \left(\partial \mathbf{t}(s)/\partial s\right)^2 ds} \ , \tag{A.9}$$

which serves as the basis for wormlike chain models.

According to this model, energy is minimized when the filament is in the straight configuration. Biopolymers, however, fluctuate and adopt contorted configurations as they exchange thermal energy with the environment at finite temperatures. As a result, the configuration of a filament is the result of a competition between bending energy and entropy, where bending energy minimization seeks to straighten it while entropy maximization seeks to deform it. Statistical mechanics thus becomes the framework for extracting useful thermodynamic variables. In particular, we begin with the most fundamental of statistical mechanics concepts – that the probability $\mathcal{P}(E_b)$ of finding the filament in a specific configuration with energy E_b is proportional to the Boltzmann factor $\exp\left[-\beta E_b\right]$, where $\beta = 1/k_B T$. From here, a partition function of all possible space curve configurations can be built and subsequently used to determine ensemble averages of interest, such as the average end-to-end distance

$\langle r \rangle$ (or extension, $\langle x \rangle$) of the polymer. Before beginning the nontrivial task of obtaining a wormlike chain's average extension, it is useful to introduce one important concept. The *persistence length* is a parameter that governs the variation in the direction of tangent vectors at different positions along the curve. It arises mathematically in the result for the tangent correlation function:

$$\langle \mathbf{t}(0) \cdot \mathbf{t}(s) \rangle = \exp\left[-s/l_p\right] , \tag{A.10}$$

where the first term is the time-averaged inner product of two tangent vectors (Fig. A-2, right panel). The persistence length l_p thus measures the length over which the tangent vectors become uncorrelated, in other words, the length scale over which thermal bending becomes signifiant. Intuitively, one would predict that this length scale represents a balance of mechanical (κ_F) and thermal ($k_B T$) effects, and indeed this was shown to be true by Doi & Edwards [27] in a well-known result for the persistence length:

$$l_p = \frac{\kappa_F}{k_B T} = \frac{EI}{k_B T} \tag{A.11}$$

Hence, polymers with relatively short persistence length appear floppy (e.g., dsDNA), whereas polymers with long persistence length appear rigid (e.g., microtubules). In general, a polymer is referred to as *semiflexible* if its persistence length is much larger than the filament diameter or monomer size, or alternatively, if the ratio of L_0/l_p is of the order of one. This class includes dsDNA, F-actin, and microtubules.

A.3 End-to-End Distribution Function: A Monte Carlo Study

A key observable in the study of semiflexible polymers is the end-to-end distance r (or extension x) for a given contour length L_0 and persistence length l_p. This quantity, which is actually a distribution function or probability density, is known exactly for a freely jointed chain [124] and, for most purposes, can be approximated by a simple Gaussian. An exact and all-encompassing end-to-end distribution function for semiflexible polymers, however, is

not known. An approximate solution for 'almost fully flexible polymers' ($L_0/l_p > 0$) was obtained through corrections to the Gaussian distribution [38]. For general L_0/l_p, analytical expressions exist for the lowest even moments of the distribution [40] and numerical results exist for higher even moments [125]. For semiflexible polymers approaching the stiff limit, all even moments of the distribution have been calculated [40]. More recently, an analytical distribution function was approximated for semiflexible polymers with small L_0/l_p and was shown to compare favorably with Monte Carlo simulation data [119].

We can numerically determine the end-to-end distribution function for a given L_0 and l_p by implementing a Monte Carlo simulation of a discretized version of the wormlike chain. The polymer chain is composed of N short segments of fixed length $1/N$ and direction $\mathbf{t}$ with a total effective bending energy

$$\mathcal{H} = \frac{\kappa_F}{2} \int_0^{L_0} \left(\frac{\partial \mathbf{t}(s)}{\partial s} \right)^2 ds \quad \longrightarrow \quad \tilde{\mathcal{H}} = l_p N \sum_{i-1}^{N-1} \mathbf{t}_i \cdot \mathbf{t}_{i+1} \tag{A.12}$$

The standard Metropolis algorithm was used to numerically build the end-to-end probability

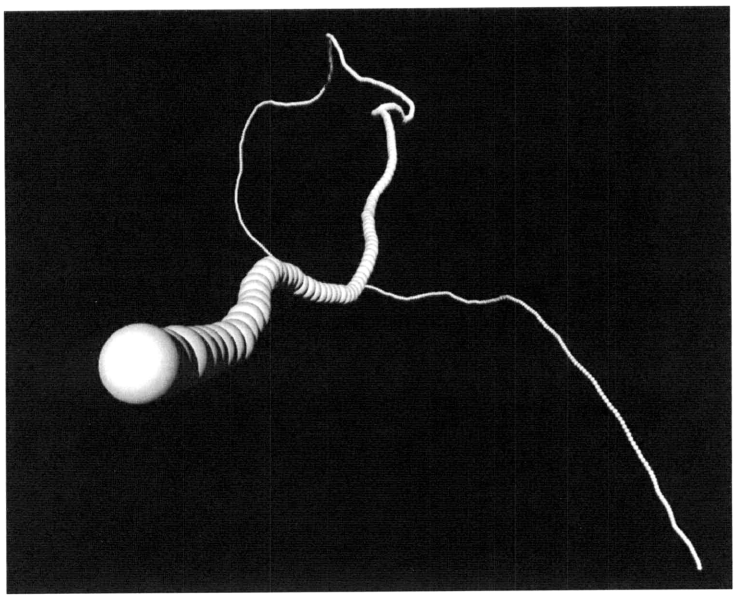

Figure A-3: Representative wormlike chain from Monte Carlo simulation.

densities (for $L_0/l_p = 0.5, 0.7, 1, 2, 5, 10$) by performing on the order of 10^5 Monte Carlo steps per segment (Fig. A-4, left panel). In each step, a hinge between two segments is chosen

at random. The downstream segments are then subjected to a three-dimensional rotation matrix, and the resulting configuration is accepted or rejected according to the Metropolis algorithm. In essence, a random walk is performed through the wormlike chain's configuration space, and the ensemble of "allowable" configurations is generated. Not surprisingly, Fig. A-4 (left panel) confirms that for a given L_0, shorter persistence lengths yield smaller average end-to-end distances $\langle r \rangle$, whereas longer persistence lengths yield end-to-end distances that approach the chain's contour length. The respective tangent correlation functions (Fig. A-4,

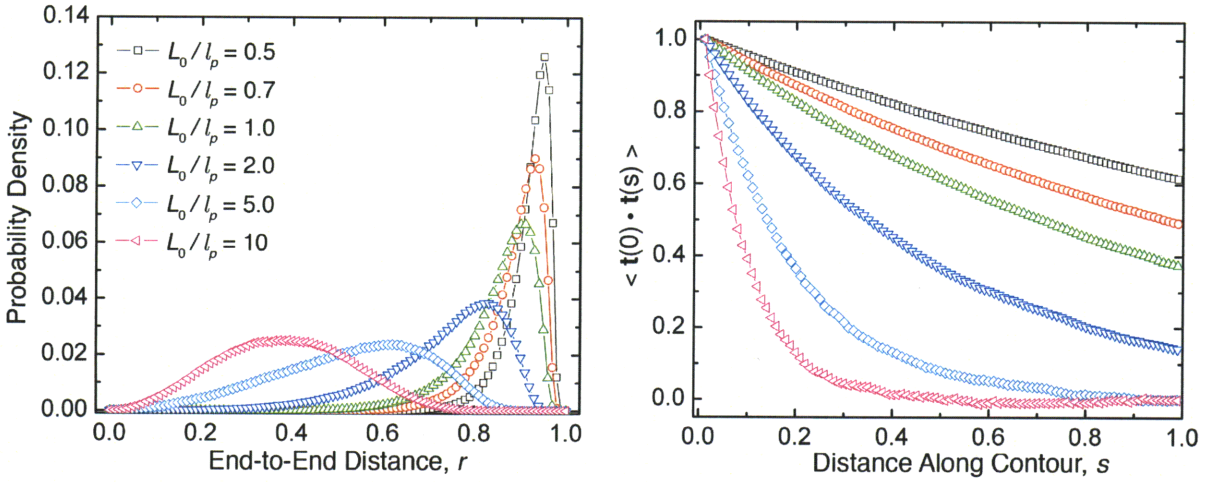

Figure A-4: End-to-end distribution functions (left panel) and tangent correlation functions (right panel) for $L_0/l_p = 0.5, 0.7, 1, 2, 5, 10$.

right panel), depicting the predicted exponential decay behavior, complement the end-to-end distribution functions in showing that wormlike chains with shorter l_p become 'thermally uncorrelated' easier than those with longer l_p.

The final key observation from this Monte Carlo study, and the motivation for always seeking the appropriate form of the wormlike chain model, is that the end-to-end ensembles show *increasing asymmetry* with increasing L_0/l_p (Fig. A-4, left panel). The deviation away from near-Gaussian behavior has profound consequences for relating single-molecule measurements to the thermodynamics of the biological system. In particular, we see that the average end-to-end extension $\langle x \rangle$ is no longer equal to, or approximately equal to, the most probable extension x_{MP} (Fig. A-4, left panel). Therefore, for single-molecule stretching of "short" polymer molecules (i.e., those with smaller L_0/l_p that are *not* in the "thermodynamic limit" of long polymers), this means that the isometric (constant extension) and isotensional

(constant force) ensembles vary [47]. Of course, the probability distributions of Fig. A-4 (left panel) do not represent the experiment of a wormlike chain undergoing uniaxial stretching; however, the trend in the distributions is the same [47]. Therefore, depending on which ensemble is assumed when solving the wormlike chain model, care must be taken to experimentally fix the appropriate thermodynamic variable (extension x or force F) and measure fluctuations in the other.

A.4 Fluctuating Rod Limit

In this section, we consider the mechanical properties of semiflexible polymers with contour length comparable to persistence length ($L_0/l_p \leq 2$) and derive the force-extension (F-x) relationship for this "fluctuating rod" limit of the wormlike chain model. In this limit, which is applicable to "short chains" *or* long chains being stretched by large forces, the probability of large deviations away from the straight configuration (or direction of applied force) is small. Thus, only small, quadratic fluctuations around the energy-minimizing configuration need be considered, an assumption that leads to an analytical solution suited for data fitting. Following the derivation in [41], we apply a generating functional method, commonly used in quantum field theory, for extracting statistical properties of fluctuating rods. Finally, it should be noted that other methods have been used to arrive at the same solution.

We begin with the Hamiltonian of a wormlike chain being stretched by a constant force f in the $\hat{\mathbf{x}}$ direction:

$$\frac{E}{k_B T} = \int_0^{L_0} \frac{1}{2} l_p \left(\frac{\partial^2 \mathbf{r}(s)}{\partial s^2} \right)^2 ds - f\hat{\mathbf{x}} \,, \tag{A.13}$$

where we can insert

$$\mathbf{x} \equiv \hat{\mathbf{x}} \cdot (\mathbf{r}(L_0) - \mathbf{r}(0))$$

into the Hamiltonial to obtain

$$\frac{E}{k_B T} = \int_0^{L_0} \frac{1}{2} l_p \left(\frac{\partial^2 \mathbf{r}(s)}{\partial s^2} \right)^2 ds - f\hat{\mathbf{x}} \cdot (\mathbf{r}(L_0) - \mathbf{r}(0))$$

Recalling that

$$\mathbf{t}(s) = \frac{\partial \mathbf{r}(s)}{\partial s} ,$$

the Hamiltonian can then be expressed in terms of the tangent vectors[1]:

$$\begin{aligned} E &= k_B T \int_0^{L_0} \left[\frac{1}{2} l_p \left(\frac{\partial \mathbf{t}(s)}{\partial s} \right)^2 ds - f \underbrace{\hat{\mathbf{x}} \cdot \mathbf{t}(s)}_{\cos\theta(s)} \right] ds \\ &= k_B T \int_0^{L_0} \left[\frac{1}{2} l_p \left(\frac{\partial \mathbf{t}(s)}{\partial s} \right)^2 - f \cos\theta(s) \right] ds \end{aligned}$$

We now consider the limit of small fluctuations, where the tangent vector makes only small deviations away from the applied force. In this case, we can invoke a quadratic approximation of the form

$$\cos\theta(s) \approx 1 - \frac{\theta(s)^2}{2} ,$$

giving the resulting Hamiltonian

$$\begin{aligned} E &= k_B T \int_0^{L_0} \left[\frac{1}{2} l_p \left(\frac{\partial \mathbf{t}(s)}{\partial s} \right)^2 - f \left(1 - \frac{\theta(s)^2}{2} \right) \right] ds \\ &= k_B T \left[-f L_0 + \int_0^{L_0} \left(\frac{1}{2} l_p \left(\frac{\partial \mathbf{t}(s)}{\partial s} \right)^2 + f \frac{\theta(s)^2}{2} \right) ds \right] \end{aligned}$$

At this point, we will restrict the analysis to $n = 2$ dimensions[2], where it is easy to see that the tangent vector $\mathbf{t}$ is completely specified by the scalar $\theta(s)$, such that $\mathbf{t}(s) = (1, \theta(s))$ (this can be shown by writing the unit vector $\mathbf{t}$ in polar coordinates: $\mathbf{t} = t_x \hat{\mathbf{x}} + t_y \hat{\mathbf{y}} = \overset{1}{\underset{\sqcup}{r}} \hat{\mathbf{r}} + \theta\hat{\theta}$). As a result, the tangent partial derivative above can be replaced by

$$\frac{\partial \mathbf{t}(s)}{\partial s} = \left(0, \frac{d\theta(s)}{ds} \right) \quad \longrightarrow \quad \left(\frac{\partial \mathbf{t}(s)}{\partial s} \right)^2 = \left(\frac{d\theta(s)}{ds} \right)^2$$

[1]The end of the filament points in the direction of the applied force ($\hat{\mathbf{x}}$), therefore, we can assume that $\hat{\mathbf{x}} \cdot \mathbf{t}(s) \equiv \mathbf{t}(0) \cdot \mathbf{t}(s) = \cos\theta(s)$, where, once again, $\theta(s)$ is the angle subtended by the arc length s or equivalently the change in direction of the unit tangent vector $\mathbf{t}$ along the arc (See Fig. A-2, right panel).

[2]The general d-dimensional space derivation is essentially analogous and can be found in [41].

The Hamiltonian can now be written as

$$E = k_B T \left[-fL_0 + \int_0^{L_0} \left(\frac{1}{2} l_p \left(\frac{d\theta(s)}{ds} \right)^2 + f \frac{\theta(s)^2}{2} \right) ds \right] \tag{A.14}$$

We seek the average extension,

$$\langle x \rangle = \langle \int_0^{L_0} \cos\theta(s)\, ds \rangle \approx \langle \int_0^{L_0} 1 - \frac{\theta(s)^2}{2}\, ds \rangle = L_0 - \int_0^{L_0} \frac{\langle \theta(s)^2 \rangle}{2}\, ds \,, \tag{A.15}$$

therefore, we need to obtain $\langle \theta(s)^2 \rangle$. From basic statistical mechanics, the average value is calculated by

$$\langle \theta^2 \rangle = \frac{\sum_i \theta_i^2 e^{-\beta E_i}}{\sum_i e^{-\beta E_i}}$$

or, in terms of a *path integral for the partition function* over all possible polymer conformations:

$$\begin{aligned} \langle \theta(s)^2 \rangle &= \int \mathcal{D}\left[\text{all paths}\right] \theta(s)^2 e^{-\beta E} \Big/ \int \mathcal{D}\left[\text{all paths}\right] e^{-\beta E} \\ &= \left[e^{-fL_0} \int \mathcal{D}\left[\text{all paths}\right] \theta(s)^2 e^{-\beta H} \right] \Big/ \left[e^{-fL_0} \int \mathcal{D}\left[\text{all paths}\right] e^{-\beta H} \right] \\ &= \int \mathcal{D}\left[\text{all paths}\right] \theta(s)^2 e^{-\beta H} \Big/ \underbrace{\int \mathcal{D}\left[\text{all paths}\right] e^{-\beta H}}_{\mathcal{Z}=\text{partition function}} \,, \end{aligned} \tag{A.16}$$

where the new Hamiltonian is

$$H = k_B T \left[\int_0^{L_0} \left(\frac{1}{2} l_p \left(\frac{d\theta(s)}{ds} \right)^2 + f \frac{\theta(s)^2}{2} \right) ds \right]$$

The first integral in the Hamiltonian can be integrated by parts:

$$\int_0^{L_0} \left(\frac{d\theta(s)}{ds} \right)^2 = \underbrace{\left[\theta(s) \frac{d\theta(s)}{ds} \right]_0^{L_0}}_{=0} - \int_0^{L_0} \theta(s) \frac{d^2\theta(s)}{ds^2}\, ds \,,$$

where the first term on the right vanishes because we have imposed a *boundary condition* that the filament ends be collinear (i.e., aligned in the direction of the applied force): $\theta(L_0) = \theta(0)$.

Inserting this integral back into the Hamiltonian gives

$$\begin{aligned}
\beta H &= \int_0^{L_0} \left[l_p \left(-\theta(s) \frac{d^2\theta(s)}{ds^2} \right) + \frac{\beta f \theta(s)^2}{2} \right] ds \\
&= \frac{1}{2} \int_0^{L_0} \theta(s) \underbrace{\left[-l_p \frac{d^2}{ds^2} + \beta f \right]}_{\mathcal{O}(s)} \theta(s)\, ds \\
&= \frac{1}{2} \int_0^{L_0} \theta(s)\, \mathcal{O}(s)\, \theta(s)\, ds \,, \qquad \text{(A.17)}
\end{aligned}$$

where $\mathcal{O}(s)$ is a differential operator.

In order to solve for $\langle \theta(s)^2 \rangle$ (Eq. (A.16)), we introduce a generating functional, $\mathcal{Z}[J]$, by adding a source term, $J\theta(s)$, to the Hamiltonian:

$$\begin{aligned}
\mathcal{Z}[J] &= \int \mathcal{D}\left[\text{all paths}\right] e^{-\beta H + J\theta(s)} \\
&= \int \mathcal{D}\left[\text{all paths}\right] e^{\left[-\frac{1}{2} \int_0^{L_0} \theta(s)\, \mathcal{O}(s)\, \theta(s)\, ds + J\theta(s) \right]}
\end{aligned}$$

Employing the quantum field theory trick of completing the squares[3] [88], we find that the correlation function is

$$\langle \theta(s)\theta(s') \rangle = \lim_{J \to 0} \frac{d^2 \log\left(\mathcal{Z}[J]\right)}{dJ^2} = G(s, s') \,, \qquad \text{(A.18)}$$

is the Green's function, $G(s, s')$, of the differential operator:

$$\mathcal{O}(s)\, G(s, s') = \delta(s - s') \qquad \text{(A.19)}$$

The above result allows us to calculate the average extension. First, the differential equation

$$-l_p \frac{d^2 G(s, s')}{ds^2} + \beta f G(s, s') = \delta(s - s') \qquad \text{(A.20)}$$

is solved for $G(s, s')$ in the two cases for which the delta function is 0 ($s < s'$ and $s > s'$), and the two solutions are equated at $s = s'$ to satisfy continuity. Next, the final boundary

[3] Letting $\theta(s) = \theta(s') - JG(s, s')$ and applying it to the modified Hamiltonian: $-\beta H + J\theta(s) = -\frac{1}{2} \int_0^{L_0} \theta(s)\, \mathcal{O}(s)\, \theta(s)\, ds + J\theta(s)$

condition is obtained by integrating Eq. (A.20) from $(s-\epsilon)$ to $(s+\epsilon)$ and taking the limit $\epsilon \to 0$. The two solutions are combined, along with the final boundary condition, to obtain the complete Green's function, $G(s,s')$. Finally, setting $s = s'$ so that $\langle\theta(s)\theta(s')\rangle = \langle\theta(s)^2\rangle$, we can insert the Green's function into Eq. (A.15) and integrate to obtain the final average extension:

$$\boxed{\langle x\rangle = L_0 - \frac{k_B T}{2F}\left[L_0\sqrt{\frac{F}{\kappa_F}}\coth\left(L_0\sqrt{\frac{F}{\kappa_F}}\right) - 1\right]} \tag{A.21}$$

Appendix B

M13 Protocols

B.1 Preparation of Biotin-H_6 Phage

Day 0

1. Prepare overnight culture (OC): 20 mL LB, 20 μL 1000X tetracycline,[1] 20μL 1000X chloramphenicol,[2] 1 colony of p9-H_6 (030417) *E. coli* in sterilized 250 mL flask. Shake in 37°C shaker overnight ($\sim 12 - 16$ hrs).

Day 1

1. Dilute 200 μL OC in 20 mL LB with 20 μL of appropriate antiobiotic solution(s) and 2 μM sodium selenite[3] in *two*, new sterilized 250 mL flask. Shake at 37°C until early log phase ($OD_{600nm} = 0.2 - 0.4$).

2. Infect bacteria with ~ 35 μL of 10^9 phage/μL *Sec1*.

3. Place flasks in 37°C incubator for 5-10 minutes. Induce with 1mM IPTG (200-250 μL of 100 mM stock solution). Place flasks back in 37°C incubator for 1 hour. Then, shake at 37°C for > 8 hrs.

[1] 1000X TET solution = 20 mg/mL tetracycline in methanol
[2] 1000X CHLR solution = 35 mg/mL chloramphenicol in ethanol
[3] Freeze 200 μM stock solutions and store working aliquots in 2-8°C for 1 month.

4. Pour contents of flasks into sterilized, large centrifuge tubes. Balance tubes with LB, and spin at 10,000 RPM (rotor ID JA25.50, 4°C) for 15 minutes to pellet out bacteria.

5. Pour supernatant into new sterilized, large centrifuge tubes, taking care not to disrupt bacterial pellet. Add 1/6 volume PEG/NaCl to phage solutions ($\sim$ 3.33 mL PEG/NaCl), invert, and store in 4°C overnight, or on ice for 2 hrs.

Day 2

1. Spin phage-PEG/NaCl solution at 12,000 RPM (rotor ID JA25.50, 4°C) for 20 minutes to pellet out phage.

2. While phage solution is spinning, prepare 4 mM I-Bt (EZ-Link Iodoacetyl-PEO_2-Biotin, Pierce #21334) in TBS buffer (2.2 mg/mL). As much as possible, keep this solution in the dark and free from moisture.

3. Carefully pour out and discard supernatant. Resuspend phage precipitates in 375 μL sodium acetate buffer solution (30 mM acetate buffer, pH 5.2), yielding a total volume of 750 μL phage–ABS solution.

4. Perform biotinylation reaction in the dark by adding 250 μL I-Bt solution to 750 μL phage and let incubate 45-60 min.

5. Add 1/6 volume PEG/NaCl ($\sim$ 200 μL) to the mixture and precipitate phage on ice for 30-60 additional minutes. If possible, keep this mixture in the dark.

6. Spin resulting phage-PEG/NaCl solution in microcentrifuge at 12,000 RPM for 15 minutes.

7. Carefully pour and/or pipette out supernatant. Add 1mL TBS and 200 μL PEG/NaCl *without* disturbing the pellet. Then spin for an additional 1-3 minutes.

8. Carefully pour and/or pipette out supernatant. Resuspend phage precipitate in 200 μL – 500 μL TBS, depending on size of pellet and desired concentration of final phage solution, by once again pipetting up and down and gently vortexing. Store in 4°C

(Note: after allowing phage to resuspend in TBS for a few hours, it is worthwhile to do a final bacteria removal spin at 10,000 RPM for < 1 minute).

B.2 Inverted Protocol for Single-Molecule M13 Tethers

Materials

1. **Penta-His Antibody** (Qiagen, Cat No. 34660, 100 μg lyophilized, 1 year storage at 2-8°C). Reconstitute with 500 μL PBS buffer or deionized water and store in -20°C in 10 μL aliquots.

2. **TBS** (100 mM Tris HCl, 150 mM NaCl, pH 7.5).

3. **PBS** (100 mM Phosphate Buffer, pH 7.5). 1860 μL 1 M NaH_2PO_4, 8140 μL 1 M Na_2HPO_4, 90 mL ddH_2O, filter through 0.22 μm filter.

4. **PBT** (100 mM Phosphate Buffer, pH 7.5, 0.1% Tween–20). 1860 μL 1 M NaH_2PO_4, 8140 μL 1 M Na_2HPO_4, 90 mL ddH_2O, 100 μL Tween–20, filter through 0.22 μm filter.

5. **Casein-PBT** (10 mg/mL Casein in PBT, stored for one week at 4°C).

6. **Streptavidin–Coated 0.440 μm Polystyrene Beads** (Spherotech, Cat No. SVP-05-10, 1.0% w/v).

7. **B–H_6 Phage**. Amplify phage using appropriate phagemid system (p9–H_6 phagemid *E. coli*) to a concentration $> 10^8$ phages/μL.

Protocol

1. Construct 10–20 μL flow channel from glass slide and KOH-etched coverslip.

2. Flow in 40 μL of 20 μg/mL Penta–His Antibody (diluted in PBS). Incubate for $>$ 45 minutes at room temperature in humidity chamber.

3. Flow in 200 μL of 3 mg/mL Casein–TBS using slow vacuum. Incubate for 20 minutes at room temperature.

4. Dilute 20 μL beads into 80 μL PBS. Start spinning down beads: 4 rounds of 6 minutes at 10.000 rpm. After each of the first three spins, pipette away supernatant and resuspend in the same volume of PBS. After final spin, pipette away supernatant and resuspend in 100 μL 0.1 mg/mL Casein–TBS. Finally, sonicate at 40% for 2 minutes.

5. Wash flow channel with 50 μL TBS.

6. Flow in 20–40 μL B–H_6 Phage solution. Incubate for 25–30 minutes.

7. Wash with 100μL 0.1 mg/mL Casein–TBS.

8. Flow in 40 μL washed beads. Incubate for 25–30 minutes.

9. Wash with 200 μL TBS or 0.1 mg/mL Casein–TBS.

B.3 Engineering Zinc Fingered-Phages: Zif268–M13

Materials

1. **pB1H1 Vector**. Parent vector containing Zif268 gene.
2. **M13KE Cloning Vector** (Ph.D. Peptide Display Cloning System, New England Biolabs, Cat No. E8101S).
3. **Taq DNA Polymerase** (Invitrogen, Cat No. 10342020).
4. **Zif268 Primers**
   (a) 3-Finger Forward: CAT GCC CGG GTA CCT TTC TAT TCT CAC TCT **GAA CGC CCA TAT GCT TGC CCT G**
   (b) 3-Finger Reverse: **GGC GGC G**CA TGT TTC GGC CGA **GTC CTT CTG TCT TAA ATG GAT**
   (c) 2-Finger Forward: CAT GCC CGG GTA CCT TTC TAT TCT CAC TCT **GAA CGC CCA TAT GCT TGC CCT G**
   (d) 2-Finger Reverse: CA TGT TTC GGC CGA **TGT GTG GGT GCG GAT GTG GGT**
5. **dNTP Mix** (2.5 mM, Invitrogen, Cat No. R72501).
6. **EagI Restriction Endonuclease** (10,000 U/mL, New England Biolabs, Cat No. R0505S).
7. **Acc65I Restriction Endonuclease** (10,000 U/mL, New England Biolabs, Cat No. R0599S).
8. **Antarctic Phosphatase** (5,000 U/mL, New England Biolabs, Cat No. M0289S).
9. **T4 DNA Ligase** (400,000 U/mL, New England Biolabs. Cat No. M0202S).
10. **XL-1-Blue Electroporation-Competent Cells** (Stratagene, Cat No. 200228).

11. **QIAquick PCR Purification Kit** (Qiagen Cat No. 28104).

12. **QIAprep Spin M13 Kit** (Qiagen Cat No. 27704).

13. **TET/IPTG/XGAL LB plates**. LB agar plate supplemented with 20 μg/mL tetracycline, 0.1 mM IPTG, 40 μg/mL Xgal.

14. **LB-TET-Zn**. LB broth supplemented with 20 μg/mL tetracycline, 50 μM zinc acetate.

Amplification of Zif268 Gene Insert

1. Prepare PCR reaction:

   60 ng pB1H1 vector

   4 μL 2.5 mM dNTPs

   0.5 μL Taq polymerase

   5 μL Taq buffer

   1.5 μL 50 mM $MgCl_2$

   5 μL 10 μM Forward primer

   5 μL 10 μM Reverse primer

   xx μL H_20

   ---

   50 μL total

   PCR: 95°C – 50°C – 72°C (32 cycles)

2. Run 4 μL of PCR reaction on a diagnostic gel (1% (w/v) agarose).

3. Purify remaining DNA with QIAquick PCR Purification Kit[4], eluting with 30 μL H_2O.

[4]Depending on *size* of insert

Digestion Reactions

1. Prepare 2 digestion reactions:

   2 μg M13KE vector (1.5 μg PCR product)

   8 μL Buffer 3 (5 μL)

   0.8 μL 100X BSA (5 μL)

   2 μL EagI (1 μL)

   2 μL Acc65I (1 μL)

   xx μL H_2O

   ---

   80 μL total (50 μL total)

   37°C (overnight), 65°C heat kill (20 minutes).

2. Run 4 μL of digested insert on a diagnostic gel (1% (w/v) agarose).

3. Purify remaining insert DNA with QIAquick PCR Purification Kit, eluting with 30 μL H_2O.

4. Purify digested vector with QIAquick PCR Purification Kit, eluting with 30 μL H_2O.

Vector Dephosphorylation

1. Prepare vector dephosphorylation reaction:

   30 μL M13KE vector

   5 μL Buffer 3

   0.5 μL Antarctic Phosphatase

   14.5 μL H_2O

   ---

   50 μL total

37°C (30 minutes); 65°C heat kill (20 minutes).

2. Purify vector with QIAquick PCR Purification Kit, eluting with 30 μL H_2O.

Ligation

1. Prepare ligation reactions:

	Molar Ratio (Insert:Vector)†	
	0	3
Vector	50 – 100 ng	50 – 100 ng
Insert	0	$\sim$ 6 – 12 ng
Ligase buffer	5 μL	5 μL
T4 DNA Ligase	0.5 μL	0.5 μL
H_2O	xx	xx
Total	50 μL	50 μL

†(ng vector) x [(kb insert) / (kb vector)] x (i:v molar ratio) = (ng insert).

16°C overnight; 65°C heat kill (10 minutes).

Cloning Transformation

1. Transform XL-1-Blue Electroporation-Competent Cells with ligation reactions.

2. After shaking cells for 1 hr. at 37°C, add 50 – 100 μL of cells to melted top agarose, and spread onto TET/IPTG/XGAL LB plates. Incubate plates at 37°C overnight.

3. Dilute ER2738 overnight culture 1:100 in LB-TET-Zn. Inoculate 1 – 2 mL of diluted culture with single blue plaque from LB plates and shake at 37°C for 4 – 5 hrs.

4. Purify DNA plasmids using QIAprep Spin M13 Kit and sequence with appropriate sequencing primer (e.g., –96 gIII).

B.4 Preparation of Zif268–H_6 Phage

Day 0

1. Prepare overnight culture (OC): 20 mL LB-TET-CHLR-Zn,[5] 1 colony of p9-H_6 (030417) *E. coli* in sterilized 250 mL flask. Shake in 37°C shaker overnight ($\sim 12 - 16$ hrs).

Day 1

1. Dilute 200 μL OC in 20 mL LB-CHLR-Zn in sterilized 250 mL flask. Shake at 37°C until early log phase ($OD_{600nm} = 0.2 - 0.4$).

2. Infect bacteria with $\sim 30 - 35$ μL of 10^9 phage/μL Zif268–M13.

3. Place flasks in 37°C incubator for 5-10 minutes. Induce with 1mM IPTG (200-250 μL of 100 mM stock solution). Place flasks back in 37°C incubator for 1 hour. Then, shake at 37°C for > 8 hrs.

4. Pour contents of flasks into sterilized, large centrifuge tubes. Balance tubes with LB, and spin at 10.000 RPM (rotor ID JA25.50, 4°C) for 15 minutes to pellet out bacteria.

5. Pour supernatant into new sterilized, large centrifuge tubes, taking care not to disrupt bacterial pellet. Add 1/6 volume PEG/NaCl to phage solutions ($\sim$ 3.33 mL PEG/NaCl), invert, and store in 4°C overnight, or on ice for 2 hrs.

Day 2

1. Spin phage-PEG/NaCl solution at 12,000 RPM (rotor ID JA25.50, 4°C) for 20 minutes to pellet out phage.

2. Carefully pour out and discard supernatant. Resuspend phage precipitates in 1 mL TBSZ (100 mM Tris HCl, pH 7.5, 150 mM NaCl, 50 μM zinc acetate)

3. Add 1/6 volume PEG/NaCl ($\sim$ 200 μL) to the mixture and precipitate phage on ice for $1 - 2$ hrs.

[5] LB broth supplemented with 20 μg/mL tetracycline, 35 μg/mL chloramphenicol, 50 μM zinc acetate

4. Spin resulting phage-PEG/NaCl solution in microcentrifuge at 12,000 RPM for 15 minutes.

5. Carefully pour and/or pipette out supernatant. *Without* disturbing the pellet, spin for an additional 1 minute.

6. Carefully pour and/or pipette out supernatant. Resuspend phage precipitate in 200 μL ZBA (Zinc Buffer A: 10 mM Tris, pH 7.5, 90 mM KCl, 1 mM $MgCl_2$, 50 μM zinc acetate, 0.5 mM EDTA). Store in 4°C.

B.5 Zif268–M13 ELISA

Materials

1. **Neutravidin** (Pierce, Cat No. 31000).
2. **Zinc Buffer A, ZBA** (10 mM Tris, pH 7.5, 90 mM KCl, 1 mM $MgCl_2$, 50 μM zinc acetate, 0.5 mM EDTA). 10 mL 1 M Tris (pH 7.5), 30 mL 3 M KCl, 2 mL 0.5 M $MgCl_2$, 1 mL 50 mM zinc acetate, 1 mL 0.5 M EDTA, 956 mL ddH_2O, filter though 0.22 μm filter.
3. **Zinc Buffer B, ZBB**. ZBA, 1% (w/v) BSA.
4. **Zinc Buffer T, ZBT**. ZBA, 0.1% (v/v) Tween-20.
5. **TBS**. 100 mM Tris-HCl, pH 7.5, 150 mM NaCl.
6. **TBST**. TBS, 0.1% (v/v) Tween-20.
7. **Blocking Buffer** (5% (w/v) BSA in TBS or TBST).
8. **STE** (10 mM Tris HCl, pH 7.5, 1 mM EDTA, 50 mM NaCl). 2 mL 1 M Tris (pH 7.5 with HCl), 0.4 mL 500 mM EDTA (pH 8.0 with NaOH), 2 mL 5 M NaCl.
9. **NUNC MaxiSorp 96 Well Plate** (eBioscience, Cat No. 44-2404-21).
10. **HRP/Anti-M13 Monoclonal Conjugate** (GE Healthcare, Cat No. 27-9421-01).
11. **TMB**. 3,3',5,5' Tetramethylbenzidine liquid substrate system for ELISA (Sigma, Cat No. T0440).
12. **Zif268–M13**. $\sim 10^{12}$ phage/mL in ZBA.
13. **Biotinylated DNA**. Complementary oligonucleotides possessing the cognate Zif268 binding site (5'–...GCG TGG GCG...–3') and a biotin ([100 mM] in STE buffer).
    (a) **SNS**. Oligo 1: 5'–CCC TAT ATA **GCG TGG GCG** TAT ATA–3' ; Oligo 2: [Biotin]–5'–CGG TAT ATA CGC CCA CGC TAT ATA GGG–3'

Protocol

1. Incubate 1 μg Neutravidin (100 μL in TBS) in each well overnight at 4°C.
2. Anneal complementary oligonucleotides (120 μL of each in STE buffer). Dilute annealed DNA in a total of 7.5 mL STE.
3. Wash wells 3 times with 200 μL TBST.
4. Block wells with 200 μL Blocking Buffer for >2 hrs. at RT with agitation (400 rpm on orbital shaker).
5. Wash wells 3 times with TBST.
6. Add 100 μL diluted DNA solution to each well. Incubate for 2 hrs. at RT with agitation.
7. Wash wells 3 times with TBST.
8. Add 5-fold decreasing dilutions of Zif268–M13 (starting with 5×10^9/mL) in 100 μL ZBB into each well. Incubate for 2.5 hrs. at RT with agitation.
9. Wash wells 3 times with ZBT.
10. Dilute HRP/Anti-M13 1:5000 in ZBB. Add 100 μL of diluted conjugate to each well and incubate for 1 hr. at RT with agitation.
11. Wash wells 5 times with ZBT.
12. Equilibrate TMB substrate to RT. Add 100 μL of TMB to each well.
13. Read absorbances on plate reader at 652nm.

B.6 Inverted Protocol for Single-Molecule Zif268–M13 Tethers

Materials

1. **Penta-His Antibody** (Qiagen, Cat No. 34660, 100 μg lyophilized, 1 year storage at 2-8°C). Reconstitute with 500 μL PBS buffer or deionized water and store in -20°C in 10 μL aliquots.

2. **PBS** (100 mM Phosphate Buffer, pH 7.5). 1860 μL 1 M NaH_2PO_4, 8140 μL 1 M Na_2HPO_4, 90 mL ddH_2O, filter through 0.22 μm filter.

3. **PBT** (100 mM Phosphate Buffer, pH 7.5, 0.1% Tween–20). 1860 μL 1 M NaH_2PO_4, 8140 μL 1 M Na_2HPO_4, 90 mL ddH_2O, 100 μL Tween–20, filter through 0.22 μm filter.

4. **Casein-PBT** (10 mg/mL Casein in PBT, stored for one week at 4°C).

5. **Streptavidin–Coated 0.80 μm Polystyrene Beads** (Spherotech, Cat No. SVP-08-10, 1.0% w/v).

6. **Zinc Buffer A, ZBA** (10 mM Tris, pH 7.5, 90 mM KCl, 1 mM $MgCl_2$, 50 μM zinc acetate, 0.5 mM EDTA). 10 mL 1 M Tris (pH 7.5), 30 mL 3 M KCl, 2 mL 0.5 M $MgCl_2$, 1 mL 50 mM zinc acetate, 1 mL 0.5 M EDTA, 956 mL ddH_2O, filter though 0.22 μm filter.

7. **Zif268–H_6 Phage**. Amplify Zif268–M13 phage using appropriate phagemid system (p9–H_6 phagemid *E. coli*) to a concentration $> 10^8$ phages/μL.

8. **DNA**. Anneal complementary oligonucleotides possessing the cognate Zif268 binding site (5'–...GCG TGG GCG...–3') and a biotin.

   (a) **SNS**. Oligo 1: 5'–CCC TAT ATA **GCG TGG GCG** TAT ATA–3' ; Oligo 2: [Biotin]–5'–CGG TAT ATA CGC CCA CGC TAT ATA GGG–3'

   (b) **20R254T**. Oligo 1: [Biotin]–5'–CCC TAT ATA TTT AAG TTA ACA TCT AGA TTC TAT TTT TAG AAT CTA GAT GTT AAC TTT TTT ATA **GCG TGG**

GCG TAT A**GC GTG GGC G**TA–3' ; Oligo 2: 5'–TAC GGC CAC GCT ATA CGC CCA CGC TAT A–3'

Protocol

1. Dilute 20 μL beads into 80 μL PBS. Start spinning down beads: 4 rounds of 6 minutes at 10,000 rpm. After each of the first three spins, pipette away supernatant and resuspend in 100 μL PBS. After final spin, pipette away supernatant and resuspend in 100 μL 0.3 mg/mL Casein–ZBA. Finally, sonicate at 40% for 2 minutes. Final [bead] $\sim$ 12 pM.

2. Incubate 50 μL beads + 50 μL DNA (diluted to appropriate concentration in 0.3 mg/mL Casein–ZBA) on cold room rocker for 2 hrs.

3. Construct 10–20 μL flow channel from glass slide and KOH-etched coverslip.

4. Flow in 40 μL of 20 μg/mL Penta–His Antibody (diluted in PBS). Incubate for 1 hr. at RT in humidity chamber.

5. Flow in 200 μL of 3 mg/mL Casein–ZBA. Incubate for 30 minutes at room temperature.

6. Wash flow channel with 0.3 mg/mL Casein–ZBA.

7. Flow in 40 μL Zif268–H_6 phage solution (diluted 1:5 in ZBA). Incubate for 30 minutes at RT in humidity chamber.

8. Wash with 100μL 0.3 mg/mL Casein–ZBA.

9. Flow in 40 μL bead–DNA solution. Incubate for 30 minutes.

10. Wash with 100 μL 0.3 mg/mL Casein–ZBA.

B.7 Penta–His Antibody Coated Beads

Materials

1. **Penta–His Biotin Conjugate** (Qiagen, Cat No. 34440, storage at 2-8°C).
2. **TBS** (100 mM Tris HCl, 150 mM NaCl, pH 7.5).
3. **PBS** (100 mM Phosphate Buffer, pH 7.5). 1860 μL 1 M NaH_2PO_4, 8140 μL 1 M Na_2HPO_4, 90 mL ddH_2O, filter through 0.22 μm filter.
4. **PBT** (100 mM Phosphate Buffer, pH 7.5, 0.1% Tween–20). 1860 μL 1 M NaH_2PO_4, 8140 μL 1 M Na_2HPO_4, 90 mL ddH_2O, 100 μL Tween–20, filter through 0.22 μm filter.
5. **Casein–PBT** (10 mg/mL Casein in PBT, stored for one week at 4°C).
6. **Streptavidin–Coated Polystyrene Beads** (Spherotech, 1.0% w/v).

Protocol

1. Add 20 μL Penta–His Biotin to 10 μL beads.
2. Add 20 μL 1 mg/mL Casein–PBS.
3. Incubate for 1 hr. on rotator at 4°.
4. Remove unbound Penta–His Biotin by spinning 5 times at 10,000 RPM for 5 min. and resuspending in desired volume of PBS or 0.1 mg/mL Casein–PBS.

Appendix C

Kinesin Protocols

C.1 Tubulin Polymerizing Protocol

Materials

1. **PEM80**. 6.048 g Pipes (Sigma P–1851), 95.1 mg EGTA (Sigma E–4378), 204.1 μL of 4.9 M $MgCl_2$ (Mallinckrodt H590) stock into 250 mL final volume (80 mM Pipes, 1 mM EGTA, 4 mM $MgCl_2$, pH adjusted to 6.9 with KOH).

2. **PEM104**. 3.133 g Pipes (Sigma P1851), 49.452 mg EGTA (Sigma E4378), 128.57 μL of 4.9 M $MgCl_2$ (Mallinckrodt H590) stock into 100 mL final volume (103.6 mM Pipes, 1.3 mM EGTA, 6.3 mM $MgCl_2$, pH adjusted to 6.9 with KOH).

3. **STAB**. 34.1 μL PEM80, 5 μL 10 mM GTP (Cytoskeleton BST06), 4.7 μL 60 g/L NaN_3 (Sigma S–8032), 1.2 μL 10 mM Taxol (Cytoskeleton TXD01), 5.0 μL DMSO (Sigma D–5879).

4. **Tubulin** (Cytoskeleton T237).

Protocol

1. Spin tubulin for 30 min. at 4°.

2. Combine 15.2 μL PEM104 + 2.0 μL 10 mM GTP to make PEM/GTP solution.

3. Combine 15.2 μL PEM/GTP + 2.2 μL DMSO, vortex mixture, then add 4.8 μL of 10 mg/mL tubulin to make TUB solution.

4. Place TUB solution in water bath at 37° for 30 min.

5. Remove TUB from water bath and add 2 μL of STAB.

6. Store microtubules at room temperature.

C.2 Kinesin Expression and Purification

Materials

1. **LB Broth** (with 100 μg/mL ampicillin (amp) + 25 μg/mL chloramphenicol (chlr)).
2. **LB Plates** (with 100 μg/mL amp + 25 μg/mL chlr).
3. **TB Broth**. Add 47.6 g TB (Difco Terrific Broth) and 4 mL glycerol into 1 L ddH_2O and autoclave. Once cooled, add antibiotics (final: 100 μg/mL amp + 25 μg/mL chlr) + biotin (100 μM, 24 mg).
4. **1 M IPTG**. In water stored in 1 mL stocks at -20°.
5. **Rifampicin** (20 mM, 16.5 mg/mL in methanol, 100X stock, stored at -20° in 1 mL aliquots).
6. **Lysis Buffer** (20 mM imidazole, pH 7, 4 mM $MgCl_2$). Add 0.680 g imidazole and 0.5 mL of 4 M $MgCl_2$ into 500 mL ddH_2O.
7. **β-mercaptoethanol** (Neat liquid, room temperature).
8. **PMSF** (Sigma P7626). 200 mM in dry isopropanol, store at -20°.
9. **Pepstatin A** (Sigma P4265). 5 mg/mL in DMSO, store at -20°.
10. **TPCK** (Sigma T4376). 10 mg/mL in DMSO, store at -20°.
11. **TAME** (Sigma T4626). 40 mg/mL in ddH_2O, store at -20°.
12. **Leupeptin** (Sigma L9875). 5 mg/mL in ddH_2O, store at -20°.
13. **Soybean TI** (Type I–S, Sigma T9003). 10 mg/mL in ddH_2O, store at -20°.
14. **DNAse I** (solid, Grade II, Sigma D4527).
15. **RNAse A** (solid, Type II–A, Sigma R5000).
16. **Ni-NTA Resin** (Qiagen Ni-NTA Superflow).

17. **TCEP** (Molecular Probes T–2566). 10 mM in ddH_2O prepared *immediately* before use.

18. **Vivspin 15 Spin Column** (Vivascience VS1522, 30,000 MWCO).

19. **Protease Inhibitor Cocktail, PI**. Prepare 4 mL of PI and store at -20° in 250 μL aliquots:

Stock	Final Concentration (mg/mL)	Volume (μL)
Pepstatin A	0.2	160
TPCK	2.0	800
TAME	2.0	200
Leupeptin	0.2	160
Soybean IT	2.0	2.0
ddH_2O		1880

20. **Econo-Column Chromatography Columns** (Bio-Rad, Cat No. 737-1512, 1.5 x 10 cm, 18 mL).

21. **Bradford Reagent** (Sigma B6916).

22. **NuPAGE 4–12% Bis–Tris Gels** (Invitrogen, Cat No. NP0321BOX, 1.0 mm x 10 well).

23. **Kinesin Storage Buffer** (50 mM imidazole, pH 7. 100 mM $NaCl_2$, 1 mM $MgCl_2$, 20 μM ATP, 0.1 mM EDTA, 5% sucrose).

Day 0

1. Streak out fresh colonies of kinesin expressing *E. coli* (WT K401-BIO-H_6 is called KT2) on LB plate (+amp, +chlr). Grow overnight (12–16 hrs) at 37° and store parafilmed plate at 4° for up to one week.

Day 1

1. Pick single colony and inoculate 20 mL of LB broth (+amp, +chlr) in sterilized 250 mL flask.

2. Grow overnight (12–16 hrs) in 37° shaker.

Day 2

1. Inoculate 500 mL TB broth (+amp, +chlr, +biotin) with 5–10 mL volume of the LB overnight culture (time = 0). Grow culture in 37° shaker and record OD_{600} measurements.

2. Induce expression at OD_{600} = 0.53–0.60 by adding 1/1000 volume of 1 M IPTG stock (final concentration 1 mM). Upon induction, reset thermostat to 22°.

3. Add 1/100 volume of 20 mM rifampicin stock (5 mL into 500 mL culture) 2 hrs. after induction.

4. Keep culture shaking at 22° in a shaker overnight (12–20 hrs.).

Day 3

1. Pellet cells by centrifugation (5,000g, 4°, 10 min.).

2. To Lysis Buffer, add β-mercaptoethanol (final concentration 10 mM), 1/100 volume of PI, and 1/100 volume PMSF. This makes Full Lysis Buffer. Make 5 mL for each 500 mL culture.

3. After the spin, drain supernatant as much as possible and retain cell pellets. Resuspend pellets in 5 mL Full Lysis Buffer[1]. Dispense resuspension into sterilized 15 mL Falcon tube for freezing.

4. Incubate cell suspension 30 min. on ice, mixing occasionally (internal lysozyme degrades cell wall).

[1] A general rule is 100–150 μL buffer per 100 mg pellet

5. Freeze suspension in 5 mL aliquots in liquid nitrogen. The frozen mixture is stored at -80° at least overnight.

Day 4

1. Thaw frozen cells (5 mL) with alternating *brief* (2 min.) exposure to 37° water bath with agitation followed by *brief* (2 min.) cooling on ice. **The solution should never rise significantly above ice temperature.** At the point of complete thawing, refreeze the cells in liquid nitrogen. This process is repeated for a total of three thaws. Mixture becomes viscous and slightly darker in color.

2. Add 500 μL 10 mg/mL RNAse (final concentration 1 mg/mL) and 250 μL 10 mg/mL DNAse (final concentration 0.5 mg/mL). Incubate on ice for 30 min., with occasional mixing. The viscosity should decrease.

3. Spin at 21,800g for 20 min. at 4° to retain low-speed-supernatant (LSS).

4. Equilibrate 2 mL of Ni–NTA resin in Full Lysis Buffer.

5. Spin LSS at 180,000g for 30 min. in Beckman ultracentrifuge at 4° to retain high-speed-supernatant (HSS).

6. Mix HSS with Ni resin and incubate at 4° for 1–1.5 hrs. (or overnight) on a rotator.

Day 5

1. Prepare chromatography column by washing with ddH_2O and then Full Lysis Buffer.

2. Prepare 250 mL of Elution Buffer 1 (20 mM imidazole, 4 mM $MgCl_2$, 10 mM β-mercaptoethanol (175 μL)) and Elution Buffer 2 (500 mM imidazole, 4 mM $MgCl_2$, 10 mM β-mercaptoethanol (175 μL).

3. Mix Elution Buffers to obtain Final Elution Buffers:

Final [imidazole] (mM)	Elution Buffer 1 (mL)	Elution Buffer 2 (mL)
70	8.96	1.04
100	8.33	1.67
150	7.29	2.71
200	6.25	3.75
500	0	10

4. Load the mixture onto the column and collect the flow-through (Ni–FT) by gravity in the cold room.

5. Wash the column with Full Lysis Buffer until you get a flat baseline, as measured by the Bradford Reagent[2].

6. Elute and collect fractions with 10 mL volumes of increasing concentration of Final Elution Buffer. Note, for each elution, the first 2 mL of collected fraction actually correspond with the previous imidazole concentration (i.e., after applying 10 mL of 150 mM imidazole, the first 2 mL of collected fraction belong with the 100 mM imidazole fraction).

7. Run the fractions in separate wells of a SDS–PAGE gel and pool the fractions with significant, pure kinesin content.

8. Concentrate the pooled protein samples by spinning in a Vivaspin concentrator.

9. While concentrating, exchange buffer so that the final protein solution is in Kinesin Storage Buffer.

10. Aliquot final protein solution into 5–10 μL volumes, freeze in liquid nitrogen, and store at -80°.

[2]Load a 96-well plate with small volumes of Bradford Reagent. Then apply 5–10 μL of Ni–FT to a well and approximate protein content by Bradford Reagent color change.

C.3 Kinesin Bead Assay

Protocol

1. Make PemTax
   (a) Label a tube **PemTax**, and add:
      i. 1000 μL Pem80 (stored in 4°)
      ii. 2 μL Taxol (10 mM in DMSO, aliquots in -20°)
   (b) Store at RT
2. Make Assay Buffer
   (a) Label a tube **AB**, and add:
      i. 1304 μL Pem80
      ii. 3 μL DTT (0.5 M in 10 mM K-acetate, aliquots in -20°)
      iii. 3 μL Taxol
      iv. 15 μL ATP (100 mM in PEM80, aliquots in -80°)
      v. 25 μL K-acetate (3 M, stored in 4°)
      vi. 150 μL 10 mg/mL Casein in PBT (made fresh once per week and stored at 4°)
   (b) AB final concentrations: 0.1 mM DTT, 20 μM Taxol, 1 mg/mL Casein, 1 mM ATP[3], 50 mM K-acetate
   (c) Store on ice
3. Make C-Tax
   (a) Label a tube **C-Tax**, and add:
      i. 80 μL PemTax
      ii. 20 μL 10 mg/mL Casein

[3]Saturating ATP levels

(b) Store on ice

4. Make bead dilution

   (a) Dilute 20 μL 0.44 μm Streptavidin–coated beads (Spherotech, Cat No. SVP-05-10, 1.0% w/v) into 80 μL PBS

   (b) Wash 4 times at 10,000 rpm for 6 min, reconstituting in 100 μL PBS

   (c) Sonicate for 2 min at 40%

   (d) Label a tube **EM/AB**, and add:

      i. 4 μL beads

      ii. 196 μL AB

5. Make Kinesin dilutions

   (a) **K/100**: 2 μL **K** into 98 μL AB

   (b) **K/1000**: 10 μL **K/100** into 90 μL AB

   (c) ...

6. Make Kinesin/Bead dilution (**KDB**)

   (a) Label a tube **KDB/###**, and add:

      i. 50 μL EM/AB

      ii. 50 μL K/###

   (b) Incubate for 1 hour on the rotator at 4°C

7. Prepare Polylysine–coated coverslips, if not already done

   (a) Dilute 1 mL Poly-L-Lysine into 300 mL EtOH and mix in 1 L beaker

   (b) Place a rack of KOH etched coverslips into the solution, and let sit for 15 min

   (c) Dry for 15 min in the oven

8. Make MT/50 - MT/150 dilutions in PemTax and start warming C-Tax and AB to RT

9. Add Glucose Oxidase plus Catalase to each KDB incubation

   (a) Add 1 μL 100X Glucose oxidase[4] (25 mg/mL in PBT, 10 μL aliquots in -80°)

   (b) Add 1 μL 100X β-D-glucose (500 mg/mL in PBT, 10 μL aliquots in -80°)

   (c) Add 1 μL 100X Catalase[5] (3 mg/mL in PBT, 10 μL aliquots in -80°)

10. Prepare flow channels from Polylysine-coated coverslips

   (a) Flow in 15 μL MT/###, and let bind for 10 min

   (b) Wash in 20 μL PemTax with high velocity

   (c) Wash in 15 μL C-Tax, and let coat for 5 min

   (d) Wash in 50 μL PemTax

   (e) Wash in 80 μL AB

   (f) Wash in 20 μL KDB/###

[4]Calbiochem Cat. #345386
[5]Calbiochem Cat. #219261

C.4 Design of Kinesin Mutant DEL

Materials

1. **WC2 Vector**. Parent kinesin cloning and expression vector, obtained from Gelles Lab (3950 bp).

2. **Gene Synthesis Oligonucleotides**

   (a) WC2_MUT1_1: CCA CAA CGG TTT CCC TCT AGA AAT AAT TTT G

   (b) WC2_MUT1_2: CTC CTT CTT AAA GTT AAA CAA AAT TAT TTC TAG AGG

   (c) WC2_MUT1_3[6]: CTT TAA GAA GGA GAT ATA CAT ATC AAA GTG GTC TGC CG

   (d) WC2_MUT1_4: CTG TCG TTC AGC GGT CGG AAT CGG CAG ACC ACT TTG

   (e) WC2_MUT1_5: CGC TGA ACG ACA GCG AAG AGA AGG CCG GCT CC

   (f) WC2_MUT1_6: ACT TGA CCA CGA ACT TGG AGC CGG CCT TC

3. **Pfu Turbo DNA Polymerase** (2.5 U/μL, Stratagene, Cat No. 600250)

4. **dNTP Mix** (2.5 mM, Invitrogen, Cat No. R72501).

5. **XbaI Restriction Endonuclease** (20,000 U/mL, New England Biolabs, Cat No. R0145S).

6. **NgoMIV Restriction Endonuclease** (10,000 U/mL, New England Biolabs, Cat No. R0564S).

7. **Antarctic Phosphatase** (5,000 U/mL, New England Biolabs, Cat No. M0289S).

8. **T4 DNA Ligase** (400,000 U/mL, New England Biolabs, Cat No. M0202S).

9. **TOP10 Chemically Competent Cells** (Invitrogen, Cat No. C4040-10).

[6]WC2_MUT1_3': CTT TAA GAA GGA GAT ATA CAT ATG ATC AAA GTG GTC TGC CG

10. **BL21(DE3) pLysS Competent Cells** (Stratagene, Cat No. 200132).

11. **QIAquick Gel Extraction Kit** (Qiagen Cat No. 28704).

12. **QIAquick PCR Purification Kit** (Qiagen Cat No. 28104).

13. **QIAprep Spin Miniprep Kit** (Qiagen Cat No. 27104).

14. **Sequencing Primers**

    (a) WC2_seq_FOR: GAC TTC GAA ATT AAT ACG ACT CAC

    (b) WC2_seq_REV: GAA CTG GTG CTT GAA CCT CGG

Gene Synthesis Step 1: Assembly PCR

1. Prepare PCR reaction:

    0.5 μL 10 μM oligonucleotides (WC2_MUT1_1, WC2_MUT1_2, ..., WC2_MUT1_6)

    4 μL 2.5 mM dNTPs

    0.5 μL Pfu Turbo polymerase

    5 μL Pfu buffer

    37.5 μL H_20

    ---

    50 μL total

    PCR: 95°C – 52°C – 72°C (30 cycles)

Gene Synthesis Step 2: Amplification PCR

1. Prepare PCR reaction:

    3 μL Assembly PCR mix

    4 μL 2.5 mM dNTPs

    0.5 μL Pfu Turbo polymerase

5 μL Pfu buffer

5 μL 10 μM flanking oligonucleotide (WC2_MUT1_1)

5 μL 10 μM flanking oligonucleotide (WC2_MUT1_6)

27.5 μL H_20

---

50 μL total

PCR: 95°C – 55°C – 72°C (30 cycles)

2. Run PCR product on 1% (w/v) agarose gel. Extract DNA with QIAquick Gel Extraction Kit, eluting with 32 μL ddH_2O.

Digestion Reactions

1. Prepare 2 digestion reactions:

1.5 μg WC2 vector (32 μL Gene insert ($\sim$ 0.7 μg))

5 μL Buffer 4

0.5 μL 100X BSA

1 μL XbaI

1 μL NgoMIV

xx μL H_2O

---

50 μL total

37°C (3.5 hrs.), 65°C heat kill (20 minutes).

2. Run double-digested products on 1% (w/v) agarose gel. Extract DNA with QIAquick Gel Extraction Kit, eluting with 30 μL ddH_2O.

Vector Dephosphorylation

1. Prepare vector dephosphorylation reaction:

   30 μL WC2 vector

   5 μL Buffer 3

   0.5 μL Antarctic Phosphatase

   14.5 μL H_2O

   ---

   50 μL total

   37°C (30 minutes); 65°C heat kill (20 minutes).

2. Purify vector with QIAquick PCR Purification Kit.

Ligation

1. Prepare ligation reactions:

	Molar Ratio (Insert:Vector)[†]	
	0	5
Vector	50 – 100 ng	50 – 100 ng
Insert	0	$\sim$ 5 – 10 ng
Ligase buffer	5 μL	5 μL
T4 DNA Ligase	0.5 μL	0.5 μL
H_2O	xx	xx
Total	50 μL	50 μL

[†](ng vector) x [(kb insert) / (kb vector)] x (i:v molar ratio) = (ng insert).

16°C overnight; 65°C heat kill (10 minutes).

Cloning Transformation

1. Transform TOP10 Chemically Competent Cells with ligation reactions.
2. Pick and grow colonies overnight in LB Amp (LB Broth with Ampicillin).
3. Purify DNA plasmids using QIAprep Spin Miniprep Kit and sequence with appropriate sequencing primers.

Expression Transformation

1. Transform BL21(DE3) pLysS Competent Cells with mutagenic DNA plasmid.

C.5 Design of Kinesin Mutant 2G

Materials

1. **WC2 Vector**. Parent kinesin cloning and expression vector, obtained from Gelles Lab (3950 bp).

2. **Mutagenic Oligonucleotide** (CGA GAG ATT CCC GGC GAG GAC GGC ATC AAA GTG G).

3. **QuickChange Multi Site-Directed Mutagenesis Kit** (Stratagene, Cat No. 200514).

4. **BL21(DE3) pLysS Competent Cells** (Stratagene. Cat No. 200132).

5. **QIAprep Spin Miniprep Kit** (Qiagen Cat No. 27104).

Mutagenesis

1. Follow protocol provided by QuickChange Multi Site-Directed Mutagenesis Kit for templates $\leq$ 5 kb.

2. After transforming the provided competent cells, purify DNA plasmids using QIAprep Spin Miniprep Kit and sequence with appropriate sequencing primers.

Expression Transformation

1. Transform BL21(DE3) pLysS Competent Cells with mutagenic DNA plasmid.

Bibliography

[1] E. A. Abbondanzieri, W. J. Greenleaf, J. W. Shaevitz, R. Landick, and S. M. Block. Direct observation of base-pair stepping by RNA polymerase. *Nature*, 438(7067):460–465, 2005.

[2] M. Adams, Z. Dogic, S. L. Keller, and S. Fraden. Entropically driven microphase transitions in mixtures of colloidal rods and spheres. *Nature*, 393(6683):349–352, 1998.

[3] D. Altman, H. L. Sweeney, and J. A. Spudich. The mechanism of myosin VI translocation and its load-induced anchoring. *Cell*, 116(5):737–749, 2004.

[4] C. L. Asbury, A. N. Fehr, and S. M. Block. Kinesin moves by an asymmetric hand-over-hand mechanism. *Science*, 302(5653):2130–2134, 2003.

[5] A. Ashkin. Acceleration and trapping of particles by radiation pressure. *Phys. Rev. Lett.*, 24(4):156–159, 1970.

[6] A. Ashkin and J. M. Dziedzic. Optical trapping and manipulation of viruses and bacteria. *Science*, 235(4795):1517–1520, 1987.

[7] F. M. Aslan, Yu Y., S. C. Mohr, and C. R. Cantor. Engineered single-chain dimeric streptavidins with an unexpected strong preference for biotin-4-fluorescein. *Proc. Natl. Acad. Sci. U.S.A.*, 102(24):8507–8512, 2005.

[8] K. Beck and R. M. Duenki. Stiff chains and filaments under tension. *J. Struct. Biol.*, 105:22–27, 1990.

[9] E. Berliner, H. K. Mahtani, S. Karki, L. F. Chu, J. E. Cronan Jr., and J. Gelles. Microtubule movement by a biotinylated kinesin bound to streptavidin-coated surface. *J. Biol. Chem.*, 269(11):8610–8615, 1994.

[10] E. Berliner, E. C. Young, K. Anderson, H. K. Mahtani, and J. Gelles. Failure of a single-headed kinesin to track parallel to microtubule protofilaments. *Nature*, 373(6516):718–721, 1995.

[11] S. M. Block. Real engines of creation. *Nature*, 386(6622):217–219, 1997.

[12] S. M. Block. Kinesin motor mechanics: binding, stepping, tracking, gating, and limping. *Biophys. J.*, 92(9):2986–2995, 2007.

[13] S. M. Block, C. L. Asbury, J. W. Shaevitz, and M. J. Lang. Probing the kinesin reaction cycle with a 2D optical force clamp. *Proc. Natl. Acad. Sci. U.S.A*, 100(5):2351–2356, 2003.

[14] D. H. Boal. *Mechanics of the cell.* Cambridge University Press, 2002.

[15] L. J. Bonderer, A. R. Studart, and L. J. Gaukler. Bioinspired design and assembly of platelet reinforced polymer films. *Science*, 319(5866):1069–1073, 2008.

[16] R. R. Brau. *Exploring the mechanome with optical tweezers and single molecule fluorescence.* PhD thesis, Massachusetts Institute of Technology, 2007.

[17] R. R. Brau, P. B. Tarsa, J. M. Ferrer, P. Lee, and M. J. Lang. Interlaced optical force-fluorescence measurements for single molecule biophysics. *Biophys. J.*, 91(3):1069–1077, 2006.

[18] M. L. Bulyk, X. Huang, Y. Choo, and G. M. Church. Exploring the DNA-binding specificities of zinc fingers with DNA microarrays. *Proc. Natl. Acad. Sci. U.S.A.*, 98(13):7158–7163, 2001.

[19] R. B. Case, S. Rice, C. L. Hart, B. Ly, and R. D. Vale. Role of the kinesin neck linker and catalytic core in microtubule-based motility. *Curr. Biol.*, 10(3):157–160, 2000.

[20] C. Cecconi, E. A. Shank, C. Bustamante, and S. Marqusee. Direct observation of the three-state folding of a single protein molecule. *Science*, 309(5743):2057–2060, 2005.

[21] Y. Choo and Klug A. Toward a code for the interactions of zinc fingers with DNA: selection of randomized fingers displayed on phage. *Proc. Natl. Acad. Sci. U.S.A.*, 91(23):11163–11167, 1994.

[22] Y. Choo and A. Klug. Selection of DNA binding sites for zinc fingers using rationally randomized DNA reveals coded interactions. *Proc. Natl. Acad. Sci. U.S.A.*, 91(23):11168–11172, 1994.

[23] B. A. Christy, L. F. Lau, and D. Nathans. A gene activated in mouse 3T3 cells by serum growth factors encodes a protein with "zinc finger" sequences. *Proc. Natl. Acad. Sci. U.S.A.*, 85(21):7857–7861, 1988.

[24] J. D. Currey. Mechanical properties of mother of pearl in tension. *Proc. R. Soc. London Ser. B*, 196(1125):443–463, 1977.

[25] G. Dai, M. R. Kaazempur-Mofrad, S. Natarajan, Y. Zhang, S. Vaughn, B. R. Blackman, R. D. Kamm, G. García-Cardeña, and M. A. Gimbrone. Distinct endothelial phenotypes evoked by arterial waveforms derived from atherosclerosis-susceptible and -resistant regions of human vasculature. *Proc. Natl. Acad. Sci. U.S.A.*, 101(41):14871–14876, 2004.

[26] P. A. M. Dirac. Quantised singularities in the electromagnetic field. *Proc. R. Soc. London Ser. A*, 133(821):60–72, 1931.

[27] M. Doi and S. F. Edwards. *The theory of polymer dynamics.* Clarendon Press, 1986.

[28] D. E. Dupuis, W. H. Guilford, Wu J., and D. M. Warshaw. Actin filament mechanics in the laser trap. *J. Muscle Res. Cell Motil.*, 18(1):17–30, 1997.

[29] J. Elf, G.-W. Li, and X. S. Xie. Probing transcription factor dynamics at the single-molecule level in a living cell. *Science*, 316(5828):1191–1194, 2007.

[30] M. Elrod-Erickson and C. O. Pabo. Binding studies with mutants of Zif268. contribution of individual side chains to binding affinity and specificity in the Zif268 zinc finger-DNA complex. *J. Biol. Chem.*, 274(27):19281–19285, 1999.

[31] S. A. Endow and K. W. Waligora. Determinants of kinesin motor polarity. *Science*, 281(5380):1200–1202, 1998.

[32] E. Evans and K. Ritchie. Dynamic strength of molecular adhesion bonds. *Biophys. J.*, 72(4):1541–1555, 1997.

[33] J. M. Ferrer. *Mapping the actin and actin binding proteins interactions: from micromechanics to single molecule force spectroscopy.* PhD thesis, Massachusetts Institute of Technology, 2007.

[34] M. E. Fisher and A. B. Kolomeisky. The force exerted by a molecular motor. *Proc. Natl. Acad. Sci. U.S.A.*, 96(12):6597–6602, 1999.

[35] M. E. Fisher and A. B. Kolomeisky. Simple mechanochemistry describes the dynamics of kinesin molecules. *Proc. Natl. Acad. Sci. U.S.A.*, 98(14):7748–7753, 2001.

[36] M. A. Geeves and K. C. Holmes. The molecular mechanism of muscle contraction. *Adv. Protein Chem.*, 71:161–193, 2005.

[37] F. Gittes and C. F. Schmidt. Interference model for back-focal-plane displacement detection in optical tweezers. *Opt. Lett.*, 23(1):7–9, 1998.

[38] W. Gobush, H. Yamakawa, W. H. Stockmayer, and W. S. Magee. Statistical mechanics of wormlike chains. I. Asymptotic behavior. *J. Chem. Phys.*, 57(7):2839, 1972.

[39] J. Hasty, D. McMillen, and J. J. Collins. Engineered gene circuits. *Nature*, 420(6912):224–230, 2002.

[40] J. J. Hermans and R. Ullman. The statistics of stiff chains, with applications to light scattering. *Physica*, 18(11):951–971, 1952.

[41] Y. Hori, A. Prasad, and J. Kondev. Stretching short biopolymers by fields and forces. *Phys. Rev. E*, 75:041904, 2007.

[42] Y. Huang, C.-Y. Chiang, S. K. Lee, Y. Gao, E. L. Hu, J. E. Yoreo, and A. M. Belcher. Programmable assembly of nanoarchitectures using genetically engineered viruses. *Nano Lett.*, 5(7):1429–1434, 2005.

[43] G. Hummer and A. Szabo. Free energy surfaces from single-molecule force spectroscopy. *Acc. Chem. Res.*, 38(7):504–513, 2005.

[44] W. Hwang. Calculation of conformation-dependent biomolecular forces. *J. Chem. Phys.*, 127(17):175104, 2007.

[45] W. Hwang, M. J. Lang, and M. Karplus. Force generation in kinesin hinges on cover-neck bundle formation. *Structure*, 16(1):62–71, 2008.

[46] A. C. Jamieson, J. C. Miller, and C. O. Pabo. Drug discovery with engineering zinc-finger proteins. *Nat. Rev. Drug Discov.*, 2(5):361–368, 2003.

[47] D. Keller, D. Swigon, and C. Bustamante. Relating single-molecule measurements to thermodynamics. *Biophys. J.*, 84(2):733–738, 2003.

[48] A. S. Khalil, D. C. Appleyard, A. K. Labno, A. Georges, M. Karplus, A. M. Belcher, W. Hwang, and M. J. Lang. Kinesin's cover-neck bundle folds forward to generate force. *Proc. Natl. Acad. Sci. U.S.A*, Accepted for publication, 2008.

[49] A. S. Khalil, J. M. Ferrer, R. R. Brau, S. T. Kottmann, C. J. Noren, M. J. Lang, and A. M. Belcher. Single M13 bacteriophage tethering and stretching. *Proc. Natl. Acad. Sci. U.S.A*, 104(12):4892–4897, 2007.

[50] A. S. Khalil, G. T. Hess, J. Y. Mao, Y. Shin, D. Ghosh, M. J. Lang, and A. M. Belcher. Engineered bacteriophages as standalone single-molecule handles: phage arms to zinc fingers. *Nat. Methods*, Manuscript in preparation, 2008.

[51] M. Kikkawa. The role of microtubules in processive kinesin movement. *Trends Cell Biol.*, 18(3):128–135, 2008.

[52] M. Kikkawa, E. P. Sablin, Y. Okada, H. Yajima, R. J. Fletterick, and N. Hirokawa. Switch-based mechanism of kinesin motors. *Nature*, 411(6836):439–445, 2001.

[53] H. Kojima, E. Muto, H. Higuchi, and T. Yanagida. Mechanics of single kinesin molecules measured by optical trapping nanometry. *Biophys. J.*, 73(4):2012–2022, 1997.

[54] O. Kratky and G. Porod. Röntgenuntersuchung gelöster Fadenmoleküle. *Rec. Trav. Chim. Pays-Bas*, 68:1106–1123, 1949.

[55] M. M. G. Krishna and S. W. Englander. The N-terminal to C-terminal motif in protein folding and function. *Proc. Natl. Acad. Sci. U.S.A.*, 102(4):1053–1058, 2005.

[56] F. J. Kull, E. B. Sablin, R. Lau, R. J. Fletterick, and R. D. Vale. Crystal structure of the kinesin motor domain reveals a structural similarity to myosin. *Nature*, 380(6574):550–555, 1996.

[57] L. D. Landau and E. M. Lifshitz. *Theory of elasticity.* Pergamon Press, 1986.

[58] M. J. Lang, C. L. Asbury, J. W. Shaevitz, and S. M. Block. An automated two-dimensional optical force clamp for single molecule studies. *Biophys. J.*, 83(1):491–510, 2002.

[59] M. J. Lang, P. M. Fordyce, A. M. Engh, K. C. Neuman, and S. M. Block. Simultaneous, coincident optical trapping and single-molecule fluorescence. *Nat. Methods*, 1(2):133–139, 2004.

[60] A. W. C. Lau, K.-H. Lin, and A. G. Yodh. Entropic interactions in suspensions of semiflexible rods: short-range effects of flexibility. *Phys. Rev. E*, 66(2):020401, 2002.

[61] S.-W. Lee, C. Mao, C. E. Flynn, and A. M. Belcher. Ordering of quantum dots using genetically engineered viruses. *Science*, 296(5569):892–895, 2002.

[62] K.-H. Lin, J. C. Crocker, A. C. Zeri, and A. G. Yodh. Colloidal interactions in suspensions of rods. *Phys. Rev. Lett.*, 87(8):088301, 2001.

[63] J. Liphardt, B. Onoa, S. B. Smith, I. Tinoco Jr., and C. Bustamante. Reversible unfolding of single RNA molecules by mechanical force. *Science*, 292(5517):733–737, 2001.

[64] S. J. Maerkl and S. R. Quake. A systems approach to measuring the binding energy landscapes of transcription factors. *Science*, 315(5809):233–237, 2007.

[65] R. Mallik, B. C. Carter, S. A. Lex, S. J. King, and S. P. Gross. Cytoplasmic dynein functions as a gear in response to load. *Nature*, 427(6975):649–652, 2004.

[66] C. Mao, C. E. Flynn, A. Hayhurst, R. Sweeney, J. Qi, G. Georgiou, B. Iverson, and A. M. Belcher. Viral assembly of oriented quantum dot nanowires. *Proc. Natl. Acad. Sci. U.S.A.*, 100(12):6946–6951, 2003.

[67] C. Mao, D. J. Solis, B. D. Reiss, S. T. Kottman, R. Y. Sweeney, A. Hayhurst, G. Georgiou, B. Iverson, and A. M. Belcher. Virus-based toolkit for the directed synthesis of magnetic and semiconducting nanowires. *Science*, 303(5655):213–217, 2004.

[68] J. F. Marko. Stretching must twist DNA. *Europhys. Lett.*, 38(3):183–188, 1997.

[69] J. F. Marko and E. D. Siggia. Stretching DNA. *Macromolecules*, 28(26):8759–8770, 1995.

[70] G. Mayer. Rigid biological systems as models for synthetic composites. *Science*, 310(5751):1144–1147, 2005.

[71] A. D. Mehta, M. Rief, J. A. Spudich, D. A. Smith, and R. M. Simmons. Single-molecule biomechanics with optical methods. *Science*, 283(5408):1689–1695, 1999.

[72] J. C. Miller and C. O. Pabo. Rearrangement of side-chains in a Zif268 mutant highlights the complexities of zinc finger-DNA recognition. *J. Mol. Biol.*, 313(2):309–315, 2001.

[73] J. P. Mills, L. Qie, M. Dao, C. T. Lim, and S. Suresh. Nonlinear elastic and viscoelastic deformation of the human red blood cell with optical tweezers. *Mech. Chem. Biosys.*, 1(3):169–180, 2004.

[74] S. Mohanty, J. H. Meinke, O. Zimmermann, and U. H. E. Hansmann. Simulation of Top7-CFr: a transient helix extension guides folding. *Proc. Natl. Acad. Sci. U.S.A.*, 105(23):8004–8007, 2008.

[75] T. Mori, R. D. Vale, and M. Tomishige. How kinesin waits between steps. *Nature*, 450(7170):750–754, 2007.

[76] K. T. Nam, D.-W. Kim, P. J. Yoo, C.-Y. Chiang, N. Meethon, P. T. Hammond, Y.-M. Chiang, and A. M. Belcher. Virus-enabled synthesis and assembly of nanowires for lithium ion battery electrodes. *Science*, 312(5775):885–888, 2006.

[77] K. T. Nam, B. R. Peelle, S.-W. Lee, and A. M. Belcher. Genetically driven assembly of nanorings based on the M13 virus. *Nano Lett.*, 4(1):23–27, 2004.

[78] K. C. Neuman and S. M. Block. Optical trapping. *Rev. Sci. Instrum.*, 75(9):2787–2809, 2004.

[79] K. C. Neuman and A. Nagy. Single-molecule force spectroscopy: optical tweezers, magnetic tweezers and atomic force microscopy. *Nat. Methods*, 5(6):491–505, 2008.

[80] J. Newman, H. L. Swinney, and L. A. Day. Hydrodynamic properties and structure of fd virus. *J. Mol. Biol.*, 116(3):593–603, 1977.

[81] T. Odijk. Stiff chains and filaments under tension. *Macromolecules*, 28(20):7016–7018, 1995.

[82] B. Onoa, S. Dumont, J. Liphardt, S. B. Smith, I. Tinoco Jr., and C. Bustamante. Identifying kinetic barriers to mechanical unfolding of T. thermophila ribozyme. *Science*, 299(5614):1892–1895, 2003.

[83] L. Onsager. The effects of shape on the interaction of colloidal particles. *Ann. NY Acad. Sci.*, 51(4):627–659, 1949.

[84] A. J. Opella, P. L. Stewart, and K. G Valentine. Protein structure by solid-state NMR spectroscopy. *Q. Rev. Biophys.*, 19(1–2):7–49, 1987.

[85] C. O. Pabo and L. Nekludova. Geometric analysis and comparison of protein-DNA interfaces: why is there no simple code for recognition? *J. Mol. Biol.*, 301(3):597–624, 2000.

[86] N. P. Pavletich and C. O. Pabo. Zinc finger-DNA recognition: crystal structure of a Zif268-DNA complex. *Science*, 252(5007):809–817, 1991.

[87] E. Peisach and C. O. Pabo. Constraints for zinc finger linker design as inferred from X-ray crystal structure of tandem Zif268-DNA complexes. *J. Mol. Biol.*, 330(1):1–7, 2003.

[88] M. E. Peskin and D. V. Schroeder. *An introduction to quantum field theory.* Harper-Collins, 1995.

[89] R. Phillips and S. R. Quake. The biological frontier of physics. *Phys. Today*, 5(3):38–43, 2006.

[90] E. J. Rebar, Y. Huang, R. Hickey, A. K. Nath, D. Meoli, S. Nath, B. Chen, L. Xu, Y. Liang, A. C. Jamieson, L. Zhang, S. K. Spratt, C. C. Case, A. Wolffe, and F. J. Giordano. Induction of angiogenesis in a mouse model using engineered transcription factors. *Nat. Med.*, 8(12):1427–1432, 2002.

[91] E. J. Rebar and C. O. Pabo. Zinc finger phage: affinity selection of fingers with new DNA-binding specificities. *Science*, 263(5147):671–673, 1994.

[92] S. Rice, Y. Cui, C. Sindelar, N. Naber, M. Matuska, R. D. Vale, and R. Cooke. Thermodynamic properties of the kinesin neck-region docking to the catalytic core. *Biophys. J.*, 84(3):1844–1854, 2003.

[93] S. Rice, A. W. Lin, D. Safer, N. Hart, C. L. Naber, B. O. Carragher, S. M. Cain, E. Pechatnikova, E. M. Wilson-Kubalek, M. Whittaker, E. Pate, R. Cooke, E. W. Taylor, R. A. Milligan, and R. D. Vale. A structural change in the kinesin motor protein that drives motility. *Nature*, 402(6763):778–784, 1999.

[94] G. Roosen and C. Imbert. Optical levitation by means of two horizontal laser beams – a theoretical and experimental study. *Phys. Lett.*, 59A:6–8, 1976.

[95] S. S. Rosenfeld, P. M. Fordyce, G. M. Jefferson, P. H. King, and S. M. Block. Stepping and stretching: how kinesin uses internal strain to walk processively. *J. Biol. Chem.*, 278(20):18550–18556, 2003.

[96] J. Sambrook and D. W. Russell. *Molecular cloning: a laboratory manual.* Cold Spring Harbor Laboratory Press, 3rd edition, 2001.

[97] K. E. Sandman, J. S. Benner, and C. J. Noren. Phage display of selenopeptides. *J. Am. Chem. Soc.*, 122(5):960–961, 2000.

[98] T. G. M. Schmidt, J. Koepke, R. Frank, and A. Skerra. Molecular interaction between the Strep-tag affinity peptide and its cognate target, streptavidin. *J. Mol. Biol.*, 255(5):753–766, 1996.

[99] M. J. Schnitzer and S. M. Block. Kinesin hydrolyses one ATP per 8-nm step. *Nature*, 388(6640):368–390, 1997.

[100] N. C. Seeman and A. M. Belcher. Emulating biology: building nanostructures from the bottom up. *Proc. Natl. Acad. Sci. U.S.A.*, 99(Suppl 2):6451–6455, 2002.

[101] C. V. Sindelar, M. J. Budny, S. Rice, N. Naber, R. Fletterick, and R. Cooke. Two conformations in the human kinesin power stroke defined by x-ray crystallography and EPR spectroscopy. *Nat. Struct. Biol.*, 9(11):844–848, 2002.

[102] C. V. Sindelar and K. H. Downing. The beginning of kinesin's force-generating cycle visualized at 9-Å resolution. *J. Cell Biol.*, 177(3):377–385, 2007.

[103] S. B. Smith, Y. Cui, and C. Bustamante. Overstretching B-DNA: the elastic response of individual double-stranded and single-stranded DNA molecules. *Science*, 271(5250):795–799, 1996.

[104] S. B. Smith, L. Finzi, and C. Bustamante. Direct mechanical measurements of the elasticity of single DNA molecules by using magnetic beads. *Science*, 258(5085):1122–1126, 1992.

[105] L. S. Song, U.-S. Kim, J. Wilcoxon, and J. M. Schurr. Dynamic light scattering from weakly bending rods: estimation of the dynamic bending rigidity of the M13 virus. *Biopolymers*, 31(5):547–567, 1991.

[106] K. Svoboda and S. M. Block. Biological applications of optical forces. *Annu. Rev. Biophys. Biomol. Struct.*, 23:247–285, 1994.

[107] K. Svoboda, C. F. Schmidt, B. J. Schnapp, and S. M. Block. Direct observation of kinesin stepping by optical trapping interferometry. *Nature*, 365(6448):721–727, 1993.

[108] J. X. Tang, P. A. Janmey, A. Lyubartsev, and L. Nordenskiöld. Metal ion-induced lateral aggregation of filamentous viruses fd and M13. *Biophys. J.*, 83(1):566–581, 2002.

[109] M. Tomishige, N. Stuurman, and R. D. Vale. Single-molecule observations of neck linker conformational changes in the kinesin motor protein. *Nat. Struct. Mol. Biol.*, 13(10):887–894, 2006.

[110] R. D. Vale. The molecular motor toolbox for intracellular transport. *Cell*, 112(4):467–480, 2003.

[111] R. D. Vale and R. G. Milligan. The way things move: looking under the hood of molecular motor proteins. *Science*, 288(5463):88–95, 2000.

[112] J. van Mameren. Single molecule mechanics of biopolymers: an optical tweezers study. Master's thesis, Vrije Universiteit, 2002.

[113] K. Visscher, M. J. Schnitzer, and S. M. Block. Single kinesin molecules studied with a molecular force clamp. *Nature*, 400(6740):184–189, 1999.

[114] L. E. Waner, P. Mancias, I. J. Butler, C. M. McDonald, L. Keppen, G. Koob, and J. R. Lupski. Mutations in the early growth response 2 EGR2 gene are associated with hereditary myelinopathies. *Nat. Genet.*, 18(4):382–384, 1998.

[115] M. D. Wang, M. J. Schnitzer, H. Yin, R. Landick, J. Gelles, and S. M. Block. Force and velocity measured for single molecules of RNA polymerase. *Science*, 282(5390):902–907, 1998.

[116] M. D. Wang, H. Yin, R. Landick, J. Gelles, and S. M. Block. Stretching DNA with optical tweezers. *Biophys. J.*, 72(3):1335–1346, 1997.

[117] R. Webster. Filamentous phage biology. In C. F. Barbas III, D. R. Burton, J. K. Scott, and G. J. Silverman, editors, *Phage display: a laboratory manual*, pages 1.1–1.37. Cold Spring Harbor Laboratory Press, 2001.

[118] S. R. Whaley, D. S. English, E. L. Hu, P. F. Barbara, and A. M. Belcher. Selection of peptides with semiconductor binding specificity for directed nanocrystal assembly. *Nature*, 405(6787):665–668, 2000.

[119] J. Wilhelm and E. Frey. Radial distribution function of semiflexible polymers. *Phys. Rev. Lett.*, 77(12):2581–2584, 1996.

[120] E. Winfree, F. Liu, L. A. Wenzler, and N. C. Seeman. Design and self-assembly of two-dimensional DNA crystals. *Nature*, 394(6693):539–544, 1998.

[121] M. T. Woodside, P. C. Anthony, W. M. Behnke-Parks, K. Larizadeh, D. Herschlag, and S. M. Block. Direct measurement of the full, sequence-dependent folding landscape of a nucleic acid. *Science*, 315(5801):1001–1004, 2006.

[122] M. T. Woodside, W. M. Behnke-Parks, K. Larizadeh, K. Travers, D. Herschlag, and S. M. Block. Nanomechanical measurements of the sequence-dependent folding landscapes of single nucleic acid hairpins. *Proc. Natl. Acad. Sci. U.S.A.*, 103(16):6190–6195, 2006.

[123] H. Wu, W. P. Yang, and C. F. Barbas. Building zinc fingers by selection: toward a therapeutic application. *Proc. Natl. Acad. Sci. U.S.A.*, 92(2):344–348, 1995.

[124] H. Yamakawa. *Modern theory of polymer solutions.* Harper & Row, 1971.

[125] H. Yamakawa and M. Fujii. Intrinsic viscosity of wormlike chains. Determination of the shift factor. *Macromolecules*, 7(1):128–135, 1974.

[126] P. J. Yoo, K. T. Nam, J. Qi, S.-K. Lee, J. Park, A. M. Belcher, and P. T. Hammond. Spontaneous assembly of viruses on multilayered polymer surfaces. *Nat. Mater.*, 5(3):234–240, 2006.

[127] S. Zhang. Fabrication of novel biomaterials through molecular self-assembly. *Nat. Biotechnol.*, 21(10):1171–1178, 2003.